MICRO-LENS-COUPLED LED NEURAL STIMULATORS FOR OPTOGENETICS

By

Xiaopeng Bi

A DISSERTATION

Submitted to
Michigan State University
in partial fulfillment of the requirements
for the degree of

Electrical Engineering—Doctor of Philosophy

2016

ABSTRACT

MICRO-LENS-COUPLED LED NEURAL STIMULATORS FOR OPTOGENETICS

By

Xiaopeng Bi

Optogenetics is a fast growing neuromodulation technique, which can remotely manipulate the specific activities of genetically-targeted neural cells and associated biological behaviors with millisecond temporal precision through light illumination. Application of optogenetics in neuroscience studies has created an increased need for the development of light sources and the instruments for light delivery. Micro-Light-emitting diodes (μ-LEDs) offer a great option as the light source for optogenetics since they are power-efficient, low-cost and suitable for integration with wireless electronics. Furthermore, arrays of individually addressable μ-LEDs have been developed to accomplish multisite in-vivo stimulation. However, a critical challenge of using μ-LEDs as the light source for optogenetics is their intrinsically low out-coupling efficiency and wide irradiation angles due to the Lambertian emission pattern, which results in a big loss of the radiation. Consequently, μ-LEDs must be driven with high power in order to reach the required light intensity of 1 mW/mm^2 and 7 mW/mm^2 for effective activation of excitatory and inhibitory opsins at the target site, respectively. However, this is not suitable for wireless operation, and could induce potential thermal interference or damage to tissues due to Joule heating effect. In this thesis, an implantable, micro-lens-coupled LED stimulator has been proposed to be applied as the light source for neural stimulation. A reflector and a microlens were coupled with the μ-LED chip for light collection and collimation, giving rise to a significantly improved light irradiance. A novel microfabrication method, vapor-induced dewetting, was developed to make self-organized SU-8 microlens arrays. It was later involved in the fabrication and integration process of micro-lens-coupled LED stimulators. An optimization on the device structure was

carried out using optical simulation in order to attain optimal penetration capabilities of the light. The optimized micro-lens-coupled LED stimulator was microfabricated and measured both in air and in tissue experimentally. Significant improvement of >60% in light intensity was achieved, validating its functionality and potential as the light source for optogenetic neuromodulation in deep cortical layers.

ACKNOWLEDGMENTS

First, I would like to express my gratitude to my advisor Prof. Wen Li. She is one of the smartest people I know. Her enthusiasm for the research and science is contagious in the group. I appreciate her expert guidance and scientific advice throughout my Ph.D study, as well as all her contributions of time and inspiring ideas. Talking with her, either on research or on my personal development, is always very helpful. Special thanks to her kindness, patience and understanding.

I am also highly indebted to my thesis committee, including Prof. Lixin Dong, Prof. Tim Hogan and Prof. Ilsoon Lee for their constructive advices and suggestions regarding my research progress in the past a few years.

I would also like to thank my colleagues Brian Crum, Bin Fan, Tian Xie, Yue Guo, Nathan Wood, Ki Yong Kwon, Haider Al-Mumen, Wasif Khan, Lin Li and Yue Huang for their technical assistance in various microfabrication processes, simulations and analysis.

Finally, and most importantly, I would like to sincerely thank my wife Rui Xu and my parents for their consistent support, encouragement and unending love. This work is dedicated to them.

TABLE OF CONTENTS

LIST OF TABLES

LIST OF FIGURES

CHAPTER 1 Introduction

1.1 Motivation

1.1.1 Optogenetics

Optogenetics is a fast growing neuromodulation technology which allows manipulation on activities of genetically targeted neurons with high temporal and spatial resolution through light illumination [1-5]. It combines techniques of genetics and optics to precisely control and monitor well-defined biological events in living tissues, even in the freely moving animals [6]. Basically, optogenetics includes three crucial approaches: (i) light delivery into tissues, (ii) targeting the control tools, that are able to respond to light and deliver effector function, to cells of interest, and (iii) recording and analysis of neural signals. Optogenetics has opened new landscapes for the study in neuroscience and biology.

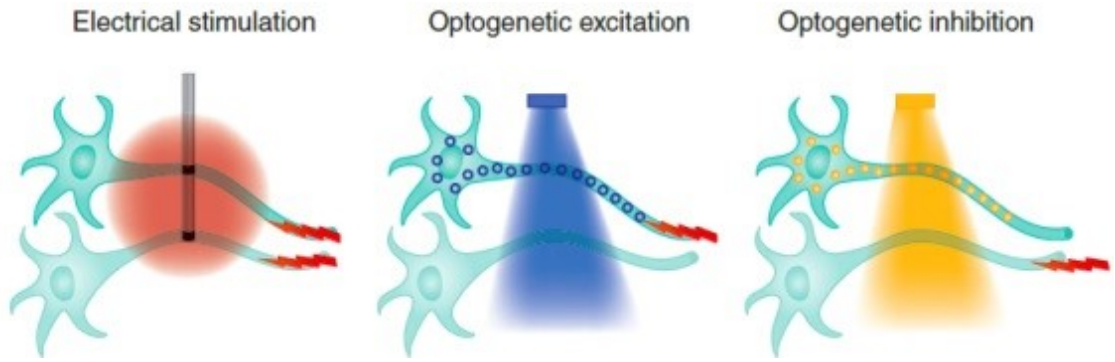

Figure 1 Principle of electrical stimulation and optogenetics [5].

Compared to electrical stimulation, which needs to implant electrodes directly into brains, optogenetics provides a minimally invasive way to deliver signal to neurons [5, 7]. As shown in Figure 1, a key advantage of optogenetics over electrical stimulation is cellular specificity, which

can be achieved through genetic targeting, because genetic expression is limited in a specific type of neuron cells. On the contrary, electrical stimulation suffers from indiscriminate activation of cell components (somas, dendrites, and axons) and thus a random set of neurons are activated. Optogenetic neuromodulation uniquely combines cell type-specific control with millisecond time scale temporal resolution in a fully reversible manner. The cell type-specificity in rodents can be achieved by selecting appropriate promoters, for example, CaMKIIα for targeting excitatory neurons, glial fibrillary acidic protein (GFAP) for targeting astrocytes, and ppHcrt promoter for targeting hypocretin neurons. Another important benefit of optogenetics over electrical stimulation is that it produces minimal electrical artifacts and instrumental interferences with electrophysiological recording, thereby allowing simultaneous recording of light-evoked neural activity.

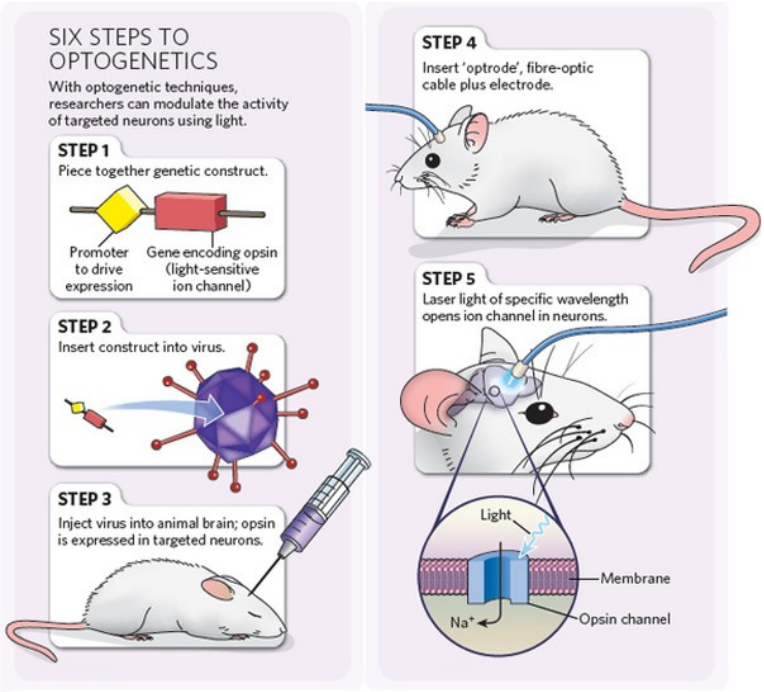

Figure 2 The realization of genetically targeted expression of light sensitive proteins [8].

The realization of genetically targeted expression of light sensitive proteins is illustrated in Figure 2. First, a genetic construct is designed by placing the gene encoding a light sensitive opsin together with a promoter that can drive its expression. Second, the construct is packaged into a virus, which is then injected into the target region in the animal brain where opsin can be genetically expressed in targeted neural cells under the control of the promoter. Third, a light source, typically an LED and a laser coupled with an optic fiber, is employed to deliver the light of specific wavelength to a precise area. As a consequence, the targeted neurons are fired through light illumination since the expressed light sensitive opsin acts as a rectifying ion channel which is directly gated by the light with specific wavelength [9]. Finally, the effects of manipulating cellular activity are measured and assessed. Ideally, the activation of the animal behavior (it can be excitation or inhibition) controlled by those targeted neurons can be achieved, and modulated by switching the light on and off. Based on the genetic expression in specified cell types, although the light is incident across a large field, only targeted neurons can be excited.

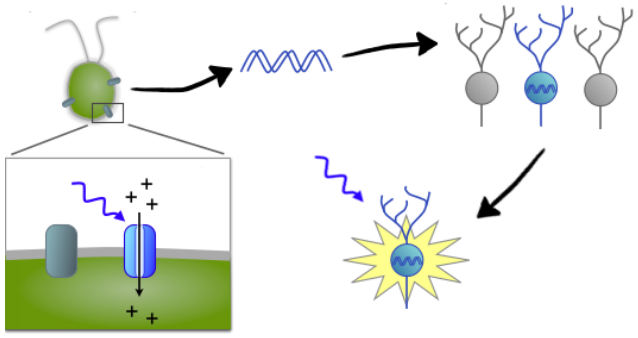

Figure 3 Neurons with genetically targeted expression of light sensitive ChR2 can be excited through illumination of blue light.

The current studies on optogenetics popularly use channelrhodopsin-2 (ChR2), a cation channel highly sensitive to visible light [1-3, 6-9]. In ChR2-expressing neurons, action potentials

can be evoked with an excitation power of approximately 1 mW/mm^2 at the maximal absorption wavelength of 470 nm. Thus, as shown in Figure 3, illumination with blue light can provide effective excitation, resulting in a permeation of sodium and potassium ions. The high sensitivity of ChR2 has been critical for its successful utilization, especially for *in vivo* studies.

Besides the prospect of basic investigation on structure and function of neuron networks, optogenetics also offers new hopes for patients suffering from vision impairment or neurological disorders based on its potential capability of modulating the activity of brain circuits.

1.1.2 Light Sources for Optogenetics

Applications of optogenetics in neuroscience studies has inspired the development of light sources and instruments for light delivery. Well-defined spectral, temporal and spatial control is very important as well as homogenous and constant output. Photo-excitation of the neural cells is most commonly accomplished by illuminating the target with a fluorescence lamp or a laser beam with an optic fiber tether [6, 10, 11]. Although these methods can provide strong illumination and decent positioning of the spot, their spatial resolution is limited, and the tethered optical fibers greatly restrict the natural behavior of freely moving subjects.

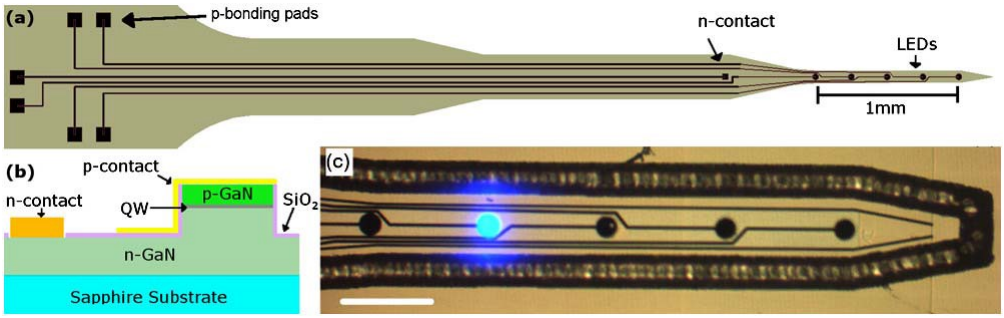

Figure 4 Micro-fabricated optogenetic tools which employ LEDs as the light source [12].

The employment of micro-light-emitting diodes (μ-LEDs) offers a great option as the light source for optogenetics. One of the examples that have been reported is shown in Figure 4 [12]. μ-LEDs are power-efficient, low-cost and suitable for integration with wireless electronics. They can also be incorporated into implants, allowing untethered light delivery in freely moving animals [13]. Furthermore, arrays of individually addressable μ-LEDs have been developed to accomplish multisite *in-vivo* stimulation [14-17]. Such spatiotemporal control over large numbers of neurons benefits both basic study of neuron network dynamics and clinical applications such as retinal prosthesis.

1.2 Challenge

A major drawback of using LEDs as the light source for optogenetics is their intrinsically low out-coupling efficiency and wide irradiation angles due to Lambertian emission pattern, which features a large beam angle around 90° to 120°, rather than in a coherent beam. Therefore, the amount of light from an LED that eventually reaches the targeted neurons has been significantly weakened. Consequently, LEDs must be driven with high power in order to reach the required light intensity of 1 mW/mm^2 and 7 mW/mm^2 for effective activation of excitatory and inhibitory opsins at the target site, respectively. However, this is not suitable for wireless operation, and could induce potential thermal interference or damage to tissues due to Joule heating effect. In addition, as shown in Figure 5, since the neural tissue is structurally comprised of several layers of neurons that correspond to different biological functions, neural stimulation on targeted deep layers but without the increase of power consumption is particularly desired to enable investigation on specified functions [18].

Based on the challenges discussed above, an extra μ-LED-coupled optical component which

can help collimate the LED light is particularly desired, offering capabilities of optical neurostimulation with reduced input voltage and power consumption. Our research group has developed a 3-D multi-waveguide probe array which is able to effectively deliver the light independently from each μ-LED to simultaneously target multiple spots in the brain, as shown in Figure 6 [17, 19]. However, such a waveguide is invasive and could lead to damage to living tissues due to the unavoidable contact.

In the macroscopic scale, an optimized secondary optical device is of great importance while designing LED lighting fitting and have already been widely commercialized, as shown in Figure 7, with a great majority of them made by molding. However, when the size scales down to tens or hundreds of micrometer, the quality of molding greatly lowers due to the problem of resolution. To date, little study has been reported on the fabrication of micro-scale LED-coupled optical devices for optogenetic applications [20, 21].

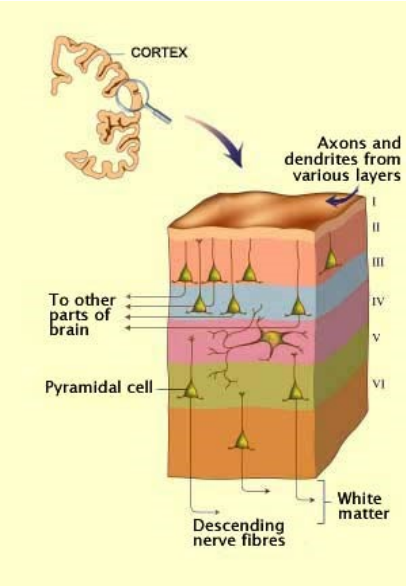

Figure 5 Neural cells with various functions are distributed in different layers of a cortex.

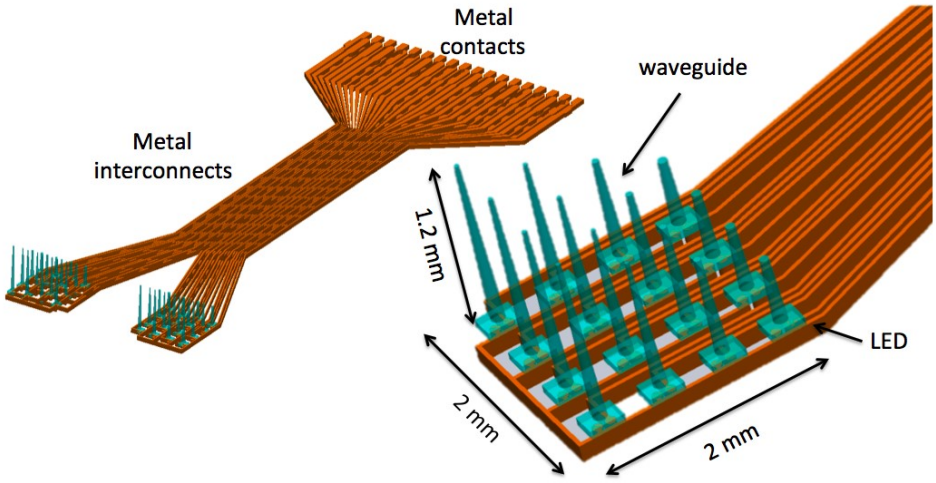

Figure 6 Conceptual diagram of the 3-D multi-waveguide probe array [17].

Figure 7 Commercialized macro-scale LED lenses, which are often comprised of a central spherical lens and a cone-shaped reflecting sidewall.

1.3 Objective

The objective of this thesis is to develop a biocompatible and flexible micro-lens-coupled LED stimulator using suitable microfabrication and integration approaches for optogenetic applications, with following requirements that need to be satisfied.

(1) A fast and versatile approach to fabrication microlenses with varied curvatures that can be coupled with μ-LEDs;

(2) Improvement on μ-LED light intensity and out-coupling efficiency

(3) Capable of stimulating neurons at an increased penetration depth;

1.4 Thesis Outline

Chapter 2 summarizes the previous work during my master study, which mainly focuses on the exploration of appropriate fabrication methods to make microlenses. Chapter 3 presents a novel technique, called vapor-induced dewetting (VID), to fabricate polymeric microlens arrays with tunable diameters and curvatures. Chapter 4 describes the structural design and fabrication processes of 1st generation of prototypes of the proposed micro-lens-coupled LED stimulators. Chapter 5 discusses the optimization of the structure of LED stimulators, as well as the optical characterization of such 2nd generation of prototypes with optimized dimensions. At the end, in Chapter 6 the thesis will be summarized with an outlook of future work and the contribution will be provided.

CHAPTER 2 Previous Work

2.1 Surface Tension Modification by Plasma Treatment

Surface tension is one of the most important attributes of materials. It strongly influences the morphology how a liquid presents on a substrate. Because droplets are always formed to be nearly spherical caps, contact angles (CAs), especially water contact angles (WCAs), are often used to characterize the surface tension. Such droplets also offer the possibility of serving as optical lenses directly. For a given system of solid, liquid, and vapor at a given temperature and pressure, the equilibrium contact angle is unique. Therefore, an effective method which can modify the surface tension is required in order to tune the contact angle of the liquid as needed, resulting in various lens curvatures.

Many efforts have been devoted to the development of super hydrophobic surfaces, which have WCAs higher than 150 °. Materials with low surface energies, such as polytetrafluoro-ethylene (PTFE) [22], are often utilized as the outermost layer to increase hydrophobicity. Such coatings, however, greatly limit the possibility of successive processing and/or patterning of substrates. Hence, controlling and tailoring surface wettability directly on original materials is desired for satisfying diverse applications. Two well-established models proposed by Wenzel [23] and Cassie [24] demonstrate a strong correlation between micro- and nano-scale surface morphology and a material's wetting behavior. Inspired by this concept, a variety of engineered surfaces have been reported, utilizing well-defined structures—such as nanotube arrays [25, 26], micro-pillar patterns [27] and the dual-scale micro- and nano-textured surfaces [28-30]—to achieve super hydrophobicity, as shown in Figure 8. However, most of these surfaces require multi-step processes and thus are complicated and expensive.

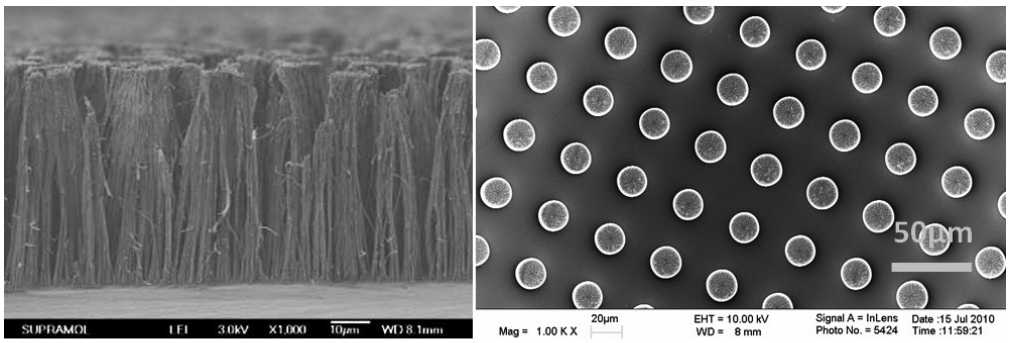

Figure 8 Previously reported fabricated super hydrophobic surfaces. (a) Nanotube arrays [25]; (b) a hierarchical dual-scale textured surface [30].

One well-developed surface processing technique is plasma treatment, which can modify only the most external molecular layers of the material without affecting bulk properties. This process is versatile and can be easily applied on devices with various surface topologies. Many types of plasmas have been found to be effective in altering the surface wettability [31-34]. Nevertheless, in most of the experiments exploring super hydrophobicity, plasma treatment (if employed) is only partially involved as one step of multi-step processes [29, 30]. Plasma treatment alone, despite its convenience and time-efficiency, has not been proven effective for super hydrophobic modification.

2.1.1 Experiment

We proposed a plasma surface modification approach to modify the surface tension without altering material bulk properties, with a combination of an oxygen (O_2) plasma pre-treatment and a sulfur hexafluoride (SF_6) plasma treatment. For ease of exposition, we call this method the "consecutive-O_2-SF_6" (COS) treatment in the following sections. Compared to previously reported methods of achieving super hydrophobic surfaces, our COS treatment eliminates the

need for designing complex micro- and/or nano-structures; it is simple and compatible with conventional micro-fabrication technology and can be applied to both flat and curved surfaces.

2.1.1.1 Material

As one of the most commonly used polymeric coating materials in biomedical micro- and nano-devices [35-40], Parylene-C has a superb combination of biocompatibility, flexibility, mechanical strength and optical transparency. A unique vapor deposition process is used for the preparation of Parylene-C coatings with pinhole-free conformity and uniform thickness. Parylene-C also provides an excellent dielectric insulation and a consistent barrier against moisture and chemicals for underlying components. To date, a large number of biomedical devices, such as retinal prostheses [35] and neural probes [39], have employed Parylene-C as the packaging material (Figure 9). Despite the significant development of Parylene packaging techniques, little attention has been paid to the surface modification of Parylene-C [30, 41, 42].

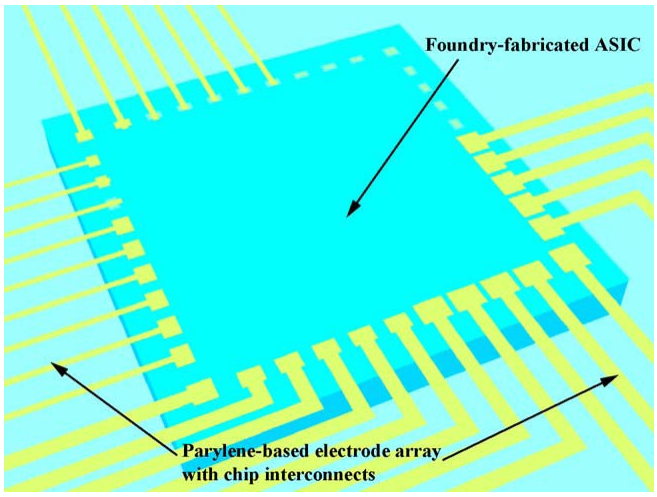

Figure 9 Parylene-C based packaged ASIC, as a part of an intraocular system for the treatment of age-related blindness [36].

Recently, Lu *et al.* reported a super hydrophobic Parylene-C surface with high and low adhesion by creating hierarchical dual-scale micro-/nano-structures [30], as shown in Figure 8(b). However, the fabrication of such dual-scale structures requires complex processes such as photolithography and DRIE etching, which is very time-consuming and not suitable for treatment on curved surfaces.

2.1.1.2 Parylene-C Deposition

Two-inch silicon wafers were chosen as the substrates and cleaned with hydrofluoric acid and deionized water prior to Parylene deposition. 5μm-thick Parylene-C films were prepared through vacuum chemical vapor deposition (CVD) using a PDS 2010 Labcoter® 2 (Specialty Coating Systems). During this process, the raw material dimer dichloro-di(p-xylylene) is first vaporized at 150 °C under vacuum and then pyrolyzed at 690 °C to generate the monomeric form chloro-p-xylylene. The monomer subsequently condenses at room temperature onto the wafer substrates in the deposition chamber to form conformal Parylene-C thin films. The thickness of Parylene-C films was determined by the amount of initial loading of dimer and verified by a profilometer.

2.1.1.3 COS Treatment

The COS treatment was performed in a reactive ion etching (RIE) system (LAM 9400, LAM Research Corporation) using O_2 plasma followed by SF_6 plasma. During the experiments, the chamber was evacuated to a base pressure of 10 mTorr before introducing the process gas with a constant flow rate of 100 sccm. A fixed radio-frequency (RF) power of 100 W was used during all plasma processes. The O_2 plasma pre-treatment of Parylene-C films was carried out

first. The treatment duration varied from 20 s to 10 min for several groups of samples. After that, SF_6 plasma was applied to the samples for 1 min. Separately, in the experimental study of switchability, a Parylene-C sample was pre-treated with O_2 plasma for 10 min, and then SF_6 and O_2 plasma treatments were alternately conducted for 1 min each on the same surface.

2.1.1.4 Characterization Methods

Both the static and dynamic WCAs were measured with a contact angle analysis system (VCA 2000, AST Products, Inc.) immediately after plasma treatments to characterize the surface wettability of modified Parylene-C films. A 2 μL droplet of deionized water was dispensed onto the Parylene-C surface with a vertical syringe. The side view of the droplet was recorded by the equipped digital image acquisition system and subsequently analyzed to determine the contact angle.

The surface morphology was characterized by an AFM (Dimension 3100, Bruker Nano). A scanning area of 3 μm by 3 μm was randomly selected on the substrates. The root-mean-square (RMS) surface roughness and quantitative three-dimensional (3-D) images were obtained. The surface chemistry on Parylene-C films was examined with an XPS (Phi 5600 ESCA system, Perkin Elmer) using a monochromatic magnesium Kα X-ray source.

2.1.2 Results

2.1.2.1 Static WCA Measurements

Prior to any treatments, the Parylene-C surface exhibited a WCA of 89.0±0.5°. Complete wetting (WCA ~ 0°) was observed after O_2 plasma pre-treatment of 40 s or longer. In this case,

the water droplet spread on the surface instantly on contact, indicating a super hydrophilic surface had been produced. This phenomenon is mainly attributed to the introduction of oxygen-related polar functional groups onto the surface during the plasma treatment [43], which is consistent with previously reported results for surface hydrophilic modification of polymers by O_2 plasma [44-46].

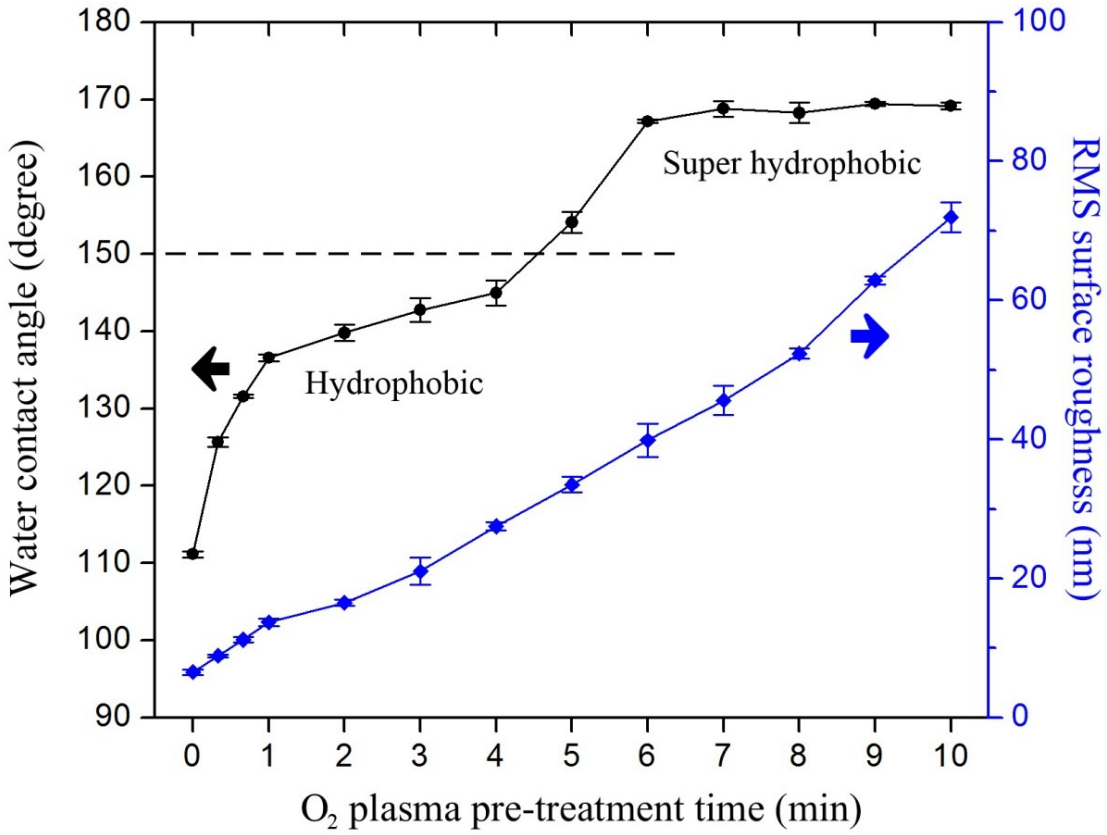

Figure 10 WCAs and RMS surface roughness on O_2 and SF_6 plasma-treated Parylene-C thin films as a function of the O_2 plasma pre-treatment time.

Subsequently, 1 min SF_6 plasma treatment was performed on the O_2 plasma pre-treated Parylene-C surfaces. The measured static WCAs are plotted as a function of O_2 plasma pre-treatment time in Figure 10. It can be seen that this brief process led to a complete inversion of

the wetting behavior on Parylene-C from hydrophilicity to hydrophobicity. The WCA became progressively higher with increased O_2 plasma pre-treatment time. It exceeded 150° when 5 min O_2 plasma pre-treatment was performed, indicating that the Parylene-C surface had turned to super hydrophobic. When the O_2 plasma pre-treatment lasted longer than 7 minutes, the WCA saturated around 169°. The highest WCA measured in our work was 169.4±0.3°.

2.1.2.2 Surface Roughness

The effects of plasma treatment on the surface morphology were examined by AFM. The change of RMS roughness is plotted in Figure 10. After polymer deposition, the fresh Parylene-C displayed a cotton-like surface with an RMS roughness of 5.772±0.376 nm. Upon exposure to the plasma, columnar structures appeared on the surface. As shown in Figure 11, the height of these structures increased with longer O_2 plasma pre-treatment time, resulting in a significant increase in the roughness. The RMS roughness increases at approximately 6.54 nm per minute of O_2 plasma pre-treatment time. On the other hand, the SF_6 plasma treatment increased the surface roughness very slightly, at about 0.76 nm per minute. This great difference can be attributed to the higher chemical reactivity of O_2 plasma with polymers, a property that makes it a popular choice for polymer etching [47, 48]. It can be concluded that the O_2 plasma treatment played a primary role in roughening the Parylene-C surface in this COS process.

2.1.2.3 Surface Chemistry

The representative XPS survey spectra and corresponding fitted high-resolution carbon 1s (C1s) spectra of Parylene-C surfaces are presented in Figure 12. Compared to the untreated Parylene-C film (Figure 12(a)), a significant increase in the oxygen (and fluorine) atomic

concentration was observed on the O_2 (and SF_6) plasma-treated surface (Figure 12(b) and (c)), which reveals the formation of new functional groups formed through the plasma-surface interaction. In the high-resolution C1s spectra, the peaks were labeled with corresponding chemical bonds where the carbon atoms were positioned. As can be seen, a number of new peaks arose after the plasma treatment. For the surface treated with only O_2 plasma, the deconvolution of C1s spectrum indicates the presence of two new peaks at 287.8 eV and 289.3 eV, which can be attributed to the carbon atoms in the free carbonyl group (C=O) and carbonate group (O_2C=O), respectively. The forming of these functional groups increased the polarity of the Parylene-C surface and thus raised the surface free energy, resulting in the improved wettability [43].

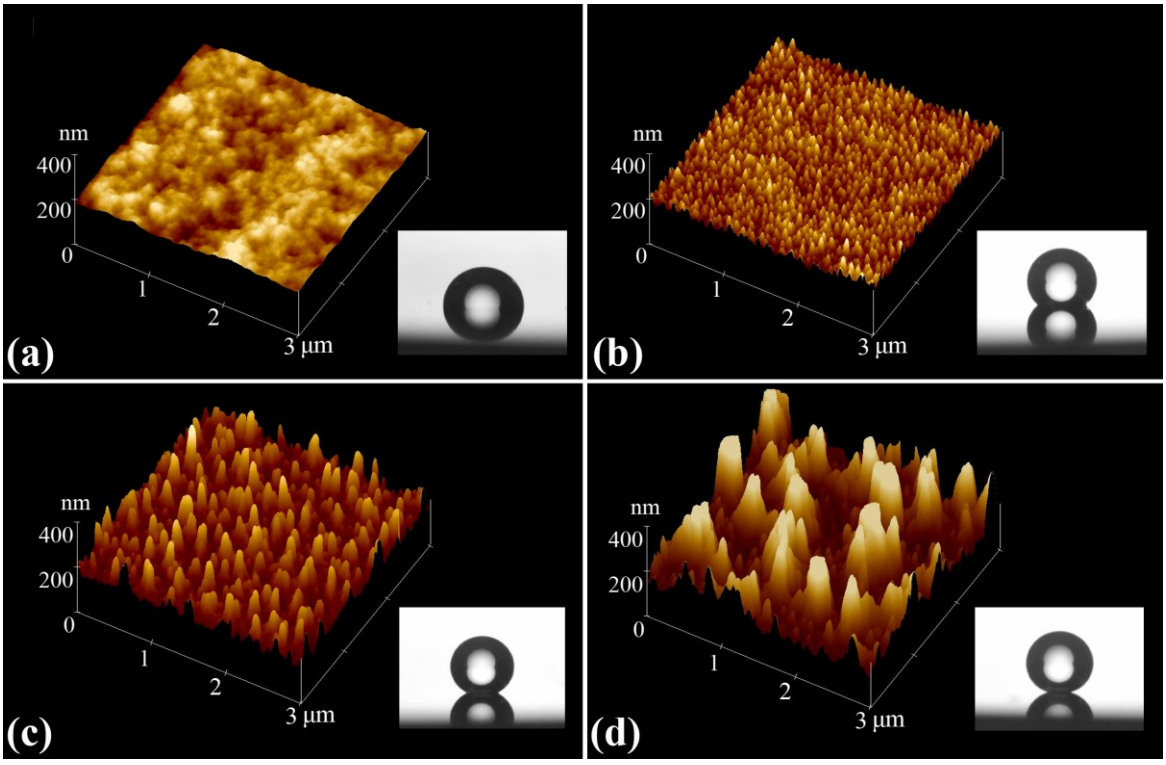

Figure 11 The representative 3-D images of Parylene-C surfaces and corresponding WCA images, with (a) no treatment, and plasma-treated with (b) 1 min O_2 + 1 min SF_6, (c) 5 min O_2 + 1 min SF_6, and (d) 10 min O_2 + 1 min SF_6.

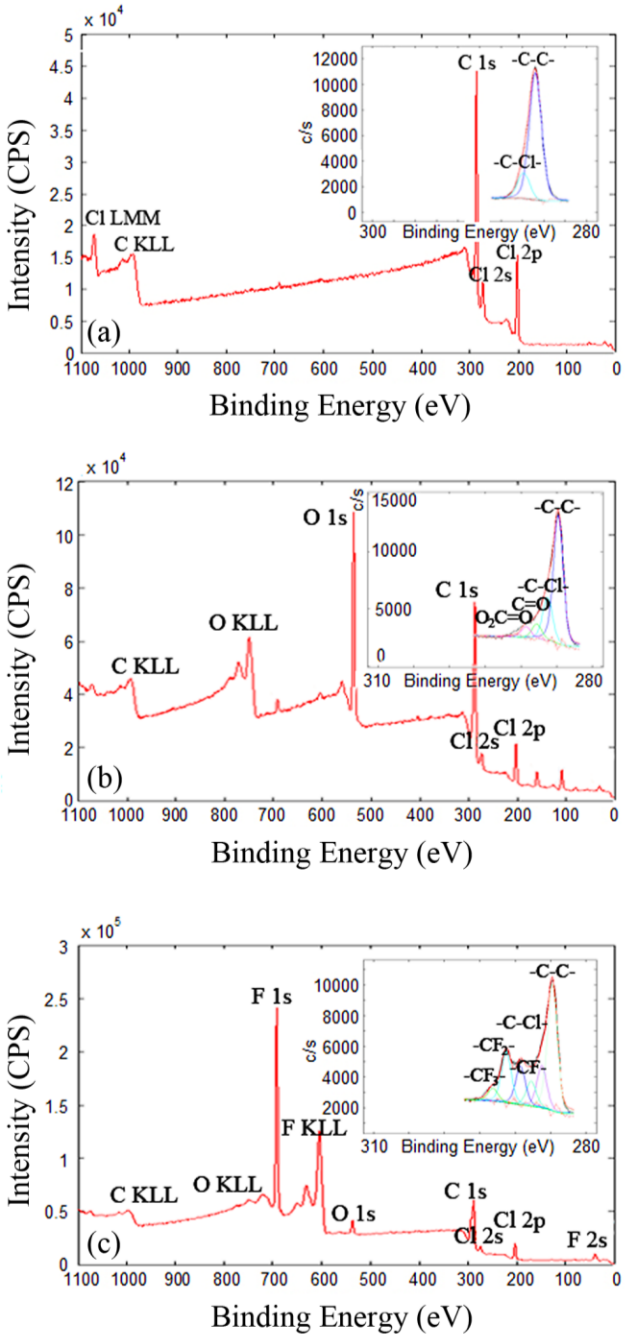

Figure 12 The representative XPS survey spectra and corresponding fitted high-resolution C1s spectra (insets) of Parylene-C surfaces with (a) no treatment, and plasma-treated with (b) 10 min O_2 and (c) 10 min O_2 + 1 min SF_6. The peaks are labeled with corresponding elements in survey spectra and carbon-related functional groups in high-resolution C1s spectra.

Similarly, new peaks representing the carbon atoms in the groups of -CF-, -F-C-Cl-, -CF_2- and -CF_3- showed up in the spectrum of the Parylene-C film that had been treated with both O_2 and SF_6 plasmas, corresponding to the peaks at 287.8eV, 289.3eV, 291.3eV and 293.2eV, respectively. Due to the chemical inertness, the fluorinated groups help lower the surface energy and thus enhance the hydrophobicity [49]. While SF_6 was selected as the main fluorinated gas source in this work, other fluorinated gases such as C_4F_8 are expected to react with the polymer surface in a similar way, as reported elsewhere [31]. It is noteworthy that the O_2 plasma treatment was a critical step prior to SF_6, which not only helped to create a rough surface but also reactivated the inert Parylene-C surface to enable subsequent chemical reaction with fluorine ions.

2.1.2.4 Switchability

We have proven previously that the COS treatment can effectively modify the surface wettability of Parylene-C films to super hydrophobicity. On that basis we proceeded to study the switchability between super hydrophobicity and super hydrophilicity through alternating one-minute SF_6 and O_2 plasma treatments on a Parylene-C sample pre-treated with O_2 plasma for 10 min. The variation of WCAs with successive treatments is shown in Figure 13. It can be seen that a 1 min post-treatment can successfully switch the surface wetting property between super hydrophilicity and super hydrophobicity. The WCAs did not show any deterioration after five cycles.

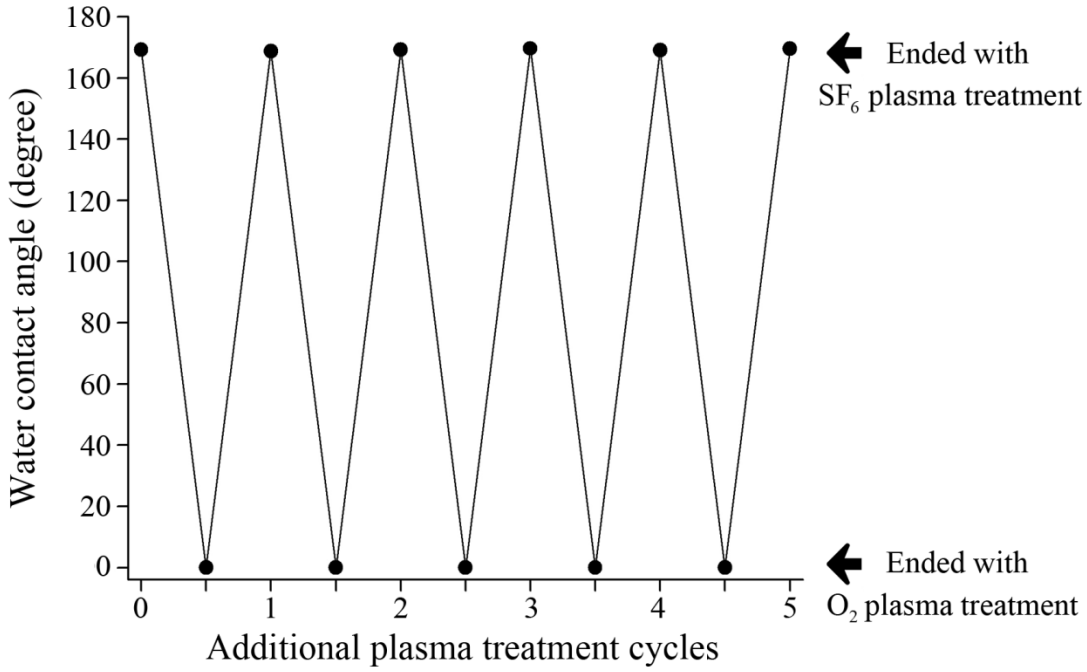

Figure 13 The switchability between super hydrophobicity and super hydrophilicity on Parylene-C thin films. The original point corresponds to the Parylene-C surface plasma-treated by 10 min O_2 + 1 min SF_6. Afterward, O_2 and SF_6 plasma treatments were alternately conducted for 1 min each on the same sample.

2.1.3 Analysis

2.1.3.1 Effect of Surface Roughness on WCA

As discussed above, the COS treatment is able to modify the surface wetting property of Parylene-C films to super hydrophobicity by enhancing the surface roughness and altering the surface chemistry. The O_2 plasma pre-treatment offers several key functions in this work. It efficiently increases the surface roughness of the Parylene-C, which is essential to achieve super hydrophobicity on a solid surface, as suggested by previous work. It also effectively activates the

inert polymer surface by forming new oxygen-related chemical bonds, which improves the efficiency of the subsequent reaction with the SF_6 plasma. The O_2 plasma treated surface exhibited a super hydrophilic property as the result of the increased surface roughness and activation. Following the O_2 plasma pre-treatment, the 1 min SF_6 plasma treatment completely converted the surface wettability to hydrophobic by introducing fluorinated functional groups, without significant change of the surface roughness.

In this section, the droplet state on such rough and hydrophobic surfaces has been investigated based on two well-established models, the Wenzel model and the Cassie model. The Wenzel model holds for homogeneous wetting (wetting contact status), where the liquid remains in full contact with the rough surface. The apparent contact angle θ_W can be given quantitatively by the Wenzel equation [23]:

$$\cos\theta_W = r\cos\theta_E, \tag{1}$$

where θ_E is the equilibrium contact angle on a flat, rigid and homogeneous surface, the wettability of which is solely dependent on the chemical composition; r is the roughness factor defined as the ratio of the actual liquid-solid contact area to the projected area on the horizontal plane. The Cassie model holds for heterogeneous wetting (composite contact status) where liquid cannot penetrate the whole surface and air pockets are trapped among the roughness peaks underneath the droplet. In this case, the apparent contact angle θ_C is given by the Cassie equation [24]:

$$\cos\theta_C = fr_W\cos\theta_E + f - 1, \tag{2}$$

where f is the area fraction of the solid-liquid contact on the horizontal projected plane, r_w is the

ratio of the actual liquid-solid contact area to the projected area, θ_E is as described in the Wenzel equation. Of these two states, the droplet usually prefers the one with the lower surface energy (in most cases, it also corresponds to the lower contact angle), which is determined solely by the surface topology. Due to the difference of contact status, the droplet in the Cassie state shows less contact angle hysteresis (defined as the difference between the advancing WCA and the receding WCA) than in the Wenzel state and thus rolls off the surface with greater ease.

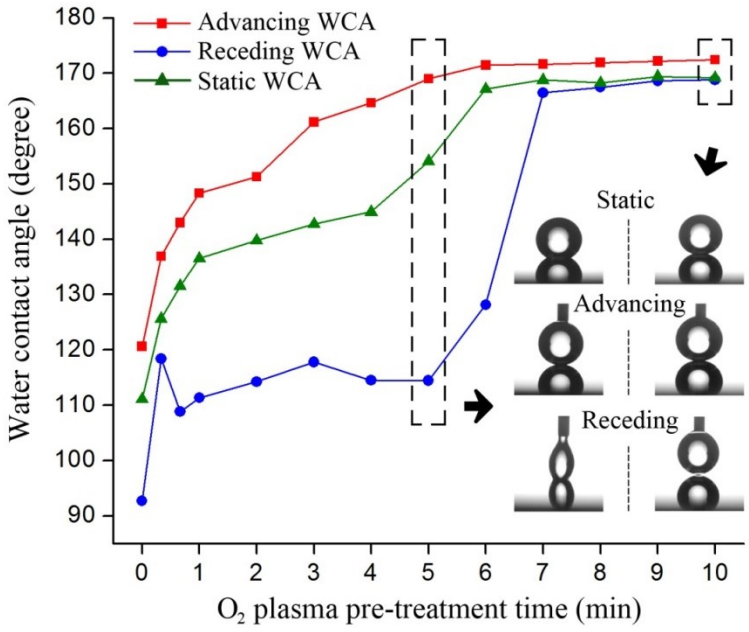

Figure 14 The advancing, receding and static WCAs on COS-treated Parylene-C thin films as a function of the O_2 plasma pre-treatment time. The insets show the representative WCA images on Parylene-C surfaces plasma-treated with 5 min O_2 + 1 min SF_6 (left) and 10 min O_2 + 1 min SF_6 (right), which correspond to the water droplets in the Wenzel state and Cassie state, respectively.

The WCA hysteresis was studied by measuring the dynamic WCAs on the COS-treated Parylene-C thin films in relation to the surface roughness induced by the O_2 treatment (Figure

14). Based on the determination of the contact angle hysteresis, the surface free energies (SFEs) of the as-treated Parylene-C solid surfaces can be estimated using the following equation [50]:

$$\gamma_s = \gamma_l(\cos\theta_r - \cos\theta_a)\frac{(1+\cos\theta_a)^2}{(1+\cos\theta_r)^2 - (1+\cos\theta_a)^2}, \quad (3)$$

where γ_s is the free energy of the solid surface, γ_l is the surface tension of the deionized water (~ 72.8 mN/m at room temperature), θ_a is the advancing contact angle, and θ_r is the receding contact angle. Figure 15 presents the predictive curve of the SFEs (γ_s), corresponding to various durations of the O_2 plasma treatment on Parylene-C surfaces.

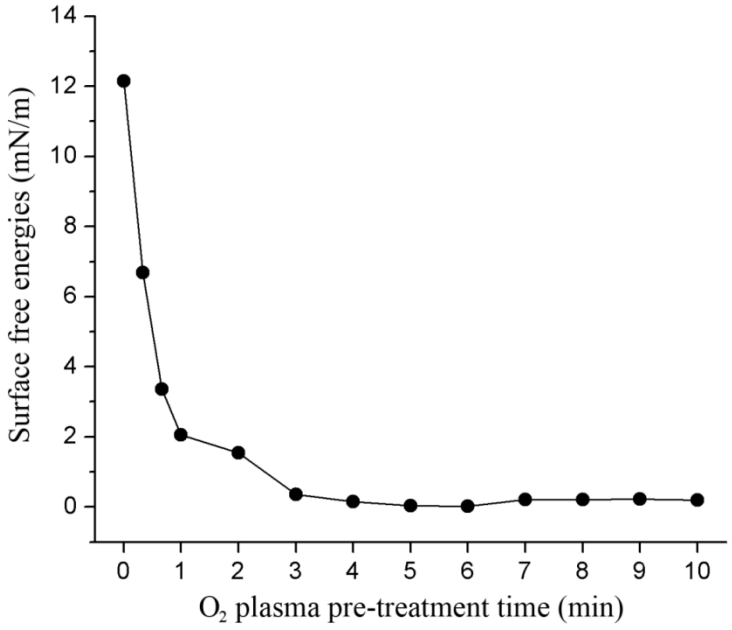

Figure 15 The predictive surface free energies (SFEs, γ_s) on COS-treated Parylene-C thin films as a function of the O_2 plasma pre-treatment time.

Furthermore, Figure 16 illustrates the relationship between the roughness factor *r* and the value of minus cosine of the static WCAs (–cosθ), as well as the WCA hysteresis. Here the

roughness factor was obtained directly from AFM analysis software through the integral of surface height distribution over the scanning area. As can be seen, two regions are clearly distinguished by the dashed line on both curves. To the left of the line, $-\cos\theta$ is linearly proportional to the roughness factor r, indicating that the Wenzel equation was followed and the surfaces were in the Wenzel state. The slope represents the value of $-\cos\theta_E$ where θ_E is the static WCA on a theoretical ideally flat (r = 1) Parylene-C surface that is chemically the same as the surface treated by O_2 and SF_6 plasmas. This value is ~0.314, indicating that the WCA on the assumed surface (θ_E) is ~108.3° (shown by the diamond in Figure 16). This approximate linearity, in accordance with Eq. (1), also implies that the surface chemistry is nearly consistent among all hydrophobic samples regardless of how long they had been pre-treated by O_2 plasma prior to SF_6 plasma treatment. Therefore, it can be concluded that the surface roughness, primarily caused by the O_2 plasma treatment, plays a dominant role in the surface wetting property and thus scales the static WCA ($-\cos\theta$) by roughness factor r. In addition, it has been found that the WCA hysteresis rises and remains above 40 degrees, further confirming the Wenzel state of the droplets. This can be explained by the pinning effect on the moderately roughened surface, which makes the surface sticky and thus increases the difference between advancing and receding WCAs.

As the roughness factor r continued to increase, $-\cos\theta$ gradually saturated in the vicinity of 0.98 and the WCA hysteresis dramatically decreased to only ~3 degrees (on the right of the dashed line in Figure 16), implying that the status of droplets has experienced a transition from the Wenzel state to the Cassie state on super hydrophobic Parylene-C surfaces. The critical point of this transition corresponds to a roughness factor of ~1.45 and a WCA of ~168°. When the roughness exceeds this critical point, the droplet cannot wet the entire surface beneath it, mainly

due to trapped air in the rough surface. Therefore, the solid-liquid adhesion weakens with a low WCA hysteresis. As a result, the droplet becomes much easier to roll off the surface, carrying away the surface contaminants.

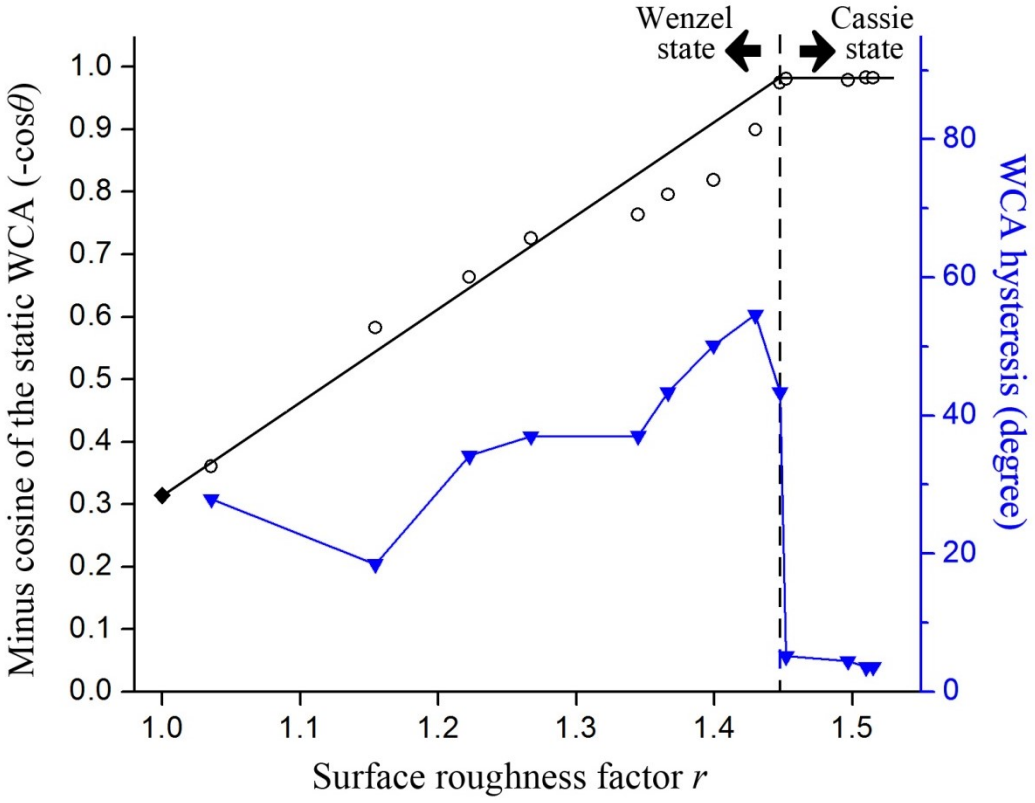

Figure 16 The value of minus cosine of the static WCA and WCA hysteresis on COS-treated Parylene-C surfaces as a function of the surface roughness factor *r*. The points also correspond to the various pre-treatment time by O_2 plasma from 0 (leftmost), 20 s, 40 s, 1 min, 2 min to 10 min (rightmost). The diamond point represents the extrapolated value on a theoretical ideally flat (r = 1) Parylene-C surface, which is chemically the same as the surface treated by O_2 and SF_6 plasmas. Two regions are distinguished by the dashed line on both curves, implying a transition of droplet status from the Wenzel state to the Cassie state.

2.1.3.2 Modeling of Surface Morphology

We have demonstrated experimentally that the surface roughness is capable of amplifying the surface wettability in the same condition of surface chemistry. Theoretical models of the plasma-roughened surface morphology have also been explored. These models could provide useful guidance in the design and fabrication of polymer surfaces with desired wetting properties. The surface topology of plasma-treated Parylene-C films was modeled and analyzed in three steps. First, we analyzed the AFM measurement results by filtering the original image upon a height threshold, as shown in Figure 17. This filtering allows us to obtain parameters, including the peak density (N), the average height of peaks (R_p) and the overall mean (M).

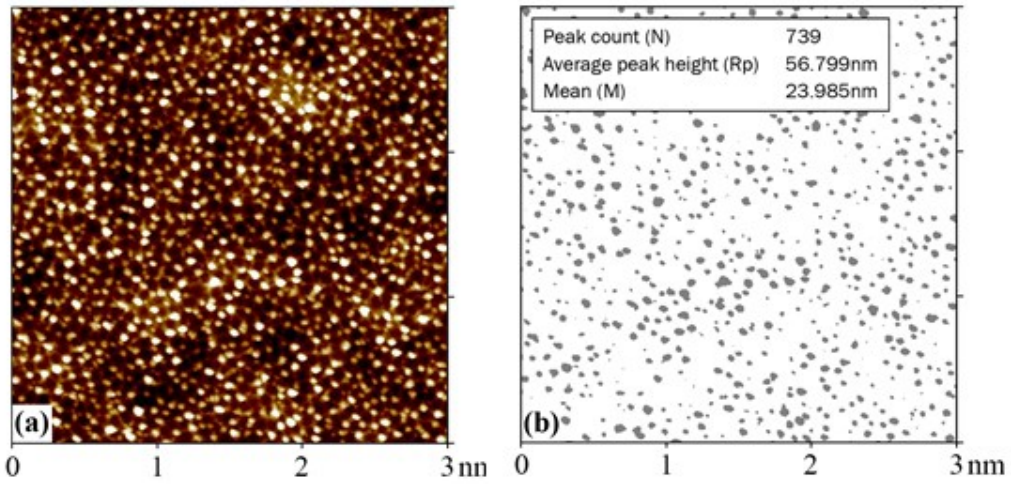

Figure 17 One example of the analysis on AFM measuremental results: (a) the original AFM image of the plasma-treated Parylene-C surface, (b) the image after the post-processing by filtering upon a height threshold on the original AFM result. Each point in (b) is considered to represent one peak on the plasma-roughened Parylene-C surface. The information such as the peak density (N), the average height of peaks (R_p) and the overall mean (M), listed in the inset, can be read directly from the software.

Second, we assumed that the plasma-treated surface was occupied by a periodic geometry. Take the square array of circular pillars as an example (Figure 18). The diameter (a), spacing (b) and height (h) were calculated based on the data from the AFM analysis (N, R_p and M) using the following equations:

$$N = \frac{9\text{nm}^2}{(a+b)^2}, \tag{4}$$

$$R_p = h, \tag{5}$$

$$M = \frac{\pi a^2 h}{4(a+b)^2}. \tag{6}$$

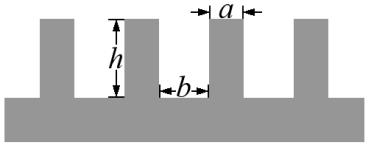

Figure 18 Circular pillars in a square array, with diameter a, spacing b and height h, which is one example of geometrical models on plasma-treated Parylene-C surfaces.

Third, the solutions of a, b and h were used to compute the theoretical roughness factor r_{M} and RMS roughness R_{M} by Eqs. (7) and (8), for comparison with the experimental data:

$$r_{\text{M}} = 1 + \frac{\pi a h}{(a+b)^2}, \tag{7}$$

$$R_{\text{M}} = \sqrt{0.25\pi a^2 (h-M)^2 + [(a+b)^2 - 0.25\pi a^2]M^2}. \tag{8}$$

It is noteworthy that for certain geometries, such as crowns and half-ellipsoids, the

roughness calculation is much more complicated than circular pillars because the employed surface integral cannot be simplified to similar expressions as Eqs. (7) and (8). In such cases, Matlab was used for the integration calculations to output the parameters r_M and R_M.

Several models have been tested with various geometrical topologies, as well as different arrangement styles, to simulate the plasma-treated Parylene-C surfaces. The models were evaluated based on the difference of the roughness factor and the RMS roughness between computed results and experimental data. Table I lists some representative surface geometrical models that have small error deviations. By comparison, the hexagonal close packing (HCP) of downward crowns was considered to be the closest model representing the surface topology of our plasma-treated Parylene-C films, with the relative error deviations of 3.79% in roughness factor and 6.31% in RMS roughness, respectively.

TABLE I

Representative surface geometrical models of
plasma-treated Parylene-C films, with small error deviations

Geometry			Relative error deviation in	
Shape	Direction	Arrangement	Roughness factor	RMS roughness
Crowns	Downward	HCP [a]	3.79%	6.31%
Cones	Upward	SCP [b]	6.80%	17.90%
Half Ellipsoids	Downward	HCP	7.68%	5.14%
Gaussians	Downward	HCP	7.52%	15.39%

[a] HCP: hexagonal close packing; [b] SCP: square close packing.

2.1.4 Summary

We have demonstrated a simple and time-efficient method in which low-powered O_2 and SF_6 plasma treatments were utilized to realize the surface tension modification. Our combination approach is able to achieve both super hydrophilic and super hydrophobic Parylene-C surfaces

without conventionally patterning micro- or nano-scale structures. Experimental results demonstrated that the physical roughening and chemical modification were the two main factors contributing to the significant variation of WCAs. The COS-treated surfaces displayed a nearly uniform chemical composition. The surface roughening treatment with O_2 plasma has been demonstrated to have a magnification effect on the surface hydrophobicity following the Wenzel equation, until the surface WCA saturates at a high value of ~169°. A transition of droplet status from the Wenzel state to the Cassie state was also observed on the hydrophobic Parylene-C surfaces, characterized by the WCA saturation and the dramatic decrease of WCA hysteresis. However, due to the evaporation, water is not ideal as the lens material unless the device is well sealed. Polymer liquids, which do not evaporate but can be cured, have the potential to replace water in lens preparation. They also show different contact angles on substrates with different surface tension, such as on the plasma-treated Parylene-C. An obstacle that appears is the difficulty in accurately dispensing a polymer liquid with a given volume by simply using a syringe or pipette due to high viscosity. Therefore, a micro-fabrication approach that is able to obtain polymer liquids with accurate volume and pattern them into spherical shapes is particularly desired.

2.2 Thermal Reflow

As an important process in micro-optics, thermal reflow is a simple and cost-effective technique by which the photoresist cylinder, created through photolithography, is baked above its glass transition temperature (T_g). This technique, which is based on mass transport, was first described by Popovic *et al.* in 1988 [51]. The molecular chain of the resist can slide past each other with ease when the temperature is above T_g, in which case the polymer is in the rubber-like

state with a stronger mobility than in the solid state. During the reflow, surface tension plays a dominant role in transforming the photoresist into the final shape, especially for micro-patterns in which case the gravitational effect is negligible. This method can help obtain high resolution without the loss of process margin. A spherical lens-shaped structure is always gradually formed during the process if circular patterns have been generated, as shown in Figure 19 [52]. The curvature of the lens is largely dependent on the baking temperature and the surface tension of both photoresist and substrate. Positive photoresists which do not crosslink are generally very suitable for the reflow.

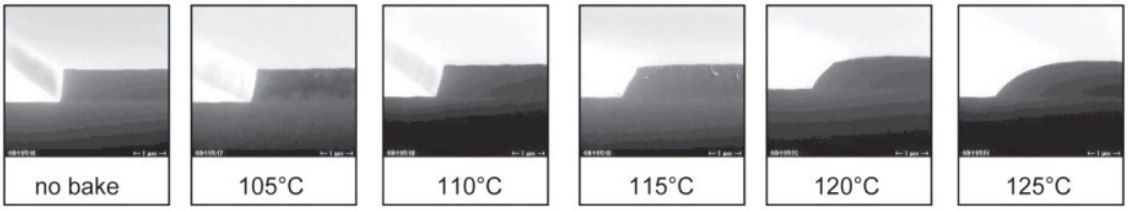

Figure 19 The evolution of the cross-section of photoresist structures during the reflow process, as the baking temperature increases [52].

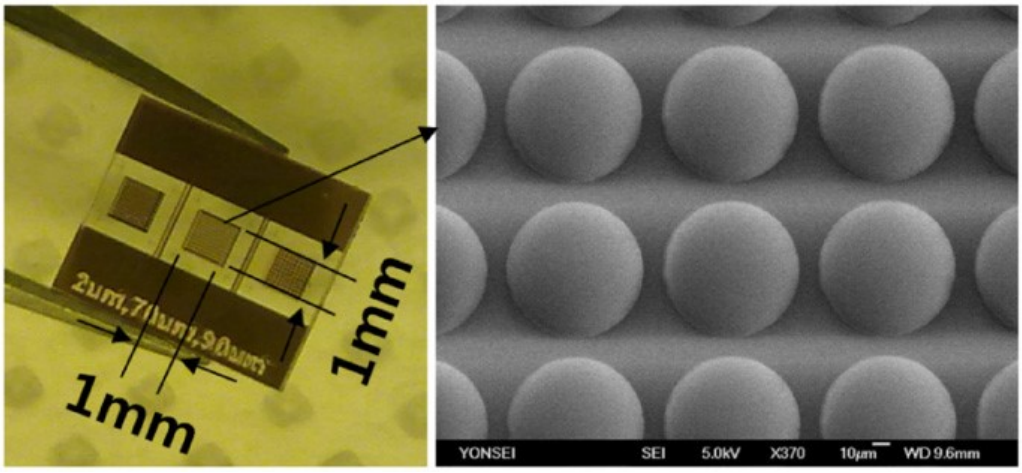

Figure 20 The reported μ-lens array with lens diameter of 80 μm fabricated through thermal reflow [53].

Fabrication of μ-lenses with diameters ranging from 5 μm up to 1 mm has been reported with thermal reflow technique [53-56]. Arrays of μ-lenses can also be produced in mass production, as shown in Figure 20 [53], which enable independent function of illumination and imaging. The variation of initial geometry can be incorporated in mask design and spin-coating process.

2.2.1 Experiment

AZ4620 was chosen as the reflow material. Several substrates with different surface tension were used for the thermal reflow process, including silicon, PDMS and Parylene-C. AZ4620 was first spin-coated at 1,000 rpm for 40 sec to obtain a layer of ~17 μm thick photoresist on substrates. The thickness can be varied by adjusting the speed of spin-coating. The samples were baked at 100 °C for 2 min and then allowed to slowly cool down until room temperature on the hot plate in order to prevent from photoresist cracking. A photomask including circular patterns with different diameters ranging from 200 μm to 500 μm was used in photolithography. The AZ4620 photoresist was exposed by UV light for 90 sec with a dosage of 1,500 mJ/cm^2. After developing, the cylinder array was achieved on the substrate. Finally, the samples were transferred into the oven and heated up to 160 °C for 3 days. The photoresist cylinders gradually reflowed and the profile was changed into a spherical lens-shape as a result of the surface tension effect. The process flow is illustrated in Figure 21.

2.2.2 Results and Analysis

2.2.2.1 Microscopic View

The micro-patterns of AZ4620 photoresist with various diameters were observed under the

microscope before and after thermal reflow process, as shown in Figure 22. It can be seen that after the thermal reflow process, the patterns look softer and smoother. The irregular edge disappeared and displaced by a smooth transition.

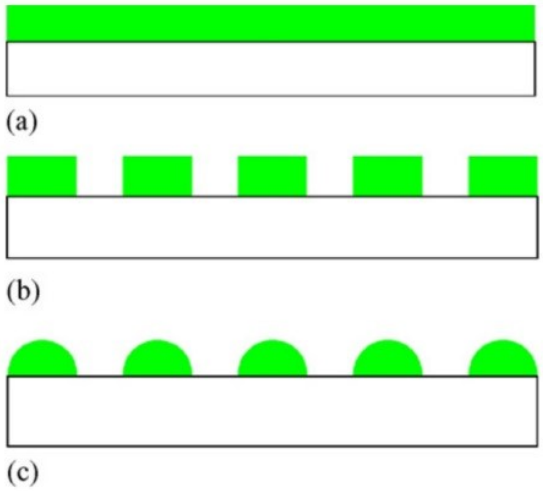

Figure 21 Schematic illustration of the formation of μ-lens array produced by photoresist thermal reflow technique: (a) AZ4620 was spin-coated on the substrate; (b) photoresist cylinders were obtained after photolithography; (c) during the reflow, the profile of patterned photoresist was changed into spherical lens-shape due to the surface tension effect.

2.2.2.2 Profile

The profile of micro-patterns on silicon substrates was measured by the stylus profilometer, as shown in Figure 23. As can be seen, the lenses were gradually formed during the reflow. For the micro-patterns with initial diameters of 200 μm and 300 μm, spherical lens-shape has been achieved after thermal reflow at 160 °C for 3 days. However, for the micro-patterns with an initial diameter of 400 μm, hollows still existed in the top middle, implying that reflow process had not finished. It can be attributed to the insufficient mobility of the photoresist. Either longer time or higher temperature is required to fully convert the pattern into the spherical lens-shape.

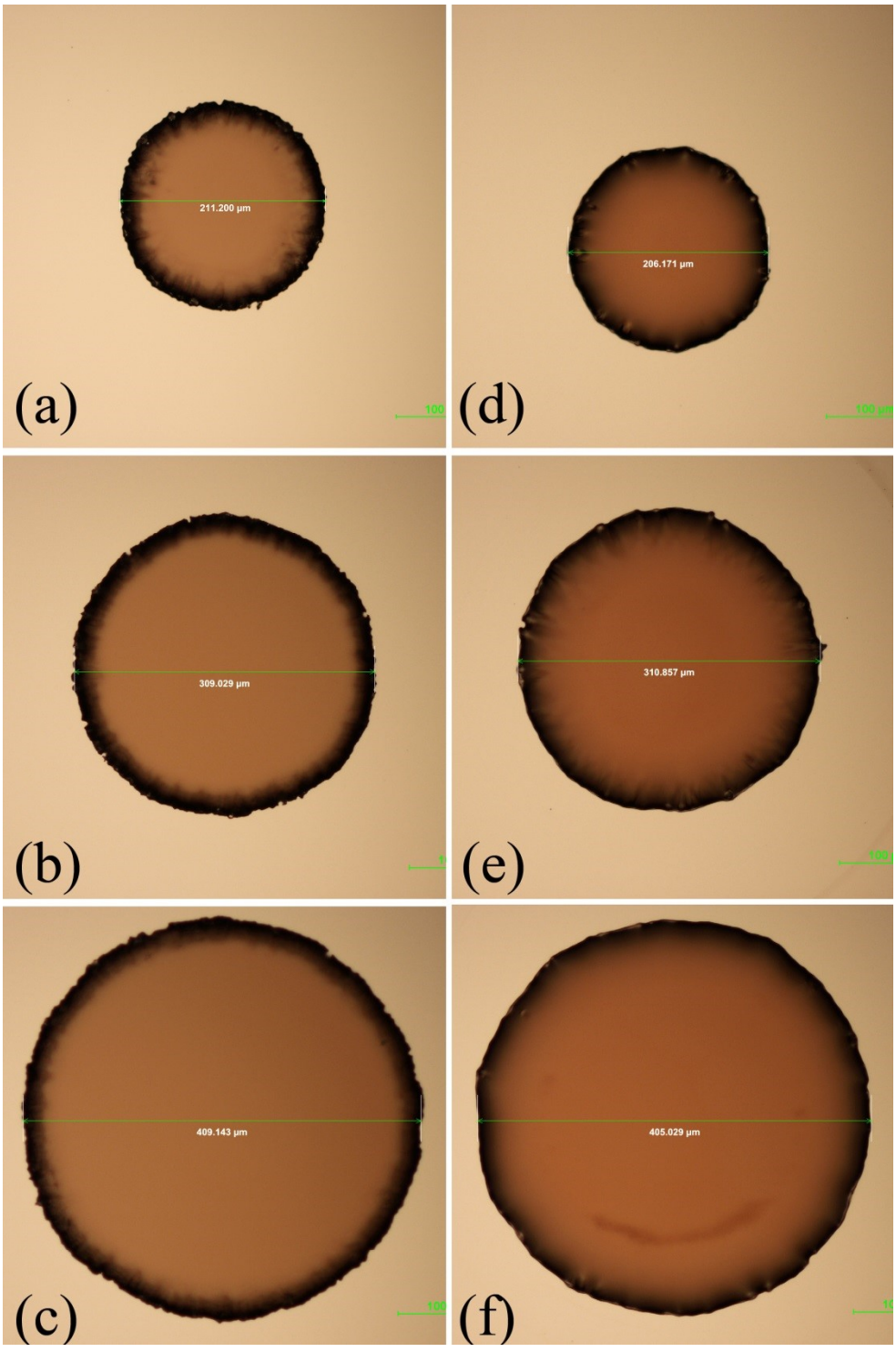

Figure 22 Microscopic view of AZ4620 micro-patterns (a)-(c) before and (d)-(f) after reflow on the silicon substrate. The diameters are (a) (d) 200 µm, (b) (e) 300 µm, and (c) (f) 400 µm, respectively.

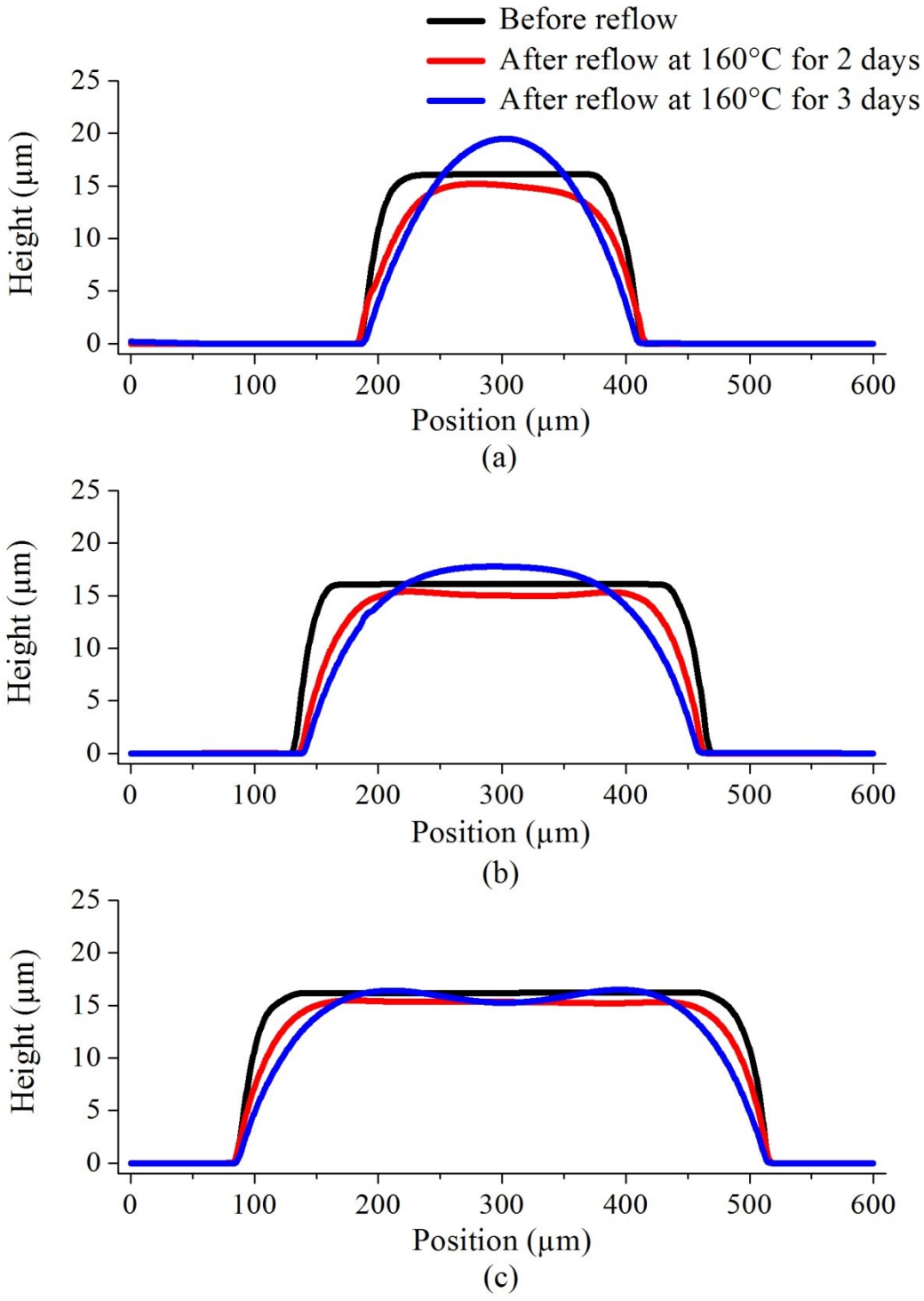

Figure 23 The profile of micro-patterns with various initial diameters of (a) 200 μm, (b) 300 μm and (c) 400 μm on silicon substrates during thermal reflow. (a) and (b) spherical lens-shape was finally achieved; (c) hollows still existed on the top middle.

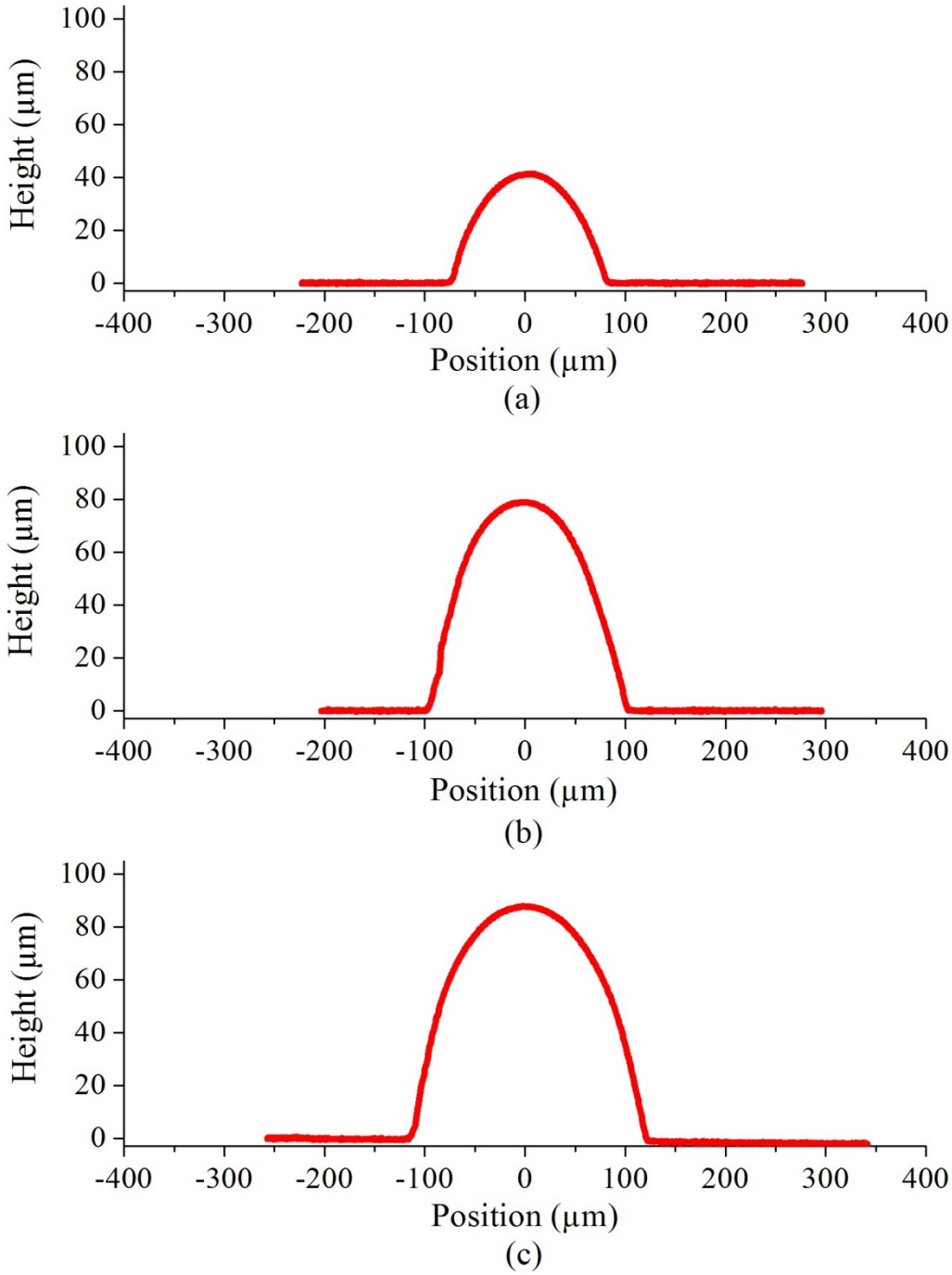

Figure 24 The final profile of μ-lenses with various initial diameters of (a) 200 μm, (b) 300 μm and (c) 400 μm on PDMS substrates after thermal reflow at 160 °C lasting for 3 days.

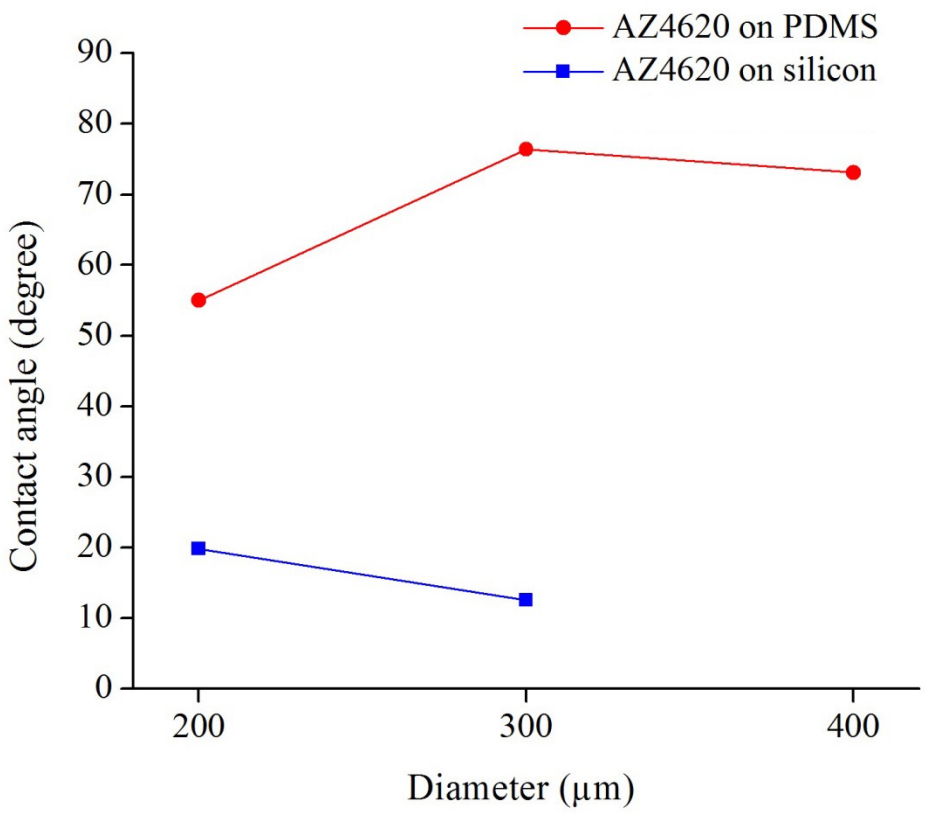

Figure 25 Contact angles of µ-lenses on silicon and PDMS substrates. The lenses were made by AZ4620 through thermal reflow process with 160 °C lasting for 3 days.

The reflow process has also been carried out on PDMS substrates, which has a lower surface tension than silicon. It is noteworthy that the measurement by profilometer could not be done before the reflow because the stylus could push the patterns off PDMS easily during the scanning, due to a low adhesion between AZ4620 photoresist and PDMS. Figure 24 shows the final profile of µ-lenses after thermal reflow at 160 °C lasting for 3 days. The spherical lens-shape has been obtained for all the samples with initial diameters of 200 µm, 300 µm and 400 µm, without the appearance of hollows on the top middle. It is also worth noting that the photoresist shrank greatly during the reflow in order to form a higher lens on the PDMS,

implying that surface tension plays an important role in the reflow process. The curvature can be estimated in terms of contact angle based on the geometry of spherical cap. Figure 25 summarizes the contact angle of μ-lenses made by AZ4620 through thermal reflow process. The photoresist exhibits a contact angle of ~70 ° on PDMS substrate, which is much larger than that on silicon substrate.

2.2.2.3 SEM Images

The morphology of fabricated μ-lens array was observed by scanning electron microscopy (SEM). The SEM images of μ-lenses with an initial diameter of 200 μm on silicon, PDMS and Parylene-C substrates are shown in Figure 26.

2.2.3 Summary

The μ-lens array made by photoresist AZ4620 has been achieved through thermal reflow technique. The photoresist was patterned by photolithography and then baked over its glass transition temperature for a couple of days. Surface tension plays an important role in the evolution of the profile of micro-patterns during reflow. A spherical lens-shape can be obtained if the driving force is strong enough for the mass transport. Because thermal reflow process is only suited for positive photoresist and common positive photoresists such as AZ4620 are not transparent, soft lithography needs to be combined to transfer the lens-shape and duplicate it by other transparent materials for optical applications. In addition, another disadvantage of thermal reflow technique is the high temperature, such as 160 °C in the previous experiment, which could likely cause permanent damage to the device.

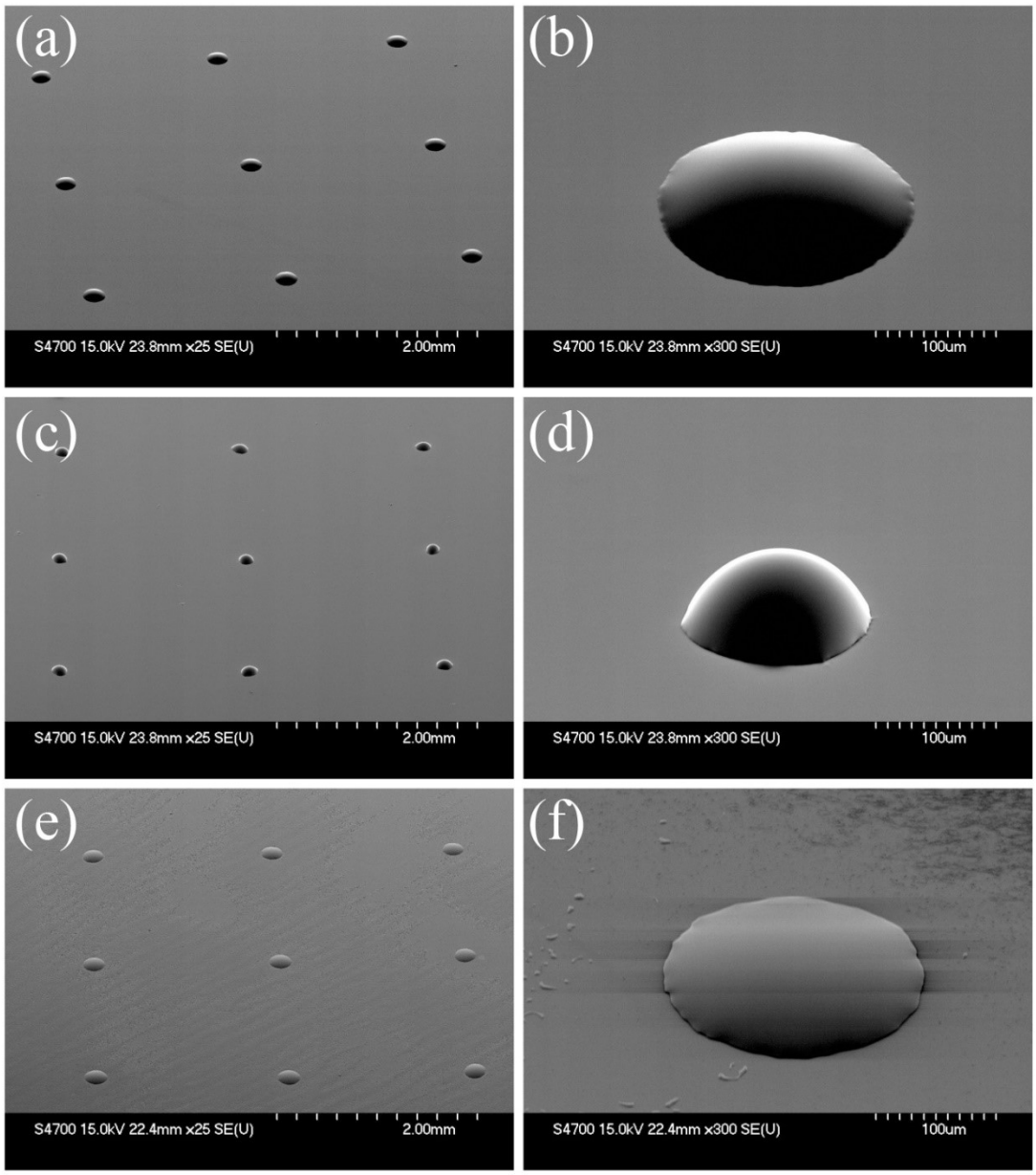

Figure 26 SEM images of fabricated μ-lens array and single μ-lens with an initial diameter of 200 μm on (a) silicon, (b) PDMS, and (c) Parylene-C substrates. Such μ-lens array was made by photoresist AZ4620 and achieved through the thermal reflow technique.

CHAPTER 3 Fabrication of Microlens Arrays through Dewetting

3.1 Background

A variety of strategies have been developed for fabricating microlens arrays. Technically, they can be classified into two categories: photolithographic [57, 58] and surface-tension-assisted [55, 59-61] technologies. The former applies improved photolithographic methods to adjust the profile of ultraviolet (UV) light distribution and directly create 3-D microlens patterns on photoresists through a single exposure. For example, Totsu et al. employed a unique grayscale mask with a transmission gradient to generate a microlens array through photolithography [57]. Manevich et al. proposed using gap photolithography with an optimized distance between the photoresist film and the illuminated mask surface to make microlens arrays [58]. However, some optical issues, such as mask resolution and light scattering, greatly limit the quality of microlenses fabricated by such methods. On the other hand, surface-tension-assisted technologies, such as the most commonly used ink-jet printing and photoresist thermal reflow methods, take advantage of surface tension to form spherically shaped microlenses with smooth profiles. Ink-jet printing, frequently operated in the drop-on-demand (DOD) mode, is a highly automated process (as shown in Figure 27) with which patterns of microlenses can be written directly onto a substrate by dispensing droplets of an optical material at target positions [59-61]. Nevertheless, the difficulty of aligning microlenses on pre-patterned substrates is a major obstacle. In the approach of photoresist thermal reflow (Figure 28), photoresist micro-cylinders are first created by conventional photolithography and subsequently baked above the glass transition temperature (T_g) of the photoresist to transform the cylindrical shape into the spherical lens shape through reflow [55]. Micro-printing or reactive ion etching (RIE) is often followed for

lens replication to transfer the microlens profile into other materials with appropriate optical properties. However, besides high processing temperatures, the complexity of multi-step fabrication could affect the repeatability and yield of production.

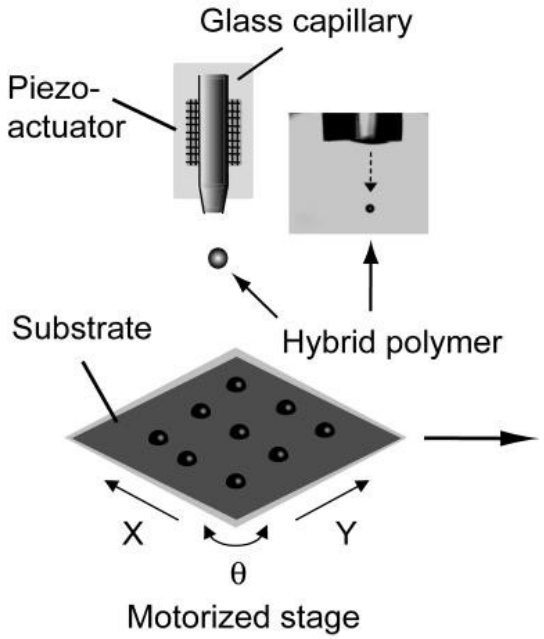

Figure 27 Schematic illustration of the DOD ink-jet printing [59].

Dewetting is another surface-tension-assisted technology that has been considered as one of the most promising strategies in surface patterning [62-64]. It is a common phenomenon that water is reluctant to be everywhere when used to flush some non-hydropholic surface. It often forms a number of droplets ramdomly on certain spots. In fact, more generally, a thin liquid coating tends to break up and fails to remain continuous on the surface if the spreading coefficient is negative [65]. This phemomenon is called “reticulation” or “dewetting”, in which an initially uniform film of a liquid breaks up, retracts, and eventually transforms into isolated droplets on a solid substrate. It is driven by the minimization of surface energy and typically occurs at the solid-liquid interface. However, due to lack of mobility, the dewetting phenomenon

does not always occur on highly viscous polymer liquid films at room temperature. Thermal annealing above T_g of polymers is commonly used to activate the dewetting by increasing the mobility of polymer chains [66, 67].

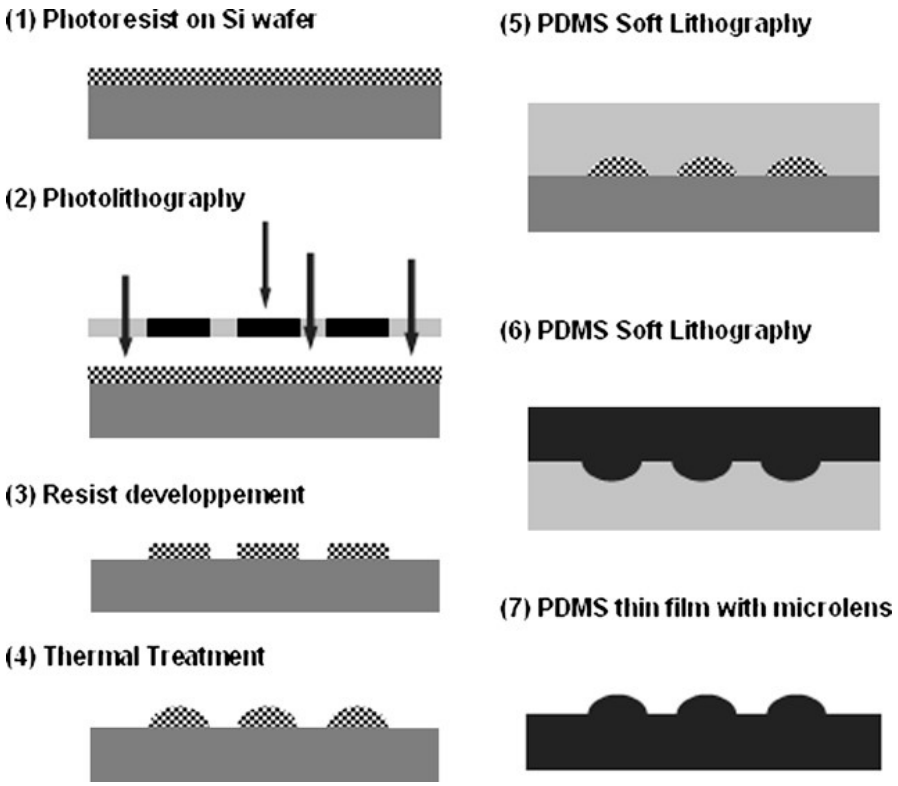

Figure 28 Schematic representation of PDMS microlens array fabrication using photoresist thermal reflow process and a double replica molding process [55].

In an ordinary dewetting process that takes place on a flat and homogeneous substrate, a random distribution of ramified droplets is usually generated at the late stage, which is a major limitation for many applications. Therefore, advanced technological approaches are particularly desired in order to control the location of dewetted structures and create well-aligned microlens arrays. Several research groups have demonstrated that topological patterning on substrates is able to modulate the organization of dewetted structures [52, 68-70]. Some groups have prepared

chemically patterned substrates with periodic surface energy contrast to induce 1-D pattern-directed dewetting and thus roughly confine the final droplets [71, 72]. However, these methods cannot precisely control the position of dewetted droplets, which could greatly increase the difficulty of successive integrations. Although significant efforts have been devoted to the development of advanced approaches and mechanisms of dewetting [52, 68-74], there have been few dewetting experiments on chemically patterned surfaces for the fabrication of self-organized and well-aligned microlens arrays.

3.2 Theory and Simulation

We proposed a simple, rapid and cost-effective approach to fabricating microlens arrays on polymeric surfaces. Vapor-induced dewetting of SU-8 thin films was carried out on biocompatible heterogeneous polydimethylsiloxane (PDMS) substrates that were selectively pre-treated with low-energy sulfur hexafluoride (SF_6) or oxygen (O_2) plasma.

As a preliminary study, a numerical simulation was first performed to examine the dewetting process on an ordered, chemically heterogeneous substrate by using a lubrication-based computational model [75]. The thickness profile of the liquid film is represented by the function $h(x, y, t)$, where x and y are spatial coordinates and t is the time. The liquid film is assumed to be non-volatile so there is no volume loss during the dewetting process. Based on the conservation of volume, the evolution of the film thickness h is governed by the continuity equation:

$$\frac{\partial h}{\partial t} = -\nabla \cdot Q, \tag{9}$$

where Q denotes the horizontal flux and $\nabla\cdot$ is the two-dimensional divergence. Applying the lubrication approximation (i.e., slow-flow and small-slope) to the Navier-Stokes equation, Q is proportional to the pressure gradient, expressed by [76]:

$$Q = -\frac{h^3}{3\mu}\nabla p\,, \tag{10}$$

where μ is the dynamic viscosity, which is assumed to be constant across the thin liquid film. The pressure p includes capillary, gravitational and disjoining contributions:

$$p = -\sigma\nabla^2 h + \rho g h - \Pi\,, \tag{11}$$

in which σ is the surface tension, ρ is the density, g is the acceleration of gravity, and Π presents the so-called disjoining pressure with a widely-used form introduced by Schwartz and Eley [75]:

$$\Pi = \frac{(n-1)(m-1)}{h_0(n-m)}\sigma(1-\cos\theta)\left[\left(\frac{h_0}{h}\right)^n - \left(\frac{h_0}{h}\right)^m\right], \tag{12}$$

describing the interaction of the liquid with the substrate. Here, h_0 is the characteristic thickness, which is very small compared to the average thickness of the dewetting film and typically in the range of 1 to 100 nm [75]. n and m are positive constants with $n > m > 1$. Therefore, Π is governed by a long-range attractive potential and a short-range repulsive potential. $\theta(x, y)$ denotes the equilibrium contact angle and its position dependence represents the heterogeneity on the substrate. Combining Eqs. (9) to (12) yields the final form of the fourth-order non-linear evolution equation for the thickness profile:

$$h_t = -\nabla \cdot \left[-\frac{h^3}{3\mu} \nabla \left(-\sigma \nabla^2 h + \rho g h - \frac{(n-1)(m-1)}{h_0 (n-m)} \sigma (1-\cos\theta) \left[\left(\frac{h_0}{h} \right)^n - \left(\frac{h_0}{h} \right)^m \right] \right) \right]. \quad (13)$$

The computational domain is sketched in Figure 29(a), which includes a 3 × 3 array of hydrophilic circular patterns with a diameter of 120 μm and a pitch of 250 μm on a hydrophobic substrate. Such specific geometry was chosen to model the pattern dimension on the photomask, which will be employed in the experiment later. The contact angles on circular patterns and remaining substrate were set to 0.1 rad and 0.5 rad, respectively. The liquid properties μ = 0.0699 Pa·s, σ = 0.0334 N/m, and ρ = 1.075 g/mL corresponded to the actual value of SU-8 3005 (MicroChem Corp.). In addition, parameters (n, m, h_0) = (3, 2, 50 nm) were used in this study.

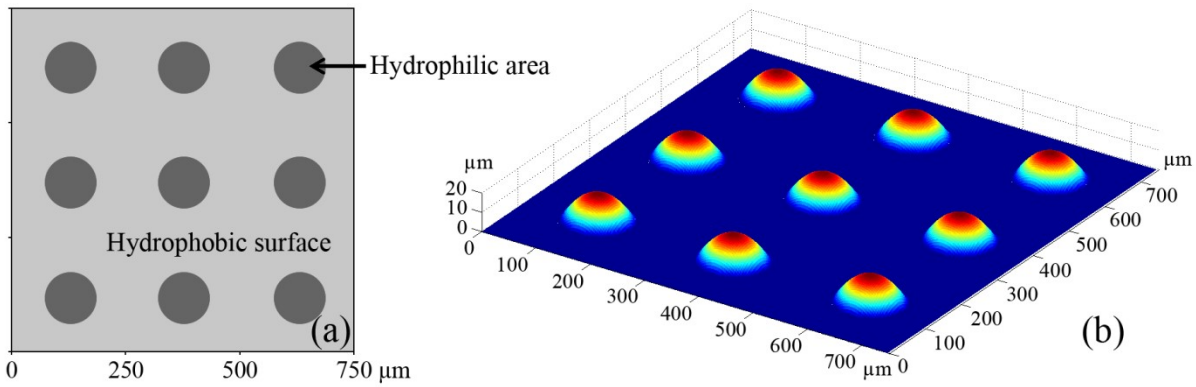

Figure 29 (a) A schematic of the computational domain, which includes a 3 × 3 array of hydrophilic circular patterns on a hydrophobic substrate. Symmetry conditions were applied along all boundaries to simulate an ideal infinite array. (b) 3-D simulation result for the dewetting process. A self-organized microlens array was formed on the final profile, occupying the ordered hydrophilic areas.

Eq. (13) was solved numerically using a finite-element algorithm by applying the

alternating direction implicit (ADI) scheme and Newton's method (second-order Crank-Nicolson scheme) [77]. Nonlinear factors were evaluated at the previous time level. A 200 × 200 mesh was used with a mesh size of 3.75 μm, and an adaptive time-stepping procedure was employed to increase the computational efficiency. The initial condition included a liquid film with a uniform thickness of 1 μm and an introduced dry spot. Symmetry conditions were applied along all boundaries to simulate an ideal infinite array. The 3-D simulation result is shown in Figure 29(b). As can be seen, a self-organized microlens array was formed on the final profile, occupying the ordered hydrophilic areas as expected. This simulation provides qualitative guidance for the following fabrication technology.

3.3 Experiment

3.3.1 Methods to Generate Heterogeneity

The nature of wetting on a surface is of crucial importance in the dewetting behavior of liquid thin films. In our experiment, polymeric substrates with heterogeneous surface wettability were first created using a low-energy plasma treatment in order to induce the self-organization of microlenses in the subsequent dewetting process. Based on the previous study in Chapter 2.1, plasma treatment offers a facile route to alter the surface wettability. It can modify only the most external molecular layers of the material without affecting the bulk property. The SF_6 and O_2 plasma treatments have been found to be effective in tuning the polymer surface into hydrophobicity and hydrophilicity, respectively. Such changes in the surface wettability can be attributed to the variation of both surface roughness and surface chemistry induced by the plasma.

3.3.2 Materials and Fabrication

A typical fabrication process is schematically illustrated in Figure 30. Biocompatible Parylene-C thin films were prepared through vacuum chemical vapor deposition (CVD) on 2-inch silicon wafers using a PDS 2010 Labcoter® 2 (Specialty Coating Systems). A thickness of ~2 μm was deposited and verified by a profilometer. After that, the mixture of PDMS pre-polymer (Dow Corning Sylgard® 184) and curing agent (10:1 by weight) was degassed in a vacuum chamber, spun onto the Parylene-C coated surfaces at 5,000 rpm for 40 s, and then baked at 110 °C for 10 min, in order to obtain PDMS thin films with a thickness of approximately 10 μm. Subsequently, SF_6 plasma was applied to treat the PDMS surface for 40 s with a flow rate of 20 sccm and an RF power of 100 W, using a plasma etcher (PX-250, March Instruments). This SF_6 plasma treatment converted the PDMS substrate to a super hydrophobic surface. After that, photoresist S1813 (Microposit™) was spin-coated at 2,000 rpm for 40 s and baked at 110 °C for 1 min on a hot plate. Through conventional photolithography, the photoresist was patterned to expose openings on substrates as the target positions for microlenses. For the proof-of-concept, a 200 × 200 array of circular patterns with a diameter of 120 μm and a pitch of 250 μm was designed and utilized as a photomask. After the UV exposure and the following development, an O_2 plasma treatment was carried out for 40 s with a flow rate of 15 sccm and an RF power of 100 W, in order to switch the wettability of the exposed PDMS surface from hydrophobicity into hydrophilicity. It is noteworthy that such a brief and low-powered plasma treatment led to an increased surface roughness of only ~2 nm, and thus the substrate exhibited little topological variation. After the removal of the remaining photoresist, PDMS substrates with non-uniform wettability were achieved. Thin SU-8 films (MicroChem Corp.) were immediately spun onto the plasma pre-patterned substrates to avoid the recovery of hydrophilic PDMS

regions in air. The high transparency of SU-8 at visible wavelengths makes it suitable for integrated optical applications. A series of SU-8 3000 photoresists were prepared to contain 30, 40, 50, and 60 wt.% resin by diluting the resin in the SU-8 thinner (cyclopentanone, MicroChem Corp.), followed by spin-coating at 1,000 rpm for 40 s to obtain SU-8 thin films with approximately 6, 10, 20, and 30 μm thickness, respectively.

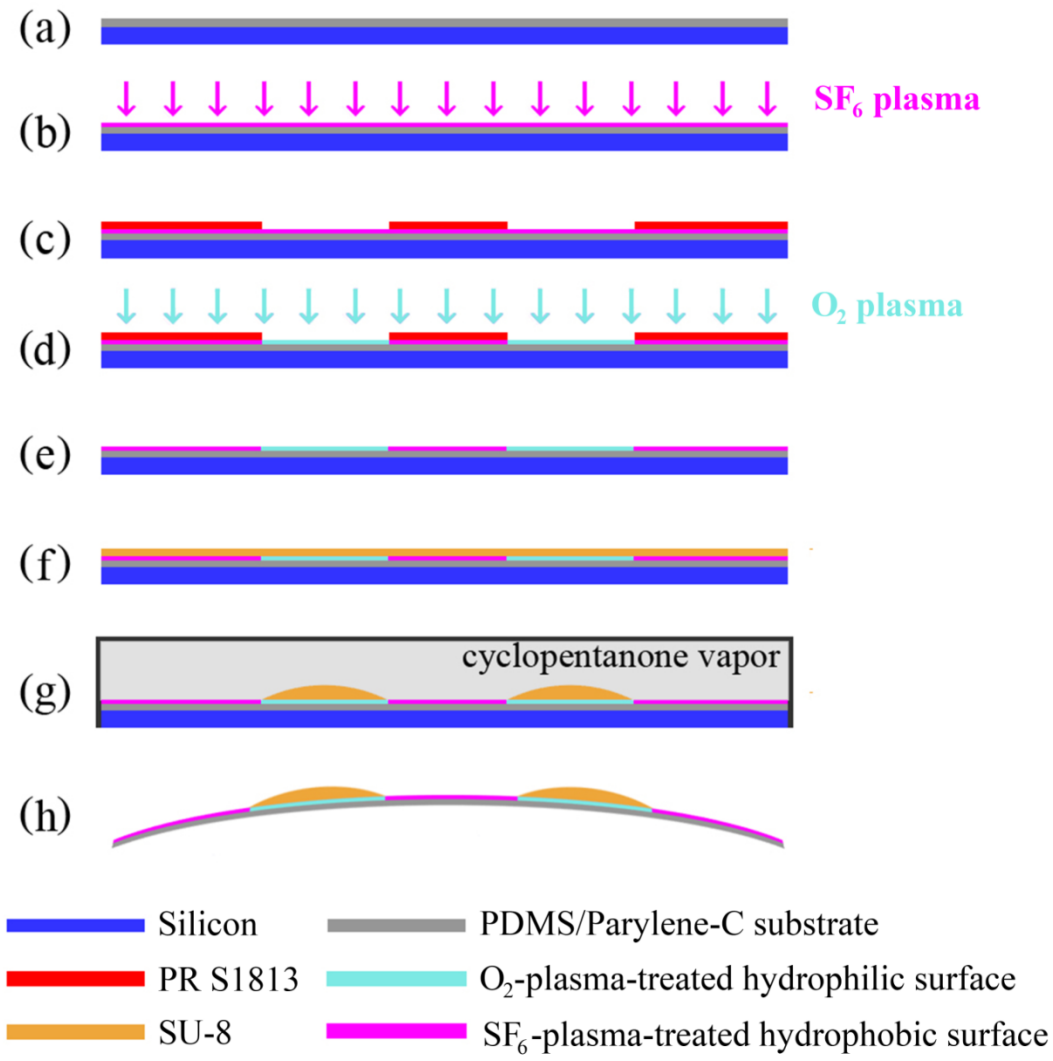

Figure 30 Schematic illustration of vapor-induced, room temperature dewetting process.

Figure 31 shows the experimental setup of the vapor-induced dewetting process. The

samples were placed into the vapor atmosphere of cyclopentanone to initiate dewetting. They were elevated by a small support to avoid contact with the solvent liquid. This process was performed at room temperature, except when specifically mentioned, in which case a hot plate was utilized to heat the liquid of cyclopentanone. The progression of dewetting was monitored through a stereo microscope (AmScope) equipped with a CCD camera. After the completion of dewetting, the samples were removed from the setup and cured by exposing the dewetted patterns to UV for 1 min.

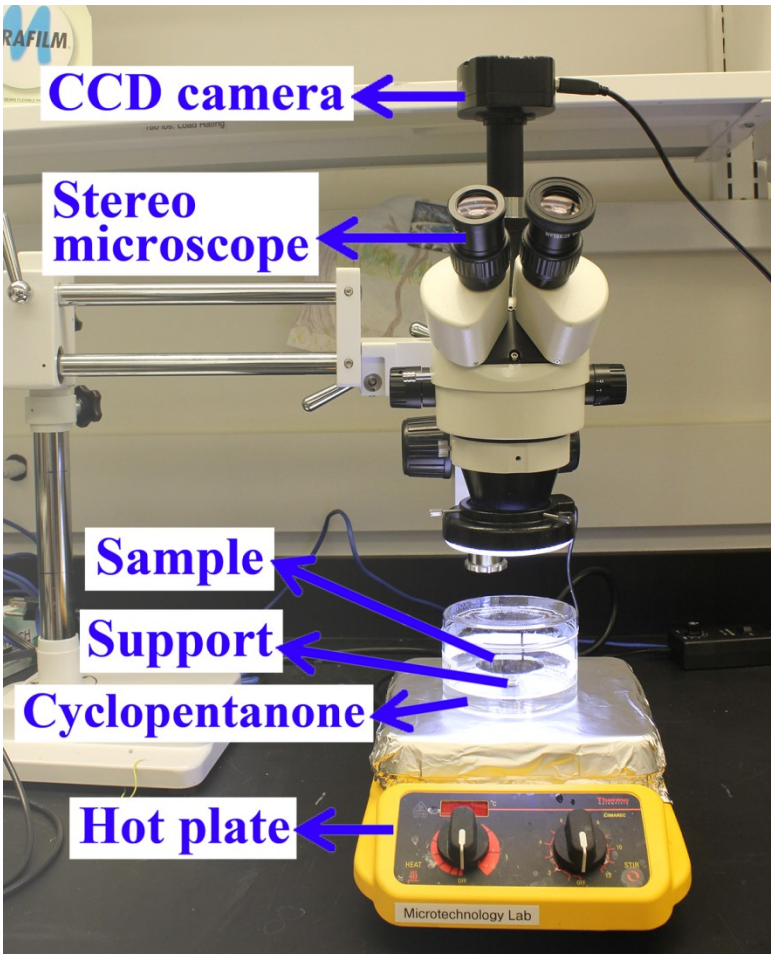

Figure 31 The experimental setup for vapor-induced dewetting.

3.3.3 Characterization

Water contact angle (WCA) measurement was conducted to confirm the wettability of untreated and plasma-treated PDMS surfaces with a contact angle analysis system (VCA 2000, AST Products, Inc.). The morphology of microlens arrays was inspected by a scanning electron microscope (SEM, Hitachi S-4700 II FESEM), and the lens curvature was measured by a stylus surface profiler (Dektak^3, Veeco Instruments, Inc.). Ten microlenses randomly selected from each array were scanned in order to verify the uniformity. The optical characterization was performed by examining the imaging capabilities of microlenses under an optical microscope (Eclipse LV100, Nikon).

3.4 Results

3.4.1 WCA Measurement

The surface wettability on PDMS substrates was inspected by measuring the WCAs before and after the plasma treatments. Prior to any treatments, the intact PDMS surface exhibited a WCA of 109.3 ± 0.4°. The hydrophobicity of the PDMS was enhanced through the SF_6 plasma treatment, with a WCA of 155.8 ± 1.6°. The following O_2 plasma treatment led to a complete inversion of the wettability of the PDMS surface where a complete wetting (WCA ~ 0°) was observed. These findings are consistent with previously reported results for surface wettability modification by SF_6 and O_2 plasmas.

3.4.2 Progression of Dewetting

Figure 32 presents a sequence of microscopic images to show the evolution of the

morphology of a ~20-μm-thick SU-8 liquid film during the vapor-induced, room temperature dewetting process. It can be seen that dewetting originated from the position where defects or impurities existed. As shown in Figure 32(a), the initially smooth thin film broke up and a circular dry hole was formed, which can be attributed to the rupture mechanism of "heterogeneous nucleation" due to a micro-scale wettability contrast [78, 79]. Such instability was manifested after 30 s exposure to the solvent vapor. After the nucleation, the dry hole grew laterally with time to form a dewetted region with a three-phase contact line progressively expanding ahead of the hole (Figure 32(b)). This was owing to the local curvature around the edge of the hole, which was higher than that on the surrounding flat film surface, resulting in a continuing net flux outwards from the edge and a retraction of the contact line [80]. When the contact line reached a hydrophilic spot, it pinned on that spot with an obvious distortion (Figure 32(c)). Such distortion increased as the contact line continued to expand, until a breakup eventually occurred around the hydrophilic spot. It has been reported that the amplitude of distortion is proportional to the size of the wetting spot. As a result, a certain amount of SU-8 polymer liquid was confined within the hydrophilic area, forming an individually isolated micro-droplet. The deformation of the contact line gradually relaxed after the breakup. The morphology of the dewetted microlens array was clearly observed under the microscope after 4 min. The borders of the SU-8 droplets matched exactly to the boundary of the hydrophilic spots on PDMS resulting from the selective surface pre-patterning through SF_6 and O_2 plasma treatments, which is in good agreement with the simulation. At the late stage, the neighboring dewetted regions coalesced as their contact lines overlapped once on contact with each other. The whole dewetting process lasted for 7 min before completion. After that, no further change was observed in the overall morphology.

3.4.3 Surface Morphology

The as-fabricated SU-8 microlens arrays were observed through SEM, as presented in Figure 33, which demonstrates the uniformity of microlens array over the entire PDMS surface. It is worth noting that the secondary droplets (also known as satellite droplets) close to each main droplet (i.e., microlens) in the array were also generated during the contact line breakup. The formation of such secondary droplets has been found to be a common phenomenon, which is strongly correlated to the ratio of characteristic instability wavelength for breakup to the length scale of the distortion [81]. In addition, their location implies the information about the motion history of dewetting.

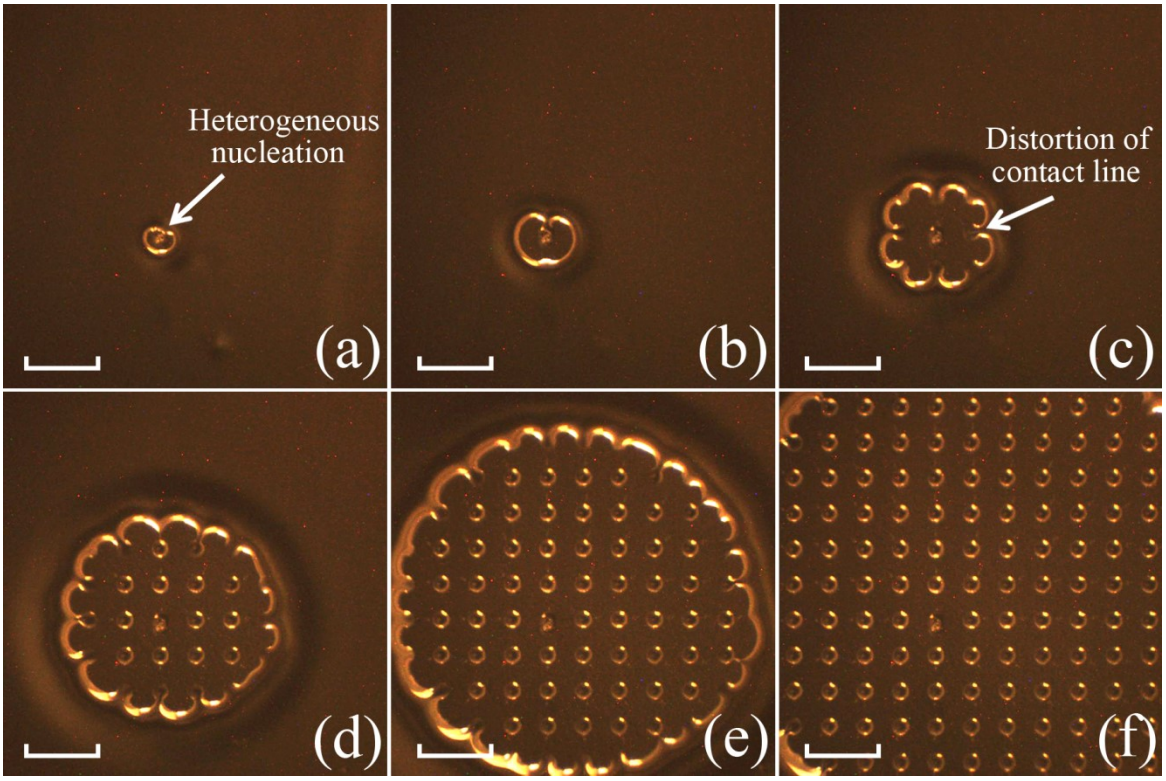

Figure 32 Morphological evolution of a ~20-μm-thick SU-8 liquid film on a chemically patterned PDMS substrate during the vapor-induced, room temperature dewetting process, with a

sequence of time intervals: (a) 1 min, (b) 2 min, (c) 3 min, (d) 4 min, (e) 5 min, and (f) 6 min. The scale bars correspond to 500 μm.

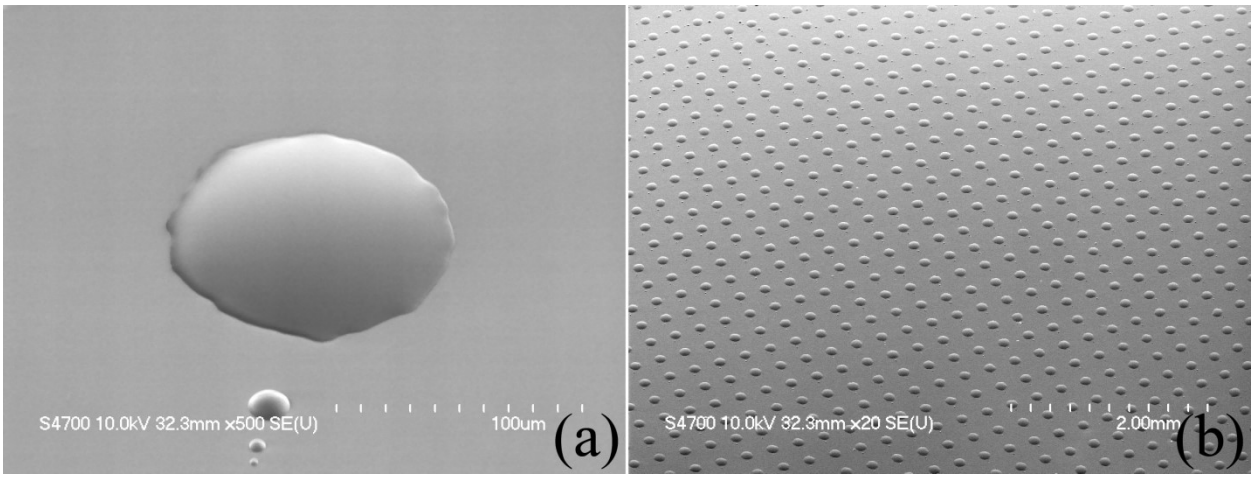

Figure 33 SEM images of (a) a single SU-8 microlens and (b) an SU-8 microlens array fabricated through vapor-induced, room temperature dewetting, with an initial film thickness of ~20 μm on a chemically patterned PDMS substrate.

3.4.4 Curvature of Microlenses

The curvature of microlenses was characterized in terms of contact angle, which was determined by the following equation:

$$\theta = 2\arctan(\frac{2h}{d}), \tag{14}$$

where d is the diameter of the base, h is the height of the droplet, and θ is the contact angle. The diameter and the height of microlenses were measured by the surface profiler, as shown in Figure 34.

The influences of the initial film thickness and the processing temperature on the microlens curvature were also investigated and plotted, as shown in Figure 35. In order to study the temperature dependence of vapor-induced dewetting, the experimental setup was placed on a hot plate with various setting temperatures (T = 40 °C, 60 °C and 80 °C), as illustrated in Figure 31. It is evident from Figure 35 that the microlens curvature is strongly correlated to the processing temperature but nearly independent of the initial film thickness. The contact angle increases from ~27° to ~47° as the processing temperature rises from 20 °C (i.e., room temperature) to 80 °C.

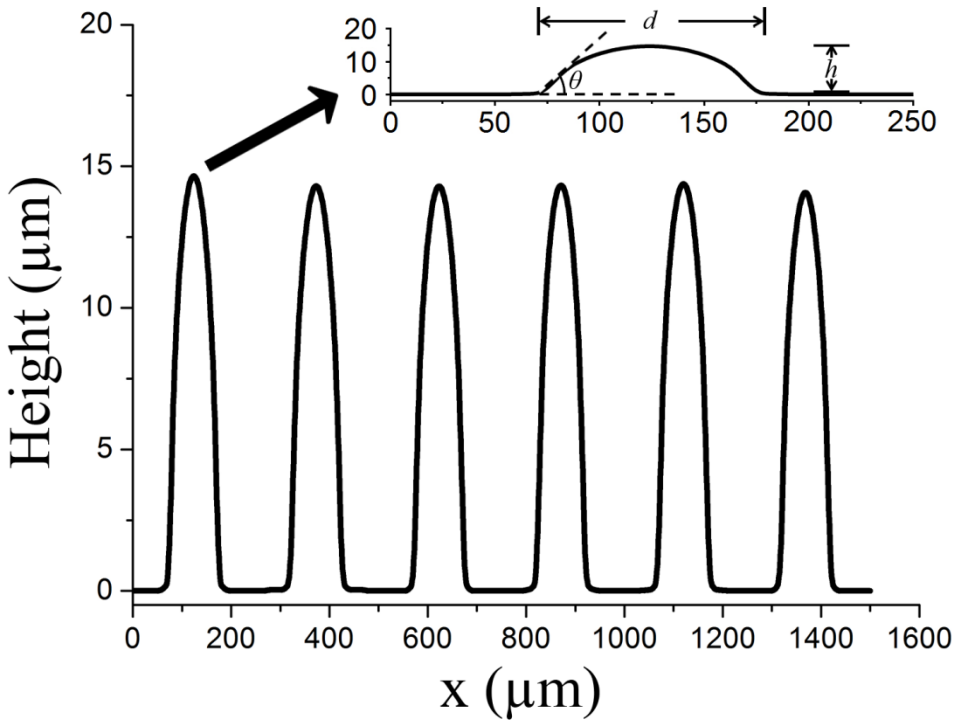

Figure 34 The profilometer measurement of randomly selected SU-8 microlenses, fabricated through vapor-induced, room temperature dewetting, with an initial film thickness of ~20 μm. The inset, showing the profile of the leftmost microlens, illustrates the geometrical relationship among the diameter (d), the height (h) and the contact angle (θ). For example, this microlens has a profile of d = 119.8 μm and h = 14.66 μm, resulting in θ = 27.5°, according to Eq. (14).

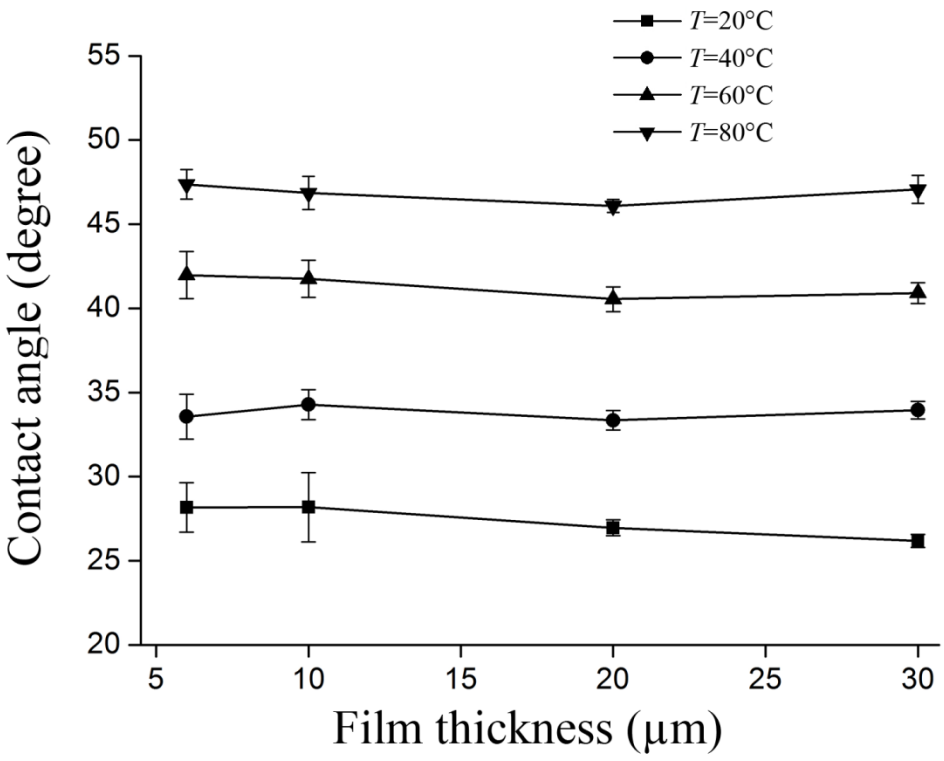

Figure 35 Contact angles of SU-8 microlenses fabricated through vapor-induced dewetting, as a function of the initial film thickness at various processing temperatures.

3.4.5 Optical Characterization

The imaging ability of as-fabricated microlens arrays was evaluated as the optical characterization. After the completion of dewetting, the self-organized SU-8 microlens arrays, along with the PDMS/Parylene-C substrates, were carefully peeled off and immediately transferred onto microscope slides. A printed photomask with a black letter “S” was used as the projection template to be imaged for the demonstration. Figure 36(a) schematically illustrates the testing setup, in which a microlens array, carried by a microscope slide, was positioned on the sample stage of an optical microscope and then illuminated from below through the projection template. The separation between the microlens array and the projection template, which is

commonly referred to as the object distance (u), is adjustable. Both the lens material (SU-8) and structural material (PDMS and Parylene-C) employed in our experiment have high optical transparency at visible wavelengths (400 nm to 800 nm) so as to reduce the light absorption by the polymers. The light passing through the template was imaged by the microlenses on the image plane and then projected through the objective lens of the microscope for observation. Figure 36(b) displays a projected image captured by an equipped CCD camera. An array of miniaturized letters "S" was observed over an SU-8 microlens array with an object distance of 11 mm. The images are inverted, real, and reduced in size with respect to the object (i.e., the projection template), which demonstrates the converging function of microlenses and their capability as optical elements.

The optical characteristics of the microlenses were further studied using the lens equation, which provides the quantitative relationship among the object distance (u), the image distance (v), and the focal length (f), as given below:

$$\frac{1}{u}+\frac{1}{v}=\frac{1}{f}. \tag{15}$$

The magnification factor (M), defined as the ratio of the size of the image (i) to the size of the object (o), can be expressed as follows:

$$M=\frac{i}{o}=\frac{v}{u}. \tag{16}$$

Substitution of Eq. (8) into Eq. (7) yields:

$$f=u\cdot\frac{M}{M+1}. \tag{17}$$

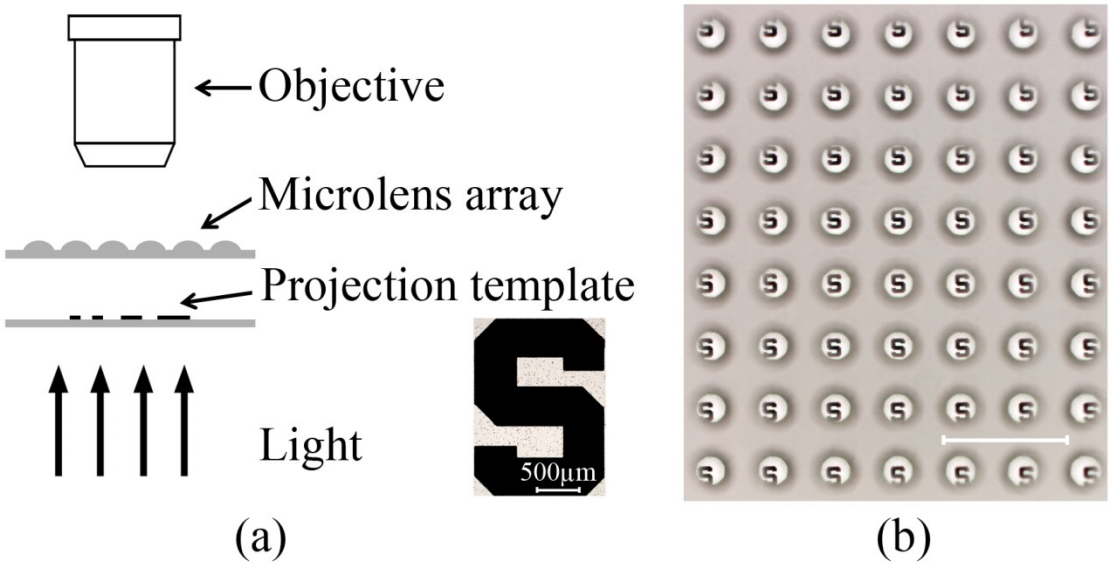

Figure 36 (a) Schematic illustration of the testing setup for the optical characterization of as-fabricated SU-8 microlens arrays. The inset shows an optical micrograph of a photomask with a black letter "S" which was used as the projection template to be imaged for the demonstration. (b) A projected image captured by a CCD camera equipped with the microscope. An array of miniaturized letters "S" was observed over an SU-8 microlens array with an object distance of 11 mm. This microlens array was fabricated through vapor-induced room temperature dewetting, with an initial film thickness of ~20 μm. The scale bars correspond to 500 μm.

Another important optical parameter, the numerical aperture (NA), is a function of the diameter of the base (d) and the focal length (f), expressed by:

$$\mathrm{NA} = \frac{d}{2f}. \tag{18}$$

Eqs. (17) and (18) were applied to evaluate the focal length and the numerical aperture of microlenses by measuring the object distance and the magnification factor. For convenience, a

calibration slide with 100 μm divisions was used for the observation in this experiment. At least ten microlenses randomly selected from each array were measured and the average was taken. Table II summarizes the measured geometrical and optical properties of SU-8 microlenses with typical curvatures, which were fabricated through vapor-induced dewetting at various processing temperatures. The focal length decreased from 359.4 μm to 219.2 μm and the numerical aperture increased from 0.166 to 0.273 with an increased contact angle from 27.0 ° to 46.1 °.

TABLE II

Geometrical and optical properties of SU-8 microlenses with typical curvatures

t (μm)	T (°C)	d (μm)	h (μm)	θ (°)	f (μm)	NA
20	20	119.1±1.8	14.3±0.2	27.0±0.5	359.4±7.3	0.166±0.002
20	40	119.0±0.2	17.8±0.3	33.3±0.6	281.3±9.1	0.212±0.005
20	60	119.4±1.2	22.0±0.3	40.5±0.7	260.8±7.0	0.228±0.003
20	80	119.6±1.2	25.4±0.3	46.1±0.4	219.2±6.6	0.273±0.002

t - approximate initial film thickness; T - processing temperature; d - diameter of the base;
h - height of the microlens; θ - contact angle; f - focal length; NA - numerical aperture.

3.4.6 Influence of Dimension

In order to study the influence of dimension on the curvatute of dewetted microlenses, we prepared a photomask with circular patterns of various diameters. After the dewetting process, the profile of microlenses was measured by a profilometer and shown in Figure 37. They exhibit an approximately constant CA of ~28 ° on the O_2-plasma-treated hydrophilic areas with various diameters, suggesting that the dimension of microlens can be easily controlled by the design of photomask without altering the lens curvature.

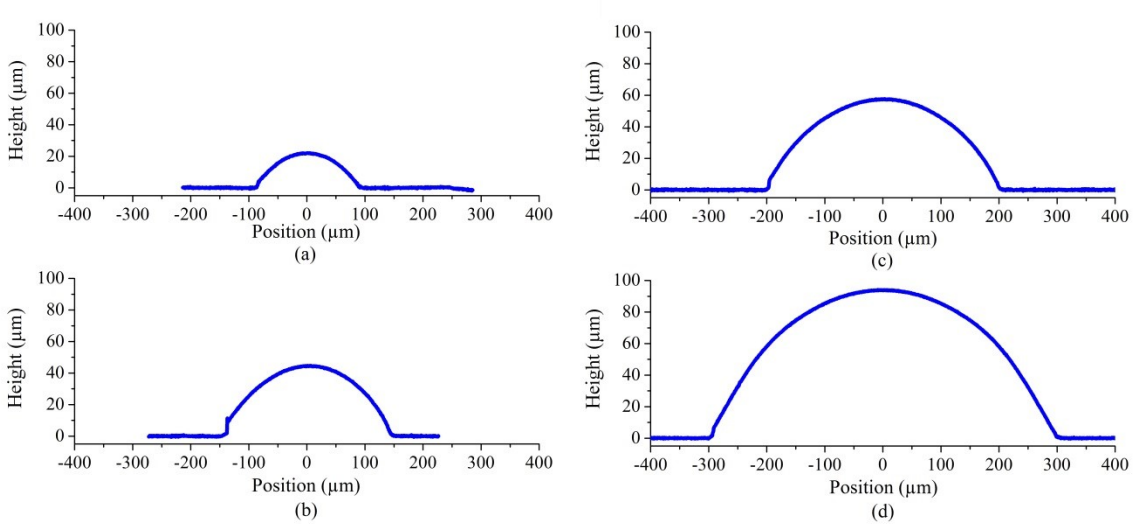

Figure 37 The profile of SU-8 μ-lenses with diameters of (a) 200 μm, (b) 300 μm, (c) 400 μm, and (d) 600 μm, which were fabricated through vapor-induced, room temperture dewetting on a chemically patterned PDMS substrates.

3.5 Discussion

One of the advantages in our experiment is the activation of dewetting at room temperature, which can be attributed to the exposure to the solvent vapor. For comparison, we have also investigated the dewetting process without solvent vapor exposure on chemically patterned PDMS substrates that were prepared in exactly the same way as described previously. In this case, no dewetting occurred at room temperature even after two months. The experimental setup illustrated in Figure 31, but without the presence of the solvent, was employed to find out the approximate dewetting temperature. The temperature of the hot plate was controlled such that it started from 20 °C with an increment of 5 °C per hour, until the occurrence of dewetting. The experiment showed that the rupture started to appear at 50, 55, 55, and 60 °C on SU-8 thin films with initial thicknesses of approximately 6, 10, 20, and 30 μm, respectively. In sharp contrast, by

exposure to the solvent vapor, dewetting can be rapidly triggered at room temperature on all the samples with various initial film thicknesses. Such a big difference can be primarily attributed to the activation of glass transition of SU-8 at room temperature owing to the presence of the solvent vapor [82]. The evaporated gas molecules of cyclopentanone can be absorbed into the SU-8 layer and thus the film viscosity is lowered. Such adsorption also weakens the interaction between the SU-8 film and the PDMS substrate. As a result, SU-8 polymer chains obtain enough mobility to be able to slide on the substrate even at room temperature.

The achievement of self-organization of dewetted microlenses has proved that the heterogeneity in surface chemistry could act as an ideal template to control the dewetting dynamics. In our experiment, the three-phase contact line displays an anisotropic receding speed once on contact with a hydrophilic spot. In fact, unlike the super-hydrophobic surface, the super-hydrophilic PDMS area has a higher surface energy, giving rise to a negative value of the effective Hamaker constant [83]. Therefore, the van der Waals force tends to stabilize the surface, which means that, theoretically, the SU-8 thin film does not dewet on the super-hydrophilic PDMS substrate. This is in accordance with our observation in which the SU-8 polymer liquid adhered onto the hydrophilic PDMS surface and was prevented from removal by dewetting. As a consequence, the contact line was pinned at the hydrophobic-hydrophilic boundary but still receded across the hydrophobic domain. This mechanism of pattern-directed dewetting is analogous to that observed on topologically heterogeneous substrates [68], except that it derives from the disjoining pressure due to the wettability contrast rather than from the capillary pressure due to the local curvature. As the contact line shifted along the hydrophobic-hydrophilic boundary, the distortion caused a neck to be generated on the side away from the wetting spot. The increased azimuthal curvature at the neck enhanced the pressure locally, drove

the flow away and eventually led to a pinch-off, which belongs to the breakup mechanism of end-pitching [84]. With continuous recession of the contact line and the repetitive occurrence of end-pitching, the morphology of the microlens array has been successfully generated. The conclusion can be drawn that the heterogeneity in surface wettability can effectively guide thin film instabilities and provide control on the dewetted morphology.

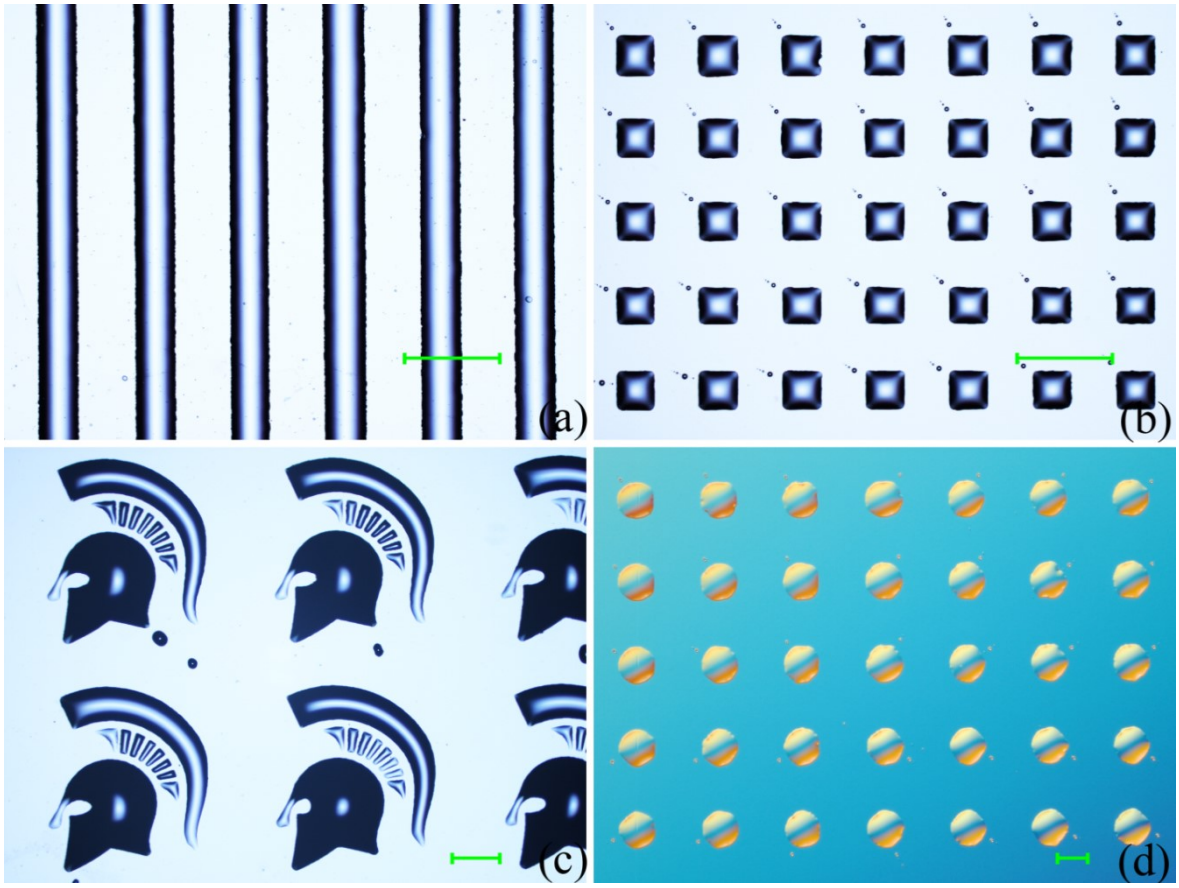

Figure 38 (a)-(c) Optical micrographs of periodic SU-8 micro-patterns on PDMS substrates: (a) parallel strips, (b) an array of squares, and (c) an array of "Spartans" logos. (d) Optical micrograph of an SU-8 microlens array on a Parylene-C substrate. All the micro-structures in this figure were generated through vapor-induced, room temperature dewetting on chemically patterned substrates. The scale bars correspond to 100 μm.

In addition, we have also demonstrated that the templated dewetting on chemically patterned substrates is widely applicable to creating ordered and even complex micro-structures with various geometries. Figure 38(a)-(c) presents optical micrographs of a series of periodic SU-8 patterns that were prepared by our method, including parallel strips, an array of squares, and an array of "Spartans" logos on PDMS substrates. Furthermore, our dewetting process is applicable to different substrates. As an example, SU-8 microlens arrays were successfully generated on a ~2-μm-thick chemically patterned Parylene-C thin film through vapor-induced, room temperature dewetting, as shown in Figure 38(d). These microlenses show an average contact angle of 2.8 ± 0.4°, which is different from the contact angles of microlenses dewetted on PDMS substrates, suggesting the influence of surface tension and surface chemistry on the dewetting process.

3.6 Summary

In this chapter, we have demonstrated the efficacy of a vapor-induced dewetting method for the fabrication of microlens arrays on chemically patterned substrates. The surface heterogeneity, arising from the selective SF_6 and O_2 plasma treatments, acted as an ideal template to control the dewetting dynamics. The dewetted SU-8 droplets were spontaneously organized on O_2-plasma-treated hydrophilic spots to form well-aligned microlens arrays. The exposure to the solvent vapor allows for the initialization of dewetting at room temperature. The microlens curvature is strongly correlated to the processing temperature, but nearly independent of the initial film thickness and the microlens dimension. The imaging ability of the as-fabricated microlenses has shown that a range of optical properties can be obtained. Our method provides a versatile and effective route for engineering periodic micro-scale structures over large areas for applications in

micro-electronic and optical devices.

In the following chapters, we will focus on the fabrication and integration of the proposed micro-lens-coupled LED stimulators. The technology of vapor-induced dewetting, discussed in this chapter, will be applied as an important approach to fabricate both microlenses and reflectors.

CHAPTER 4 Micro-Lens-Coupled LED Stimulators

Application of optogenetics in neuroscience studies has inspired the development of light sources and instruments for light delivery. Optical stimulation of neural cells is most commonly accomplished by illuminating target neurons with laser, laser diode, or light-emitting-diode (LED) coupled optical fibers [9, 18, 85]. Although such instruments can provide strong illumination, their spatial resolution is limited, and the tethered optical fibers greatly restrict the natural behavior of freely moving subjects. The employment of micro-LEDs (μ-LEDs) offers a great option as the light source for optogenetics [12]. They are power-efficient, low-cost, and suitable for integration with wireless electronics [13]. Furthermore, arrays of individually addressable μ-LEDs have been developed to accomplish multisite in-vivo stimulation [14, 15, 86]. However, a critical challenge of using LEDs as the light source for optogenetics is their intrinsically low out-coupling efficiency and wide irradiation angles due to the Lambertian emission pattern, which results in a big loss of the radiation. Consequently, LEDs must be driven with high power in order to reach the required light intensity of 1 mW/mm^2 and 7 mW/mm^2 for effective activation of excitatory and inhibitory opsins at the target site, respectively [87]. This, however, is not suitable for wireless operation, and could induce potential thermal interference or damage to tissues due to Joule heating effect. Therefore, an extra optical component that can help collimate the LED light is particularly desired, offering capabilities of deep layer stimulation with reduced input voltage and power consumption. To date, little study has been reported on such collimated LED stimulators for optogenetic applications [17, 21].

To address these needs, we propose an implantable, micro-lens-coupled LED neural stimulator to be applied as the light source for deep layer neural stimulation. A reflector and a

microlens were coupled with the μ-LED chip for light collection and collimation, giving rise to a significantly improved light irradiance at near-normal irradiation angles. The 1st generation of prototypes has been fabricated and integrated.

4.1 Design Concept

The proposed micro-lens-coupled LED stimulator comprises three main elements: a μ-LED chip, a microlens, and a reflector, as shown in Figure 39. The μ-LED is placed on a thin Parylene-C substrate, which is biocompatible, flexible, and optically transparent. A PDMS cover is employed to house the μ-LED, and also serves as the substrate in fabrication of SU-8 microlens. The μ-LED is sandwiched between the microlens and the reflector with center alignment through bonding. Since the unpackaged μ-LED chip used in our experiments radiates light in all directions, the backside reflector is applied to redirect and collect the downward-emitting lights, while the microlens is placed on the frontside of the μ-LED enabling collimation of lights. Surface mounted μ-LED chips (Cree® TR2227TM, 220 μm × 270 μm × 50 μm) with a peak wavelength of 460 nm are used as the light source.

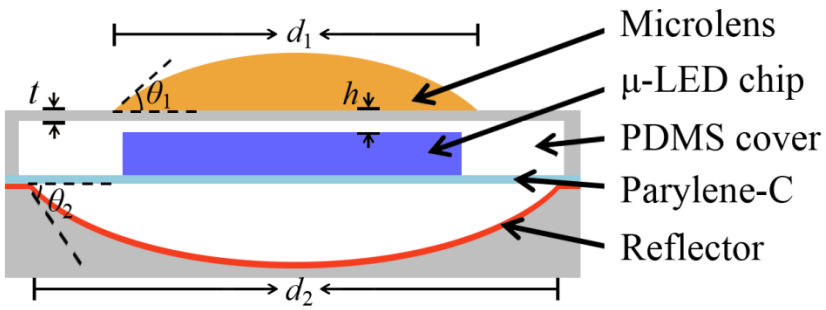

Figure 39 Structure of micro-lens-coupled LED simulator, which comprises a μ-LED chip, a frontside microlens, and a backside reflector.

4.2 Fabrication of Device Prototypes

For the proof-of-concept, the 1st generation of prototypes of micro-lens-coupled LED stimulators have been designed and constructed. The fabrication and integration processes are schematically illustrated in Figure 40. SU-8 pillars (MicroChem Corp.), with dimensions of 320 μm × 370 μm × 80 μm, were first patterned on silicon substrates through photolithography, followed by spin-coating a layer of 100 μm-thick PDMS mixture (Dow Corning Sylgard® 184, 10 : 1 by weight). Surface plasma treatment (PX-250, March Instruments) and vapor-induced dewetting (VID) were subsequently applied to fabricate self-organized SU-8 microlenses with a diameter of 220 μm and a height of 25 μm at designated spots on the PDMS surface. Experimental details of the VID process for microlens fabrication have been previously discussed in Chapter 3. After the microlenses were formed, the PDMS cover was cut and peeled off for the preparation of assembly. The cavities under the cover for housing μ-LEDs were replicated from the SU-8 pillars and matched the dimensions of the μ-LEDs.

The VID process was also employed for fabricating backside reflectors, as shown in Figure 40(b). SU-8 microlenses with a diameter of 600 μm and a height of 70 μm were obtained and served as the master for PDMS micromolding. A 300 nm-thick aluminum film was subsequently deposited through thermal evaporation (Edwards Auto 306 Evaporator) on the surface of embossed PDMS to form a reflecting layer.

Surface mounted μ-LED chips (Cree® TR2227TM, 220 μm × 270 μm × 50 μm) with a peak wavelength of 460 nm were used as the light source. They were soldered on flexible, micro-patterned circuit on a Parylene-C substrate. As shown in Figure 40(c), prototypes of micro-lens-coupled stimulators were successfully integrated by centrally aligning each component under a

stereo microscope and bonding with a polymer adhesive. Figure 41 presents an image of an integrated device, as well as representative SEM images of a single microlens and a microlens array fabricated by VID process.

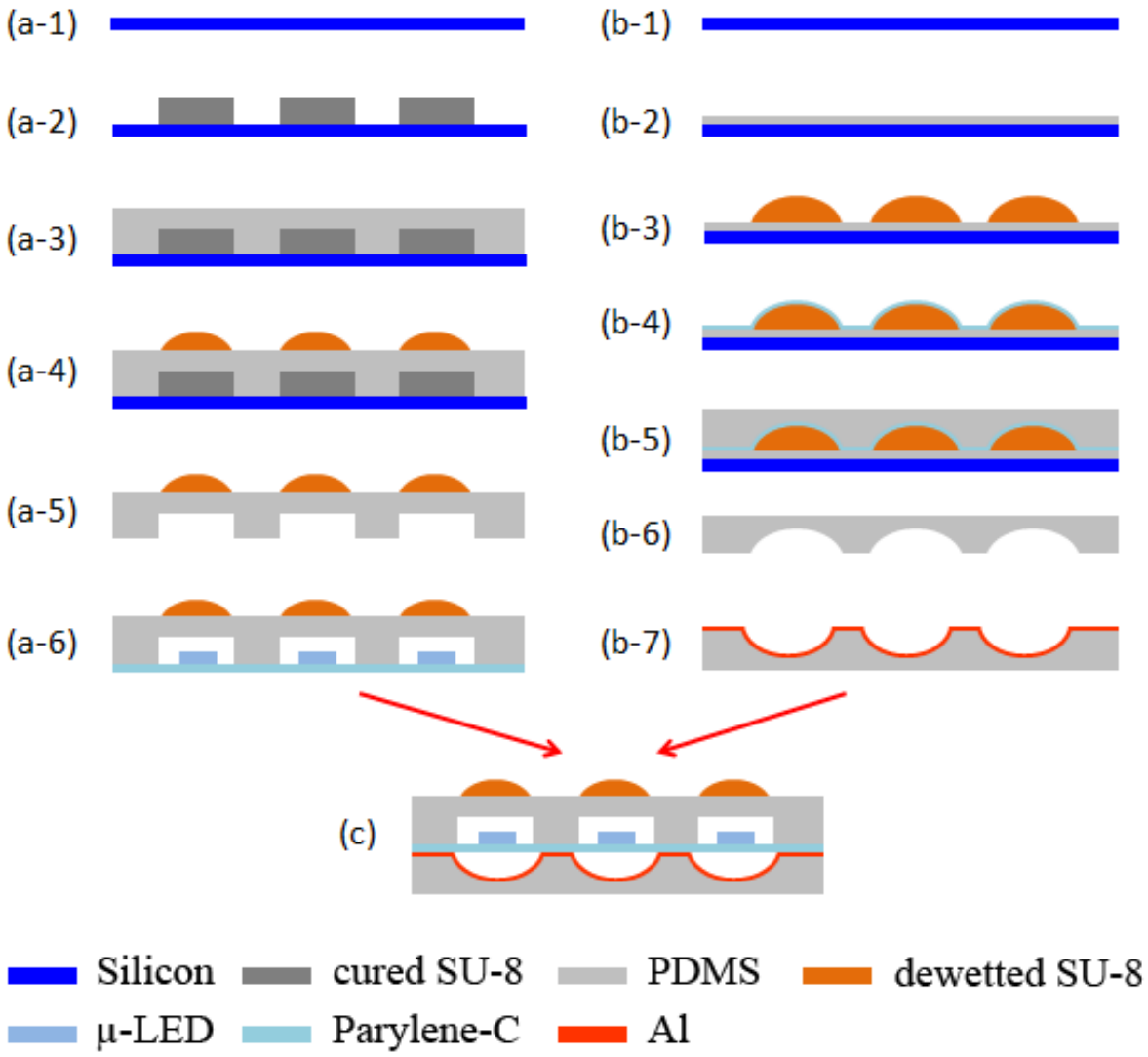

Figure 40 Schematic illustration of fabrication and integration processes of the micro-lens-coupled LED simulator: (a) microlens fabrication, (b) reflector fabrication, and (c) device integration.

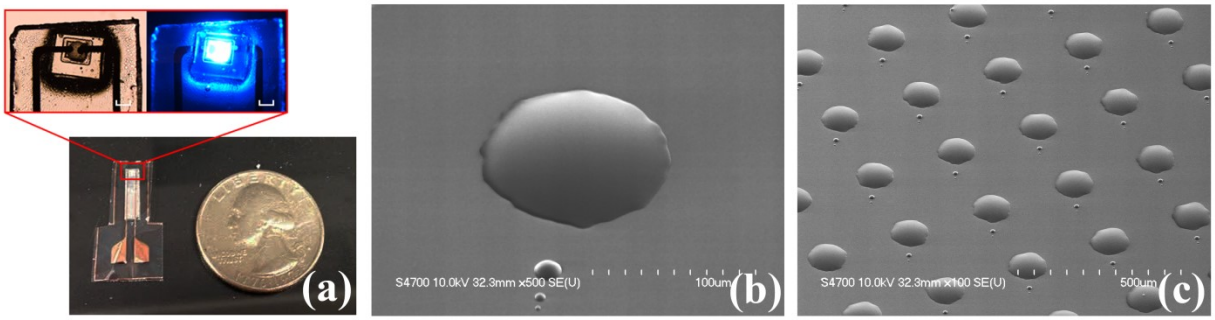

Figure 41 (a) Image of an integrated micro-lens-coupled LED stimulator. The inset shows micrographs of the device without and with light illumination. The scale bars in the inset correspond to 200 μm. (b) SEM image of a fabricated microlens which was made by VID process. (c) SEM image of a microlens array.

4.3 Optical Measurement

4.3.1 Measurement in Air

The optical performance of device prototypes was first characterized in air using a photodetector (Model 815 Series, Newport, Inc), which has an approximate sensing area of 100 mm^2 to measure the incident light intensity. The photodetector was positioned on top of the measured device with a fixed distance of 9.3 mm between the μ-LED top surface and the optical sensor. The light intensity radiated from ten prototypes under a driving voltage of 2.7 V was measured. At least five measurements were carried out for each prototype and the average was taken. For comparison, we also measured the light intensity of the corresponding bare μ-LED chips before the device integration process. The percentage of improvement in light intensity was calculated, as shown in Figure 42. A significant increase of ~67% was achieved by the micro-lens-coupled LED stimulators in average, compared to the bare μ-LEDs.

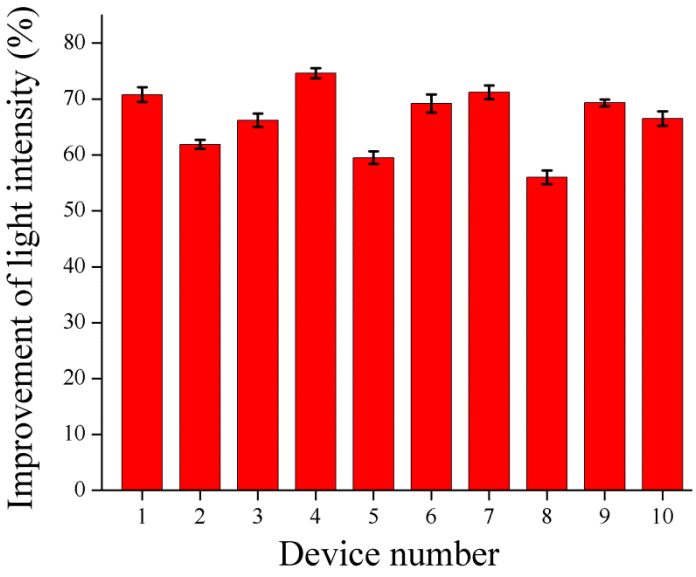

Figure 42 The improvement of light intensity radiated by ten micro-lens-coupled LED stimulators under a driving voltage of 2.7 V. The reference intensity for each device was measured on the corresponding bare μ-LED chips. The measurement was carried out using a photodetector with its sensor part located at 9.3 mm away from the LED top surface.

4.3.2 Measurement in Tissue-Mimicking Gelatin

In order to validate the functionality of prototypes in optogenetic experiments, a tissue-mimicking phantom was constructed using gelatin. The powder of gelatin was mixed with water at a ratio of 1:4 in weight and stirred for 2 min. It was then filled in the gap between the measured prototype and the photodetector, and kept until turning firm. Due to the equipment limitation of the photodetector, the measured device could not approach to the sensor part closely enough to attain a comparable distance as in optogenetic experiments, which is typically on the order of several hundred micrometers. Therefore, the relative light intensity was calculated to characterize the optical performance. Since the μ-LED chip of the same type has been found capable of activating neural activity in the brain of rats with an applied driving voltage above 2.7

V in our previous optogenetic experiment, the light intensity for the bare μ-LED under 2.7 V was used as the reference intensity. Figure 43 plots the relative light intensity of a prototype and the corresponding bare μ-LED under different driving voltages. A constantly ~78% improvement was obtained in gelatin under various voltages of 2.4-3.4 V for the fabricated prototype, implying that the proposed micro-lens-coupled LED stimulator is capable of providing much stronger illumination. In other words, it has the potential to enable optogenetic neurostimulation with a lower driving voltage on μ-LEDs, and thus prevent excessive heat production and damage to tissue.

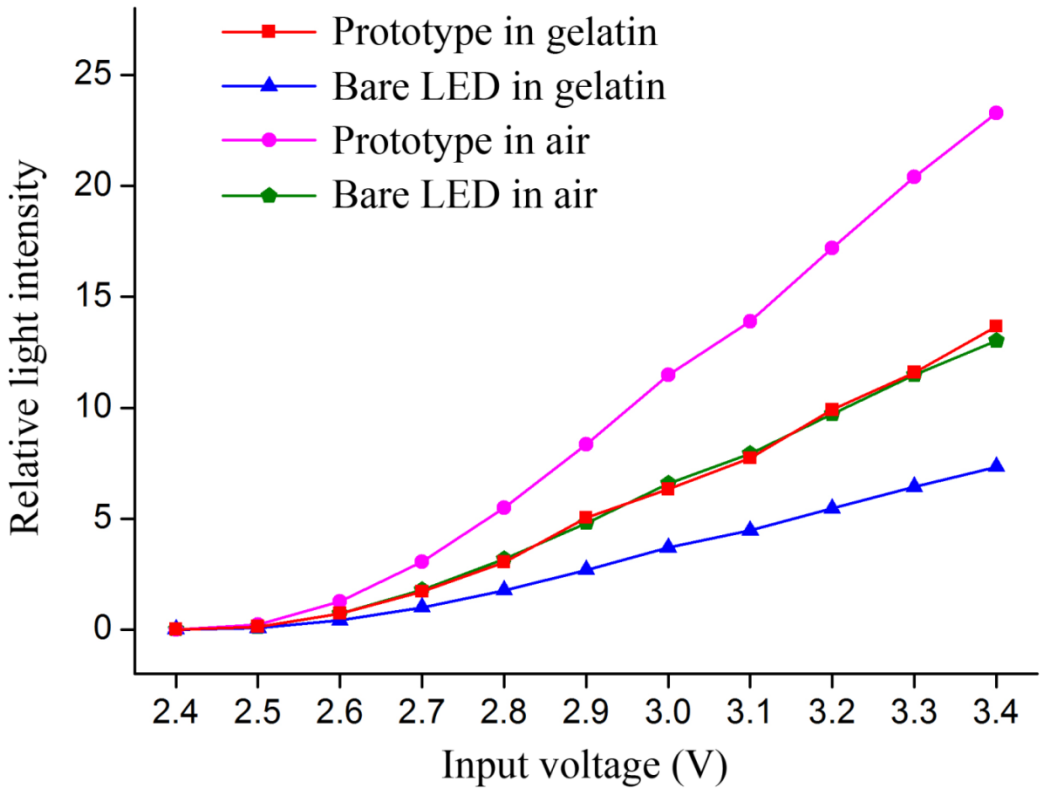

Figure 43 Relative light intensity of a device prototype of micro-lens-coupled LED stimulator and the corresponding bare μ-LED under different driving voltages, which was measured both in air and in phantom tissue.

CHAPTER 5 Optimization of Micro-Lens-Coupled LED Stimulators

Optical simulation and optimization was performed in Tracepro (Lambda Research Corporation, Littleton, MA) by tracing light rays using the Monte Carlo method to study the properties of the micro-lens-coupled LED stimulator. A typical structural model including all the elements is presented in Figure 44. The surface source property was imported from the irradiation distribution on μ-LED data sheet. Except when specifically mentioned, a light radiative flux of 1 W with a wavelength of 460 nm was set on both the top and the bottom LED surfaces in order to simulate the double-sided illumination. The geometry for each element was drawn based on the design and the optimization of their structures will be discussed later. Candela distribution, which shows the relationship between light radiant intensity ($I_{e,\Omega}$) and irradiation angles, is used to characterize the emission property of the light source. The light radiant intensity is measured in watts per steradian (W/sr). The irradiation angle is defined as the angle with respect to the normal direction to the LED top surface. Especially, the light radiant intensity at 0° on the candela distribution ($I_{e,\Omega,NORMAL}$) is employed to approximately represent the collimation ability of the light. For a bare μ-LED chip, $I_{e,\Omega,NORMAL}$ is 0.29 W/sr.

5.1 Optimization of Microlens Structure

Several parameters have been considered for microlens optimization, including its base diameter (d_1), its inclined angle (θ_1), its distance away from the LED top surface (h), and the thickness of the PDMS layer (t), as shown in Figure 39. It is noteworthy that the PDMS cover is a necessary element in our design because of the following two reasons. First, a fabrication technique called vapor-induced dewetting (VID) [88] is employed to produce SU-8 microlenses directly on the plasma-treated PDMS surface. During the dewetting process, the surface

chemistry of PDMS plays a crucial role in determining the range of the inclined angle of microlenses. Second, the lens effect is strongly influenced by the distance between the lens and the μ-LED (h), which can be tuned using PDMS micromolding to achieve the most desired value. On the other hand, in order to minimize the scattering effect while light propagates through PDMS, the thickness of the PDMS cover (t) was kept as small as 10 μm.

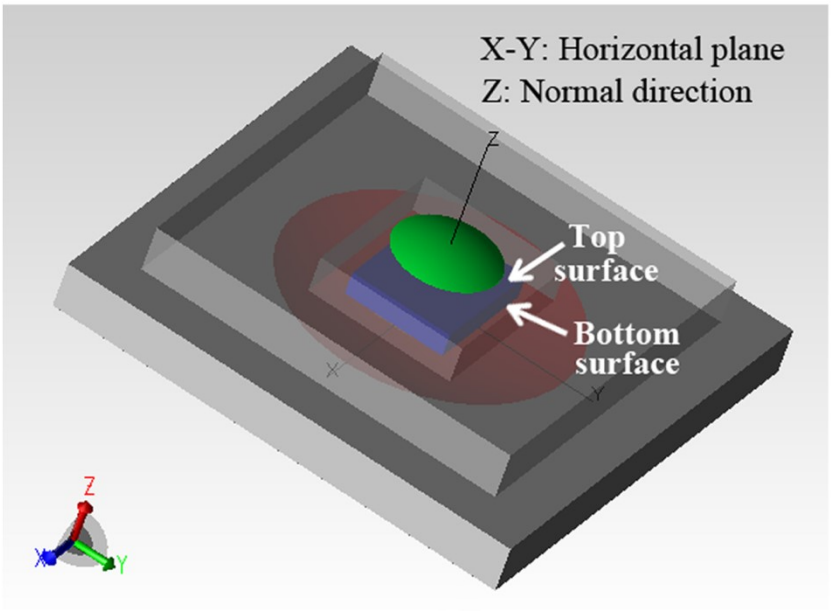

Figure 44 Structural model of the micro-lens-coupled LED stimulator in the simulation.

Taking the compactness of devices into consideration, d_1 and h were limited to not exceed 600 μm and 100 μm, respectively. The influence of θ_1 on the collimation was first considered. Figure 45 shows representative curves of $I_{e,\Omega,NORMAL}$ as a function of h for μ-LED-coupled microlenses with a fixed d_1 of 500 μm but varied θ_1 of 30°, 45° and 60°. It can be concluded that a microlens with a larger inclined angle leads to a stronger light radiant intensity in the normal direction. Such a trend was also observed in our optical simulation for microlenses with varied diameters of 400 μm, 450 μm, 550 μm and 600 μm. Since our VID process can fabricate

microlenses with inclined angles between ~27° to ~47° [88], θ_1 = 45° is used in the following optimization studies. For microlenses with larger inclined angles, other microfabrication approaches, such as grayscale photolithography [57] and ink-jet printing [60], can be employed.

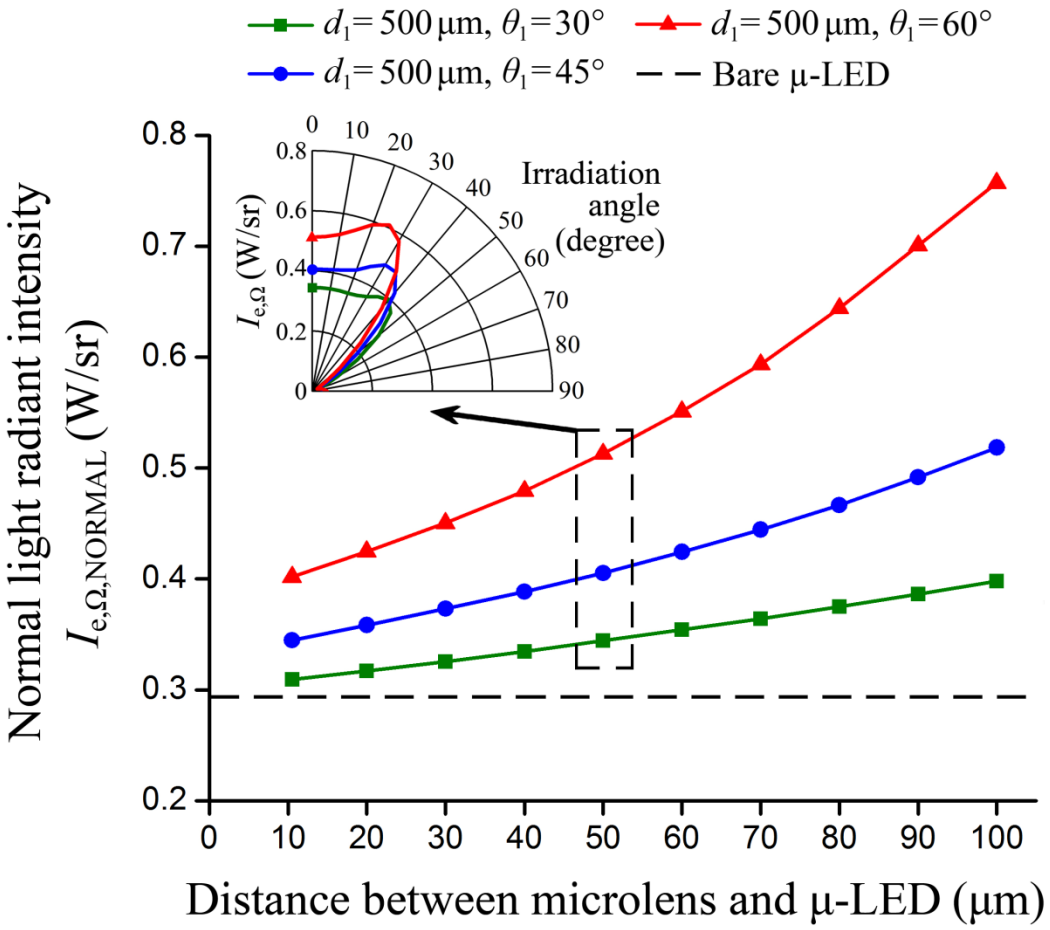

Figure 45 Simulated normal light radiant intensity ($I_{e,\Omega,NORMAL}$) for µ-LED-coupled microlenses with a fixed base diameter (d_1) of 500 µm but varied inclined angles (θ_1) of 30°, 45° and 60°, as a function of the distance between the µ-LED and the microlens (h). The inset shows candela distribution of µ-LED-coupled microlenses that are placed at h = 50 µm. The light radiative flux from each side of the µ-LED was set to 1 W. For comparison, the black dash line shows the value of $I_{e,\Omega,NORMAL}$ for the bare µ-LED.

Figure 46 plots $I_{e,\Omega,NORMAL}$ as a function of h for μ-LED-coupled microlenses with the optimized θ_1 of 45° and varied d_1 ranging from 350 μm to 600 μm. As can be seen, the collimation capability of the microlens can be improved as h appropriately increases. Especially, an optimal $I_{e,\Omega,NORMAL}$ of 0.54 W/sr was achieved from a microlens with $d_1 = 450$ μm and $\theta_1 = 45°$ while $h = 100$ μm.

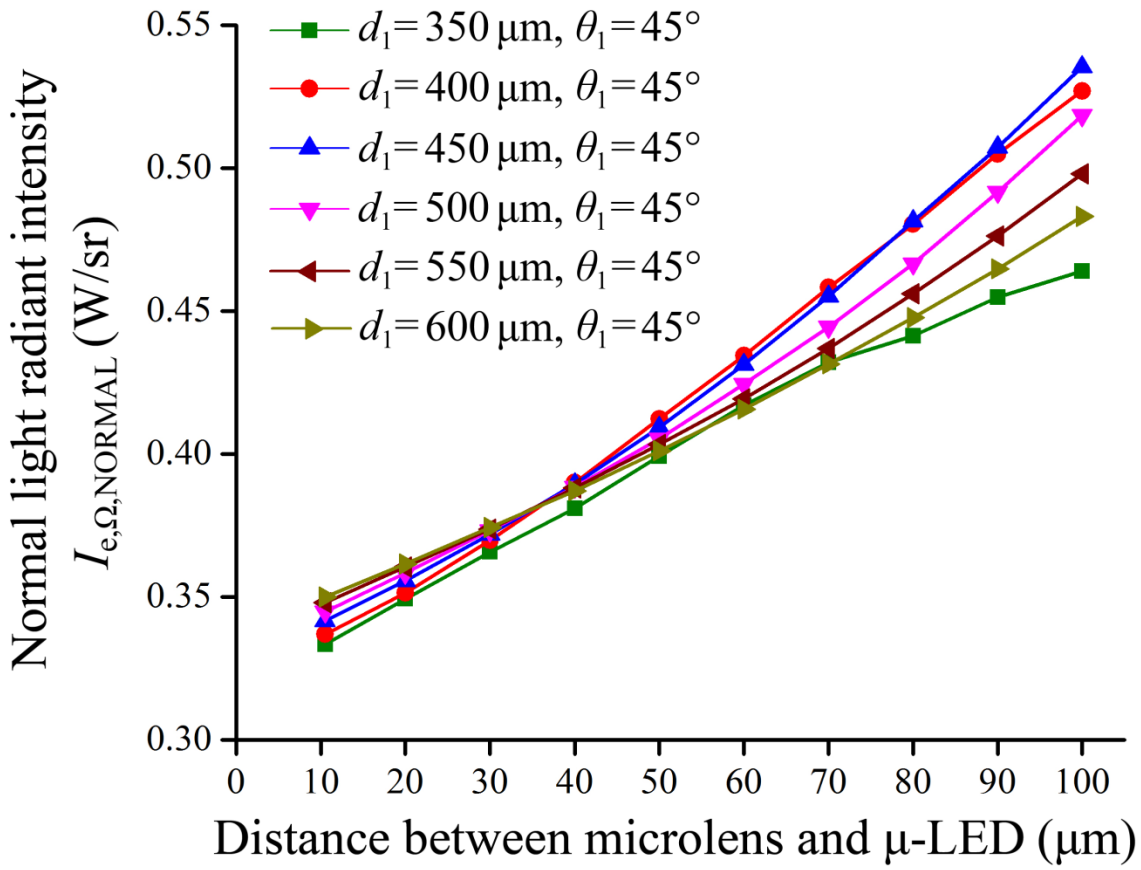

Figure 46 Simulated normal light radiant intensity ($I_{e,\Omega,NORMAL}$) for μ-LED-coupled microlenses with a fixed inclined angle (θ_1) of 45° but varied base diameters (d_1) ranging from 350 μm to 600 μm, as a function of the distance between the μ-LED and the microlens (h). The light radiative flux from each side of the μ-LED was set to 1 W.

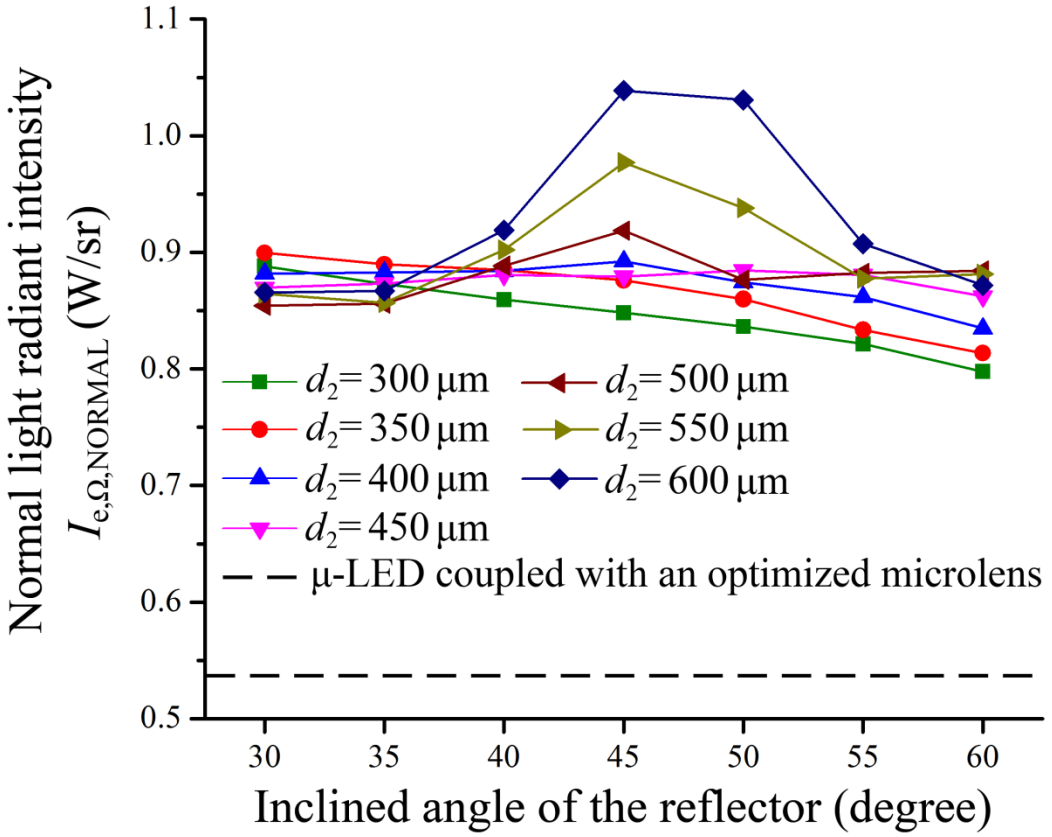

Figure 47 Simulated normal light radiant intensity ($I_{e,\Omega,NORMAL}$) for μ-LEDs coupled with an optimized microlens (d_1 = 450 μm, θ_1 = 45°, t = 100 μm) and different reflectors with varied diameters (d_2) and inclined angles (θ_2). The light radiative flux from each side of the μ-LED was set to 1 W. For comparison, the black dash line shows the value of $I_{e,\Omega,NORMAL}$ for the device without a reflector.

5.2 Optimization of Reflector Structure

In this part, a reflector was further integrated on the backside of the μ-LED chip, which had been coupled with an optimized microlens. 90% reflectance was applied to simulate the high reflectivity of the surface. In the simulation, the diameter (d_2) and the inclined angle (θ_2) of the

reflector varied from 300 μm to 600 μm and from 30° to 60°, respectively. Simulation result of $I_{e,\Omega,NORMAL}$ in relation to d_2 and θ_2 is presented in Figure 47, which shows great enhancement on $I_{e,\Omega,NORMAL}$ compared to the device without a reflector. It can be attributed to the effective collection of the downward-emitting LED light. The maximum of $I_{e,\Omega,NORMAL}$ (1.04 W/sr) appears as $d_2 = 600$ μm and $\theta_2 = 45°$, which were chosen as the dimensions for the optimized reflector.

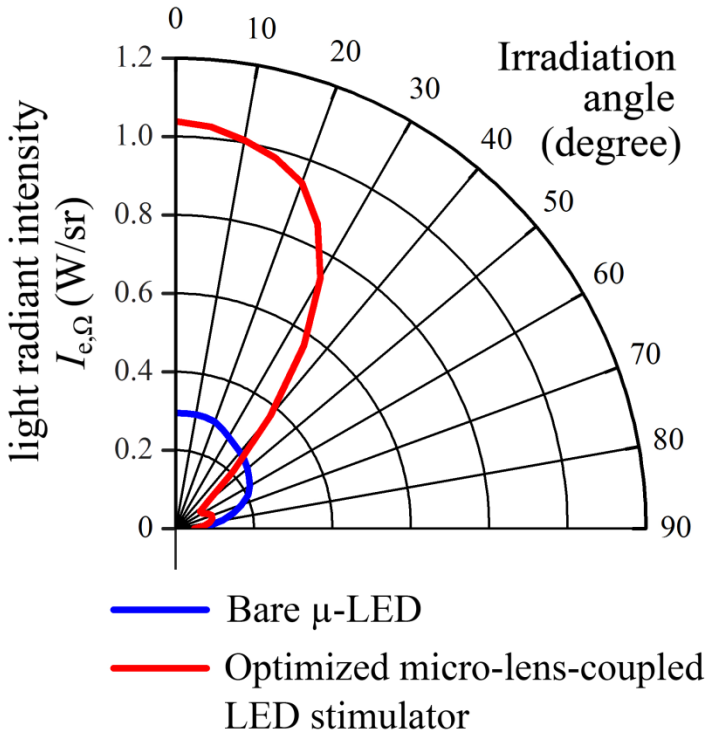

Figure 48 Simulated candela distribution of the bare μ-LED and the optimized micro-lens-coupled LED stimulator. The light radiative flux from each side of the μ-LED was set to 1 W.

5.3 Performance of Optimized Structure

So far, we have investigated the structure of both microlens and reflector, and their optimized dimensions have been found. To avoid confusion, in this paper, the term "micro-lens-coupled LED stimulator" is uniquely used to describe the μ-LED chip coupled with both

microlens and reflector. Figure 48 plots the simulated polar candela distribution of the optimized micro-lens-coupled LED stimulator, as well as the distribution of the bare μ-LED for comparison. It clearly shows that the optimized micro-lens-coupled LED stimulator can effectively enhance the light irradiance at small irradiation angles (< 30°). Especially, $I_{e,\Omega,NORMAL}$ increased from 0.29 W/sr to 1.04 W/sr when the light radiative flux was set to 1 W on each side of the μ-LED.

In order to mimic the application of the device in a biological environment, the penetration of light in the medium of tissue for the micro-lens-coupled LED stimulator was also simulated. At this time, the measured light radiative flux of μ-LEDs under an applied voltage of 2.9 V, which results in 2.06 mW on each side, was used to investigate the effective region in which optogenetic opsins can be stimulated. This voltage (2.9 V) was selected because it can provide strong illumination while avoiding overheating of the brain tissue as demonstrated previously in [89]. An absorption coefficient (μ_a) of 0.5 cm^{-1} and a reduced scattering coefficient (μ_s') of 15 cm^{-1} were employed as the transmitting property of the light in the rat cortex at a wavelength of 460 nm [90]. The contour lines at 1 mW/mm^2, which is the typical threshold of light intensity for activating excitatory opsins [87], are plotted in Figure 49. Since the light source is typically placed in contact with the surface of the brain tissue during optogenetic experiments, a term of effective penetration depth (d_{eff}) is defined as how far the light propagates through the illuminated medium. For the lens-coupled LED stimulator, it is the distance between the target position and the summit of the microlens, rather than the μ-LED top surface. As shown in Figure 49, the optimized micro-lens-coupled LED stimulator shows an evocable effective penetration depth of 800 μm, an increase of 26.0% compared to 635 μm for the bare μ-LED chip. The volume of stimulated tissues (with light intensity larger than 1 mW/mm^2) for the micro-lens-

coupled LED stimulator and the bare μ-LED is 0.328 mm^3 and 0.193 mm^3, respectively, corresponding to an increase of 70.4%.

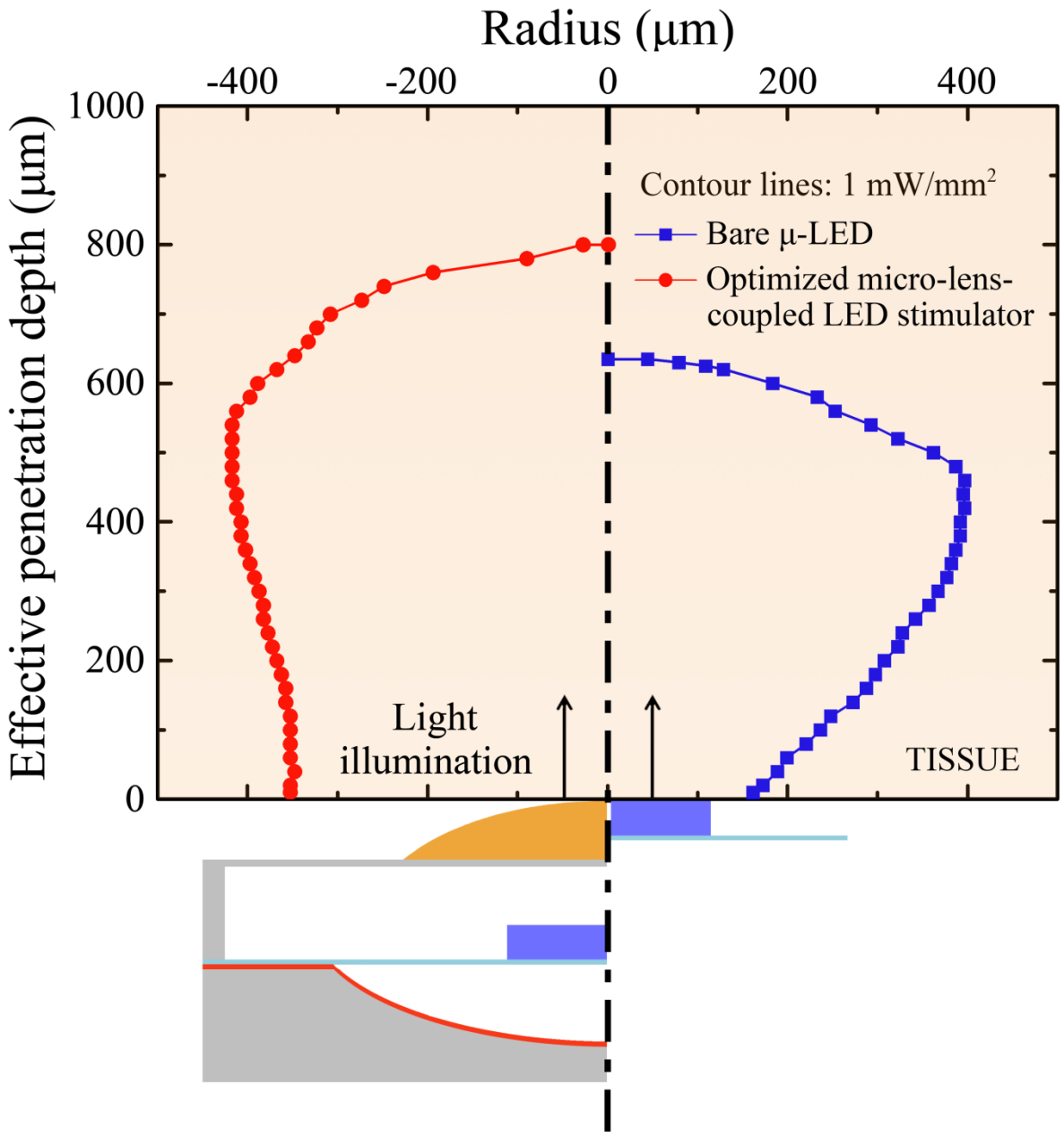

Figure 49 Simulated contour lines at 1 mW/mm^2 in rat cortex for the optimized micro-lens-coupled LED stimulator (red) and the bare μ-LED (blue). The light radiative flux from each side of the μ-LED was set to 2.06 mW, which was measured under an applied voltage of 2.9 V.

5.4 Device Measurement

5.4.1 Profile

Based on the simulation result, prototypes of micro-lens-coupled LED stimulators with the optimized dimensions, i.e., d_1 = 450 µm, θ_1 = 45°, h = 100 µm, d_2 = 600 µm and θ_2 = 45°, have been fabricated and integrated. Figure 50 presents an optical image of an integrated device, as well as the profiles of as-fabricated microlenses and reflectors that were examined by a surface profile. The measurement was carried out on five integrated LED stimulators and the average was taken. The microlens shows a base diameter of 458.5 ± 2.3 µm and an inclined angle of 42.7 ± 1.1°, while the reflector has a diameter of 606.5 ± 3.0 µm and an angle of 41.6 ± 1.2°.

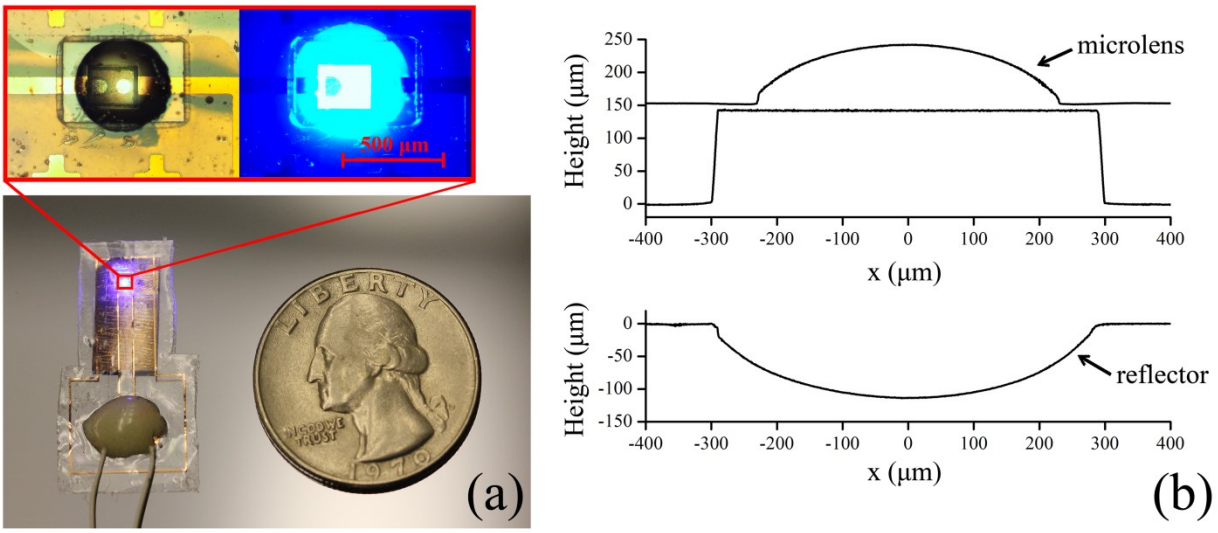

Figure 50 (a) Optical image of an integrated micro-lens-coupled stimulator with optimized dimensions. The inset shows micrographs of the device without (left) and with (right) light illumination. (b) Profilometer measurement of the microlens and the reflector of an integrated micro-lens-coupled LED stimulator, which shows a profile of d_1 = 461.2 µm, θ_1 = 42.4°, d_2 = 602.0 µm and θ_2 = 41.5°.

5.4.2 Measurement in Air

The optical performance of a fabricated device prototype of micro-lens-coupled LED stimulator was characterized in air using a photodetector (Model 815 Series, Newport, Inc), which has an approximate sensing area of 100 mm^2 to measure the incident light power. The photodetector was fixed on a 3D micropositioning stage to be able to adjust the distance between the detector and the device prototype (i.e., effective penetration depth, d_{eff}). The prototype was lit up with a fixed driving voltage of 2.9 V. The d_{eff} was gradually changed from 0 to 5,000 μm with every single step of 100 μm. Three times of measurements were carried out for the prototype before it was disassembled and the light power of the corresponding bare μ-LED was measured in the same method for another three times. The measurement result was averaged and plotted in Figure 51. For comparison, Figure 51 also presents the result of the simulation, in which an observation disk with a sensing area of 100 mm^2 was placed at varied depths to collect the incident light power. The applied LED source property (2.06 mW) was determined in such a way that the simulation and the measurement show an identical light power at $d_{eff} = 0$ for the bare μ-LED. The percentage of the improvement of light power for the measured prototype was calculated and also included in Figure 51.

As can be seen, the simulation and measurement results for the bare μ-LED are very consistent, as the corresponding two curves almost completely overlap. For the device prototype, the measurement result is averagely 11% lower than the simulation, which is possibly due to the low reflectance of the reflector, as some wrinkles were observed on the aluminum thin film during assembly. As d_{eff} increases from 0 to 5,000 μm, the fabricated micro-lens-coupled LED stimulator achieves an improvement of light power from 15% to 102%, compared to the bare μ-

LED. The improvement keeps increasing as the distance goes further, which is an evidence of the collimation effect resulted by the microlens. It implies that micro-lens-coupled LED stimulators could be more valuable in deep brain stimulation.

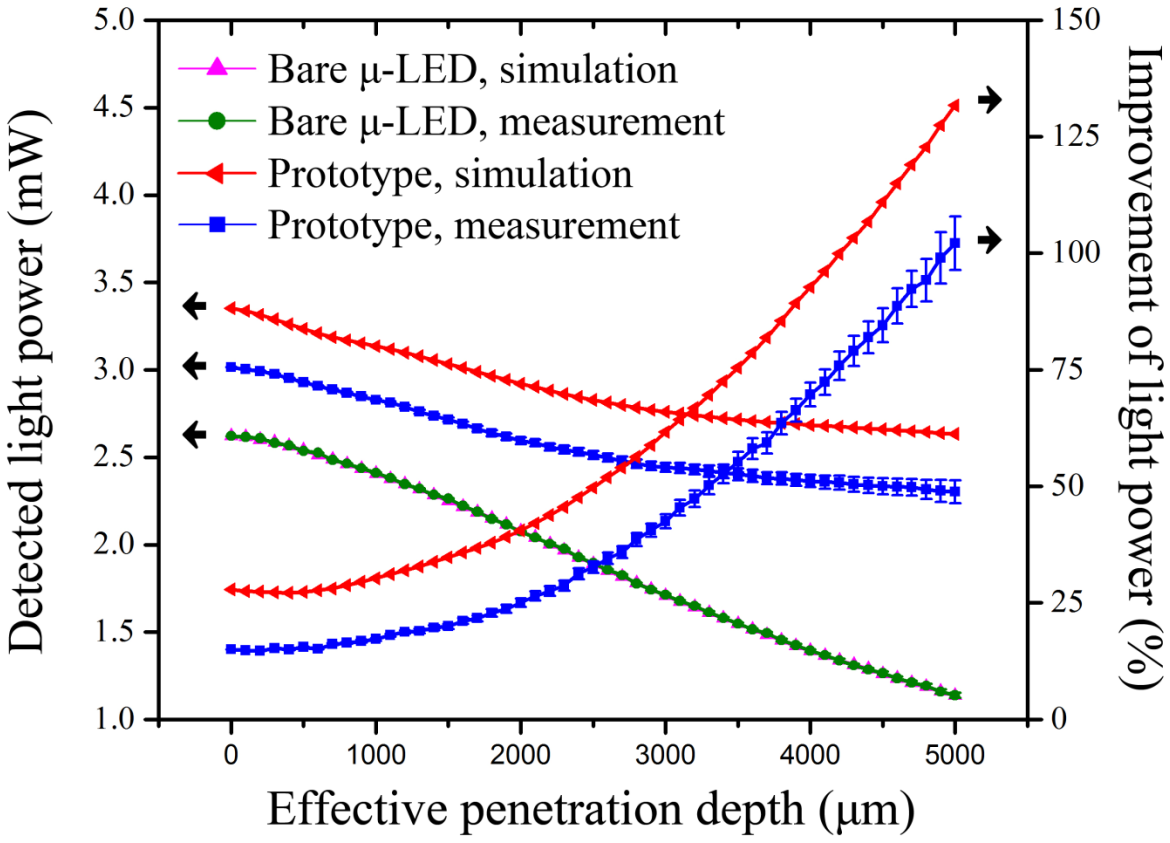

Figure 51 Detected light power of a device prototype of the optimized micro-lens-coupled LED stimulator and the corresponding μ-LED under an applied voltage of 2.9 V, as well as the improvement of the light power for the measured prototype, as a function of the effective penetration depth. The photodetector has a sensing area of ~100 mm^2. For comparison, the simulation result was also plotted.

5.4.3 Measurement through Tissue

In this measurement, the d_{eff} was fixed as far as 5,000 μm. An approximate 500-μm-thick rat cortical tissue slice was cut after an animal surgery and kept in saline. When applied, the tissue was taken out using a brush and placed directly on the top of the device. The light power was measured by the photodetector for one fabricated device prototype and the corresponding μ-LED, as shown in Figure 52. An average 99% and 103% improvement was obtained with and without the 500-μm-thick rat tissue under various voltages of 2.4-3.2 V for the measured prototype, respectively. The proposed micro-lens-coupled LED stimulator demonstrates a remarkable potential to enable optical neural stimulation with a lower driving voltage on μ-LEDs, and thus prevent excessive heat production and reduce the risk of tissue damage.

5.4.4 Soaking Test

Soaking test was initiated by immersing two device prototypes in saline (0.9 wt% sodium chloride) on a hot plate set at 40 °C for seven days, to evaluate the reliability of the lens-coupled LEDs. One device (A) was kept on by applying a continuing pulsed signal with a voltage of 2.7 V and a duty cycle of 50%, while the other one (B) was disconnected. After seven days, device A shows a decrease of 11.8% in the light power at d_{eff} = 0, while device B did not show any deterioration of optical throughput. Soaking test study is ongoing for the statistical analysis of device's long-term reliability and the in-depth understanding of potential failure mechanisms.

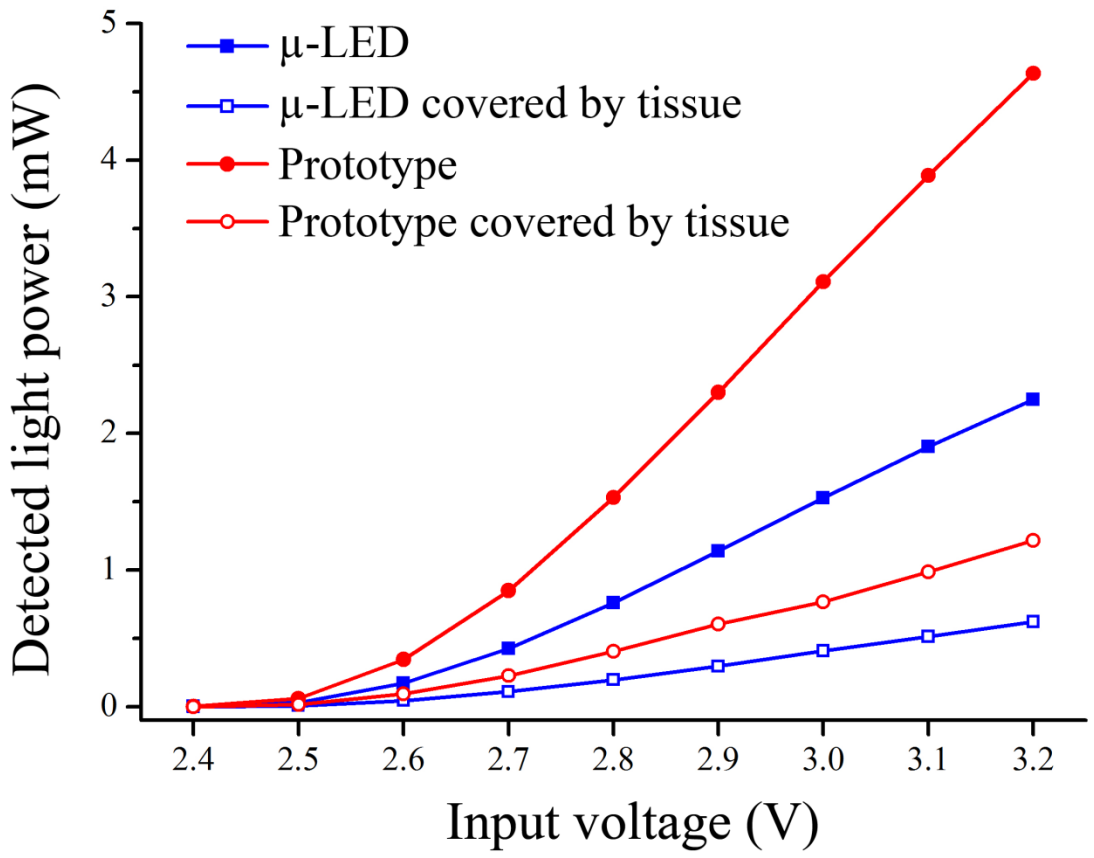

Figure 52 Detected light power of a device prototype of the optimized micro-lens-coupled LED stimulator (red) and the corresponding bare μ-LED (blue) under different driving voltages, which was measured with (hollow) and without (solid) a ~500-μm-thick rat cortical tissue slice. The photodetector has a sensing area of ~100 mm^2, which was positioned at a fixed effective penetration depth of 5,000 μm.

5.5 Summary

In this chapter, optimization of the structure of micro-lens-coupled neural stimulators was carried out in order to attain optimal collimation and penetration capabilities of light. The simulation was performed on the microlens and the reflector individually. The result shows that

the optimized micro-lens-coupled LED stimulator is able to activate excitatory opsins with 26.0% increase in penetration depth and 70.4% increase in the volume of stimulated tissue. The optimized microlenses and reflectors were fabricated through vapor-induced dewetting followed by integration with surface-mounted μ-LED chips to obtain device prototypes. The light power was measured by a photodetector and the fabricated device prototype shows an improvement of 15% to 102% as the effective penetration depth increased from 0 to 5,000 μm, compared to the bare μ-LED. While applying a 500-μm-thick rat cortical tissue slice, an average 99% light power enhancement at d_{eff} = 5,000 μm was achieved by the micro-lens-coupled LED stimulator under various voltages.

CHAPTER 6 Summary

A micro-lens-coupled LED stimulator has been proposed and successfully achieved in order to improve the LED light out-coupling efficiency for optogenetic applications. First, plasma treatment has been studied to adjust the surface wettability and the combined O_2 and SF_6 plasma has been found to be effective in altering the surface wettability of polymers. Especially, both super hydrophilicity and super hydrophobic have been obtained. This method was combined into a novel microfabrication technology, vapor-induced dewetting (VID), which can form self-organized spherical polymeric microlenses due to patterned surface chemistry heterogeneity. Microlenses with different dimensions and curvatures were produced under different conditions. Such microlenses were also employed to fabricate reflectors by PDMS micromolding. The microlenses and reflectors were used to integrate with micro-light-emitting diodes (μ-LEDs), forming micro-lens-coupled LED stimulators. A constantly ~78% improvement was obtained in gelatin under various voltages of 2.4-3.4 V for the fabricated prototypes. In addition, the structure of micro-lens-coupled LED stimulators was optimized by optical simulation, in order to achieve an optimal light collimation effect. Based on the optimization results, the 2nd generation of prototypes was integrated and characterized. As the effective penetration depth increased from 0 to 5,000 μm, the fabricated optimized device prototype shows an improvement of 15% to 102% compared to the bare μ-LED. They are expected to be employed as the light source in deep layer neural stimulation, providing stronger illumination and deeper penetration depth compared to bare μ-LEDs.

The main contributions of this thesis research are:

Contribution 1: Super hydrophobicity and super hydrophilicity have been achieved on Parylene-C films through fast and low-powered O_2 and SF_6 plasma treatments

Contribution 2: Developed a fast, self-organized, vapor-induced dewetting method to fabricate polymer-based microlens arrays on chemically pre-patterned substrates.

Contribution 3: Proposed and integrated a micro-lens-coupled LED stimulator, which can provide stronger illumination and deeper penetration depth.

Contribution 4: Optimized the structure of the micro-lens-coupled LED stimulator.

APPENDIX

Appendix Experimental Procedure

A. Water Contact Angle Measurement

1. Fill the syringe with DI water and assemble the syringe on the measurement setup.

2. Place the wafer on the stage and adjust the target position under the syringe.

3. Turn on the light source.

4. Open the software. Adjust the light intensity to make sure the brightness on the capture screen is neither too strong nor too weak.

5. Adjust the height of the stage to make both the tip of the middle and the wafer shown in the capture screen.

6. Turn the knob on the backside of the syringe, in order to push a certain amount of DI water out from the needle. 1 μL is always used for contact angle measurement. Fine focus is recommended on the water droplet.

7. Raise the stage slowly until the wafer makes contact with the water droplet. Then lower the stage gently. In most cases, the water will leave the needle tip and stay on the wafer surface. If the surface is super hydrophobic and the droplet does not drop, try to raise the stage a little bit more or shake the needle gently.

8. Capture an image in the software.

9. Open “contact angle analysis” software. Draw at least three points along the interface between water and air. The contact angle can be calculated by software.

10. When the measurement is finished, remove the wafer and turn off the light source.

B. Vapor-induced Dewetting

1. 2-μm-thick Parylene-C deposition on 2'' fresh silicon wafers.

2. Mix PDMS with a ratio of 10:1 before degassing in the oven.

3. Spin degassed PDMS on Parylene-covered silicon wafers. The speed is 5,000 rpm and the duration for the spin is 40 s. Approximate 10 μm thickness of PDMS can be achieved.

4. Baking at 110 °C for 10 min.

5. SF_6 plasma treatment for 40 s with an RF power of 100 W.

6. Spin-coat S1813 at 2,000 rpm for 40 s.

7. Baking at 110 °C for 10 min on the hot plate.

8. Lithography and development.

9. O_2 plasma treatment for 40 s with an RF power of 100 W.

10. Remove the photoresist by acetone.

11. Spin-coat SU-8 immediately on the plasma-treated wafers. Different SU-8 concentration can be prepared by diluting the resin in the SU-8 thinner using different ratios. The spin speed is 1,000 rpm the duration is 40 s. 10~30 μm thickness of SU-8 can be obtained when the wt% of SU-8 resin ranges 40%~60%.

12. Place the wafer into a beaker filled with SU-8 thinner. The wafer is elevated by a small support to avoid contact with the solvent liquid. Cover the beaker with a glass slide.

13. The progression of dewetting can be monitored through a stereo microscope equipped with a CCD camera, which can be used to take an image or record the progress.

C. LED Soldering

1. Place aluminum foil over a hot plate. Set the temperature of the hot plate to 120 °C.

2. Place 2-3 drops of hydrochloric acid in a glass dish filled with deionized water before placing low-temperature solder in the acid.

3. Place the glass dish on the hot plate. Wait until the solder is melted in the acid.

4. Carefully place the devices into the acid.

5. Pipet small droplets of solder onto the patterned spots on the devices, making sure that the solder is sticking to the patterned spots.

6. Use tweezers to retrieve the devices from the acid.

7. Rinse the devices in deionized water. Then check for the solder on the patterned spots under a microscope. If they have not appeared, repeat steps above.

8. Turn off the hot plate.

9. Take the micro-LEDs out of their container and transfer as many as needed to a sheet of PDMS using tweezers under a microscope.

10. Transfer the LEDs onto a device and align them on their target position. It is optional to apply some solder flux.

11. Turn on the hot plate and set the temperature to 80 °C.

12. Use a pin or tweezers to press down on the LEDs so that it can adhere to the solder. This step is done under a microscope.

13. Immerse the wafer in ethanol, acetone and DI water consecutively to remove the solder flux and photoresist.

14. Gently dry the wafer by adsorbing the water residue with wipes.

15. Use a multimeter to test the connection. The LEDs should light up.

16. Attach the wires onto the pads. Use epoxy the cover the connection for protection. After that, Parylene-C deposition is strongly recommended for better protection against water and moisture.

REFERENCES

REFERENCES

[1] A. Stroh and I. Diester, "Optogenetics: a new method for the causal analysis of neuronal networks in vivo," *Neuroforum,* vol. 18, no. 4, pp. 280-289, Nov 2012.

[2] E. S. Boyden, F. Zhang, E. Bamberg, G. Nagel, and K. Deisseroth, "Millisecond-timescale, genetically targeted optical control of neural activity," *Nature Neuroscience,* vol. 8, no. 9, pp. 1263-1268, Sep 2005.

[3] V. Gradinaru, F. Zhang, C. Ramakrishnan, J. Mattis, R. Prakash, I. Diester*, et al.*, "Molecular and cellular approaches for diversifying and extending optogenetics," *Cell,* vol. 141, no. 1, pp. 154-165, Apr 2010.

[4] M. Banghart, K. Borges, E. Isacoff, D. Trauner, and R. H. Kramer, "Light-activated ion channels for remote control of neuronal firing," *Nature Neuroscience,* vol. 7, no. 12, pp. 1381-1386, Dec 2004.

[5] K. Deisseroth, "Optogenetics," *Nature Methods,* vol. 8, no. 1, pp. 26-29, Jan 2011.

[6] P. Anikeeva, A. S. Andalman, I. Witten, M. Warden, I. Goshen, L. Grosenick*, et al.*, "Optetrode: a multichannel readout for optogenetic control in freely moving mice," *Nature Neuroscience,* vol. 15, no. 1, pp. 163-170, Jan 2012.

[7] J. J. Mancuso, J. Kim, S. Lee, S. Tsuda, N. B. H. Chow, and G. J. Augustine, "Optogenetic probing of functional brain circuitry," *Experimental Physiology,* vol. 96, no. 1, pp. 26-33, Jan 2011.

[8] L. Buchen, "Neuroscience: Illuminating the brain," *Nature,* vol. 465, no. 7294, pp. 26-28, May 2010.

[9] F. Zhang, V. Gradinaru, A. R. Adamantidis, R. Durand, R. D. Airan, L. de Lecea*, et al.*, "Optogenetic interrogation of neural circuits: technology for probing mammalian brain structures," *Nature Protocols,* vol. 5, no. 3, pp. 439-456, Feb 2010.

[10] H. E. Covington, M. K. Lobo, I. Maze, V. Vialou, J. M. Hyman, S. Zaman*, et al.*, "Antidepressant Effect of Optogenetic Stimulation of the Medial Prefrontal Cortex," *Journal of Neuroscience,* vol. 30, no. 48, pp. 16082-16090, Dec 2010.

[11] A. V. Kravitz, B. S. Freeze, P. R. L. Parker, K. Kay, M. T. Thwin, K. Deisseroth*, et al.*, "Regulation of parkinsonian motor behaviours by optogenetic control of basal ganglia circuitry," *Nature,* vol. 466, no. 7306, pp. 622-626, Jul 2010.

[12] N. McAlinden, D. Massoubre, E. Richardson, E. Gu, S. Sakata, M. D. Dawson*, et al.*, "Thermal and optical characterization of micro-LED probes for in vivo optogenetic neural stimulation," *Optics Letters,* vol. 38, no. 6, pp. 992-994, Mar 2013.

[13] C. T. Wentz, J. G. Bernstein, P. Monahan, A. Guerra, A. Rodriguez, and E. S. Boyden, "A

wirelessly powered and controlled device for optical neural control of freely-behaving animals," *Journal of Neural Engineering,* vol. 8, no. 4, pp. 046021-1–046021-10, Aug 2011.

[14] N. Grossman, V. Poher, M. S. Grubb, G. T. Kennedy, K. Nikolic, B. McGovern*, et al.*, "Multi-site optical excitation using ChR2 and micro-LED array," *Journal of Neural Engineering,* vol. 7, no. 1, pp. 016004-1–016004-13, Feb 2010.

[15] B. McGovern, R. B. Palmini, N. Grossman, E. M. Drakakis, V. Poher, M. A. A. Neil*, et al.*, "A new individually addressable micro-LED array for photogenetic neural stimulation," *IEEE Transactions on Biomedical Circuits and Systems,* vol. 4, no. 6, pp. 469-476, Dec 2010.

[16] P. Degenaar, B. McGovern, R. Berlinguer-Palmini, N. Vysokov, N. Grossman, V. Pohrer*, et al.*, "Individually addressable optoelectronic arrays for optogenetic neural stimulation," in *Proc. Int. Conf. BioCAS*, Nov 2010, pp. 170-173.

[17] K. Y. Kwon, A. Khomenko, M. Haq, and W. Li, "Integrated slanted microneedle-LED array for optogenetics," in *Proc. 35th Int. Conf. EMBC*, Jul 2013, pp. 249-252.

[18] A. M. Aravanis, L. P. Wang, F. Zhang, L. A. Meltzer, M. Z. Mogri, M. B. Schneider*, et al.*, "An optical neural interface: in vivo control of rodent motor cortex with integrated fiberoptic and optogenetic technology," *Journal of Neural Engineering,* vol. 4, no. 3, pp. S143-S156, Sep 2007.

[19] K. Y. Kwon, X. P. Bi, and W. Li, "Droplet backside exposure for making slanted SU-8 microneedles," in *Proc. 35th Int. Conf. EMBC*, Jul 2013, pp. 767-770.

[20] S. Moller and S. R. Forrest, "Improved light out-coupling in organic light emitting diodes employing ordered microlens arrays," *Journal of Applied Physics,* vol. 91, no. 5, pp. 3324-3327, Mar 2002.

[21] Y. Sun and S. R. Forrest, "Enhanced light out-coupling of organic light-emitting devices using embedded low-index grids," *Nature Photonics,* vol. 2, no. 8, pp. 483-487, Aug 2008.

[22] E. Burkarter, C. K. Saul, F. Thomazi, N. C. Cruz, L. S. Roman, and W. H. Schreiner, "Superhydrophobic electrosprayed PTFE," *Surface and Coatings Technology,* vol. 202, no. 1, pp. 194-198, Nov 2007.

[23] R. N. Wenzel, "Resistance of solid surfaces to wetting by water," *Industrial and Engineering Chemistry,* vol. 28, no. 8, pp. 988-994, Aug 1936.

[24] A. B. D. Cassie and S. Baxter, "Wettability of porous surfaces," *Transactions of the Faraday Society,* vol. 40, pp. 546-550, Sep 1944.

[25] S. J. Zhu, Y. F. Li, J. H. Zhang, C. L. Lu, X. Dai, F. Jia*, et al.*, "Biomimetic polyimide nanotube arrays with slippery or sticky superhydrophobicity," *Journal of Colloid and Interface Science,* vol. 344, no. 2, pp. 541-546, Apr 2010.

[26] K. K. S. Lau, J. Bico, K. B. K. Teo, M. Chhowalla, G. A. J. Amaratunga, W. I. Milne*, et*

al., "Superhydrophobic carbon nanotube forests," *Nano Letters,* vol. 3, no. 12, pp. 1701-1705, Dec 2003.

[27] J. Yeo, M. J. Choi, and D. S. Kim, "Robust hydrophobic surfaces with various micropillar arrays," *Journal of Micromechanics and Microengineering,* vol. 20, no. 2, pp. 025028-1–025028-8, Feb 2010.

[28] H. E. Jeong, S. H. Lee, J. K. Kim, and K. Y. Suh, "Nanoengineered multiscale hierarchical structures with tailored wetting properties," *Langmuir,* vol. 22, no. 4, pp. 1640-1645, Feb 2006.

[29] Y. Yoon, D. W. Lee, and J. B. Lee, "Surface modified nano-patterned SU-8 pillar array optically transparent super-hydrophobic thin film," *Journal of Micromechanics and Microengineering,* vol. 22, no. 3, pp. 035012-1–035012-7, Mar 2012.

[30] B. Lu, J. C. H. Lin, Z. Liu, Y. K. Lee, and Y. C. Tai, "Highly flexible, transparent and patternable parylene-C superhydrophobic films with high and low adhesion," in *Proc. 24th Int. Conf. MEMS*, Jan 2011, pp. 1143-1146.

[31] K. Tsougeni, N. Vourdas, A. Tserepi, E. Gogolides, and C. Cardinaud, "Mechanisms of oxygen plasma nanotexturing of organic polymer surfaces: from stable super hydrophilic to super hydrophobic surfaces," *Langmuir,* vol. 25, no. 19, pp. 11748-11759, Oct 2009.

[32] I. Woodward, W. C. E. Schofield, V. Roucoules, and J. P. S. Badyal, "Super-hydrophobic surfaces produced by plasma fluorination of polybutadiene films," *Langmuir,* vol. 19, no. 8, pp. 3432-3438, Apr 2003.

[33] E. C. Rangel, W. C. A. Bento, M. E. Kayama, W. H. Schreiner, and N. C. Cruz, "Enhancement of polymer hydrophobicity by SF_6 plasma treatment and argon plasma immersion ion implantation," *Surface and Interface Analysis,* vol. 35, no. 2, pp. 179-183, Feb 2003.

[34] M. Ataeefard, S. Moradian, M. Mirabedini, M. Ebrahimi, and S. Asiaban, "Investigating the effect of power/time in the wettability of Ar and O_2 gas plasma-treated low-density polyethylene," *Progress in Organic Coatings,* vol. 64, no. 4, pp. 482-488, Mar 2009.

[35] W. Li, D. C. Rodger, E. Meng, J. D. Weiland, M. S. Humayun, and Y. C. Tai, "Flexible parylene packaged intraocular coil for retinal prostheses," in *Proc. Int. Conf. MMB*, May 2006, pp. 105-108.

[36] D. C. Rodger, J. D. Weiland, M. S. Humayun, and Y. C. Tai, "Scalable high lead-count parylene package for retinal prostheses," *Sensors and Actuators B-Chemical,* vol. 117, no. 1, pp. 107-114, Sep 2006.

[37] P. Y. Li, J. Shih, R. Lo, S. Saati, R. Agrawal, M. S. Humayun*, et al.*, "An electrochemical intraocular drug delivery device," *Sensors and Actuators A-Physical,* vol. 143, no. 1, pp. 41-48, May 2008.

[38] J. M. Hsu, L. Rieth, R. A. Normann, P. Tathireddy, and F. Solzbacher, "Encapsulation of

an integrated neural interface device with Parylene C," *IEEE Transactions on Biomedical Engineering,* vol. 56, no. 1, pp. 23-29, Jan 2009.

[39] S. Takeuchi, D. Ziegler, Y. Yoshida, K. Mabuchi, and T. Suzuki, "Parylene flexible neural probes integrated with microfluidic channels," *Lab on a Chip,* vol. 5, no. 5, pp. 519-523, May 2005.

[40] X. Liu, L. Li, B. Awate, R. M. Worden, G. Reguera, and A. J. Mason, "Biosensor array microsystem on a CMOS amperometric readout chip," in *Proc. Int. Conf. BioCAS*, Nov 2011, pp. 305-308.

[41] J. S. Song, S. Lee, S. H. Jung, G. C. Cha, and M. S. Mun, "Improved biocompatibility of Parylene-C films prepared by chemical vapor deposition and the subsequent plasma treatment," *Journal of Applied Polymer Science,* vol. 112, no. 6, pp. 3677-3685, Jun 2009.

[42] T. Trantidou, T. Prodromakis, and C. Toumazou, "Oxygen plasma induced hydrophilicity of Parylene-C thin films," *Applied Surface Science,* vol. 261, pp. 43-51, Nov 2012.

[43] J. N. Chai, F. Z. Lu, B. M. Li, and D. Y. Kwok, "Wettability interpretation of oxygen plasma modified poly(methyl methacrylate)," *Langmuir,* vol. 20, no. 25, pp. 10919-10927, Dec 2004.

[44] K. S. Kim, K. H. Lee, K. Cho, and C. E. Park, "Surface modification of polysulfone ultrafiltration membrane by oxygen plasma treatment," *Journal of Membrane Science,* vol. 199, no. 1-2, pp. 135-145, Apr 2002.

[45] K. Tsougeni, P. S. Petrou, A. Tserepi, S. E. Kakabakos, and E. Gogolides, "Nano-texturing of poly(methyl methacrylate) polymer using plasma processes and applications in wetting control and protein adsorption," *Microelectronic Engineering,* vol. 86, no. 4-6, pp. 1424-1427, Apr-Jun 2009.

[46] F. Walther, P. Davydovskaya, S. Zucher, M. Kaiser, H. Herberg, A. M. Gigler*, et al.*, "Stability of the hydrophilic behavior of oxygen plasma activated SU-8," *Journal of Micromechanics and Microengineering,* vol. 17, no. 3, pp. 524-531, Mar 2007.

[47] J. F. Chang and H. Sirringhaus, "Patterning of solution-processed semiconducting polymers in high-mobility thin-film transistors by physical delamination," *Advanced Materials,* vol. 21, no. 24, pp. 2530-2535, Jun 2009.

[48] K. Tsougeni, D. Papageorgiou, A. Tserepi, and E. Gogolides, ""Smart" polymeric microfluidics fabricated by plasma processing: controlled wetting, capillary filling and hydrophobic valving," *Lab on a Chip,* vol. 10, no. 4, pp. 462-469, 2010.

[49] P. Rezai, P. R. Selvaganapathy, and G. Rwohl, "Plasma enhanced bonding of polydimethylsiloxane with parylene and its optimization," *Journal of Micromechanics and Microengineering,* vol. 21, no. 6, pp. 065024-1–065024-13, Jun 2011.

[50] E. Chibowski, "Surface free energy of a solid from contact angle hysteresis," *Advances in*

Colloid and Interface Science, vol. 103, no. 2, pp. 149-172, Apr 2003.

[51] Z. D. Popovic, R. A. Sprague, and G. A. N. Connell, "Technique for monolithic fabrication of microlens arrays," *Applied Optics,* vol. 27, no. 7, pp. 1281-1284, Apr. 1988.

[52] R. Mukherjee, D. Bandyopadhyay, and A. Sharma, "Control of morphology in pattern directed dewetting of thin polymer films," *Soft Matter,* vol. 4, no. 10, pp. 2086-2097, 2008.

[53] J. Lim, M. Jung, C. Joo, and S. Kang, "Development of micro-objective lens array for large field-of-view multi-optical probe confocal microscopy," *Journal of Micromechanics and Microengineering,* vol. 23, no. 6, pp. 065028-1–065028-7, Jun. 2013.

[54] H. H. Yang, C. K. Chao, M. K. Wei, and C. P. Lin, "High fill-factor microlens array mold insert fabrication using a thermal reflow process," *Journal of Micromechanics and Microengineering,* vol. 14, no. 8, pp. 1197-1204, Aug. 2004.

[55] E. Roy, B. Voisin, J. F. Gravel, R. Peytavi, D. Boudreau, and T. Veres, "Microlens array fabrication by enhanced thermal reflow process: Towards efficient collection of fluorescence light from microarrays," *Microelectronic Engineering,* vol. 86, no. 11, pp. 2255-2261, Nov 2009.

[56] H. Yang, C. K. Chao, C. P. Lin, and S. C. Shen, "Micro-ball lens array modeling and fabrication using thermal reflow in two polymer layers," *Journal of Micromechanics and Microengineering,* vol. 14, no. 2, pp. 277-282, Feb. 2004.

[57] K. Totsu, K. Fujishiro, S. Tanaka, and M. Esashi, "Fabrication of three-dimensional microstructure using maskless gray-scale lithography," *Sensors and Actuators A-Physical,* vol. 130-131, pp. 387-392, Aug 2006.

[58] M. Manevich, M. Klebanov, V. Lyubin, J. Varshal, J. Broder, and N. P. Eisenberg, "Gap micro-lithography for chalcogenide micro-lens array fabrication," *Chalcogenide Letters,* vol. 5, no. 4, pp. 61-64, Apr 2008.

[59] J. Y. Kim, N. B. Brauer, V. Fakhfouri, D. L. Boiko, E. Charbon, G. Grutzner*, et al.*, "Hybrid polymer microlens arrays with high numerical apertures fabricated using simple ink-jet printing technique," *Optical Materials Express,* vol. 1, no. 2, pp. 259-269, Jun 2011.

[60] J. Y. Kim, K. Pfeiffer, A. Voigt, G. Gruetzner, and J. Brugger, "Directly fabricated multi-scale microlens arrays on a hydrophobic flat surface by a simple ink-jet printing technique," *Journal of Materials Chemistry,* vol. 22, no. 7, pp. 3053-3058, 2012.

[61] V. Fakhfouri, N. Cantale, G. Mermoud, J. Y. Kim, D. Boiko, E. Charbon*, et al.*, "Inkjet printing of SU-8 for polymer-based MEMS a case study for microlenses," in *Proc. 21st Int. Conf. MEMS*, Jan 2008, pp. 407-410.

[62] R. van Hameren, P. Schon, A. M. van Buul, J. Hoogboom, S. V. Lazarenko, J. W. Gerritsen*, et al.*, "Macroscopic hierarchical surface patterning of porphyrin trimers via self-assembly and dewetting," *Science,* vol. 314, no. 5804, pp. 1433-1436, Dec 2006.

[63] A. M. Higgins and R. A. L. Jones, "Anisotropic spinodal dewetting as a route to self-assembly of patterned surfaces," *Nature,* vol. 404, no. 6777, pp. 476-478, Mar 2000.

[64] L. J. Xue and Y. C. Han, "Pattern formation by dewetting of polymer thin film," *Progress in Polymer Science,* vol. 36, no. 2, pp. 269-293, Feb 2011.

[65] D. Bonn, J. Eggers, J. Indekeu, J. Meunier, and E. Rolley, "Wetting and spreading," *Reviews of Modern Physics,* vol. 81, no. 2, pp. 739-805, Apr-Jun 2009.

[66] R. Seemann, S. Herminghaus, and K. Jacobs, "Gaining control of pattern formation of dewetting liquid films," *Journal of Physics-Condensed Matter,* vol. 13, no. 21, pp. 4925-4938, May 2001.

[67] G. Reiter, "Dewetting of thin polymer-films," *Physical Review Letters,* vol. 68, no. 1, pp. 75-78, Jan 1992.

[68] R. B. Xing, C. X. Luo, Z. Wang, and Y. C. Han, "Dewetting of polymethyl methacrylate on the patterned elastomer substrate by solvent vapor treatment," *Polymer,* vol. 48, no. 12, pp. 3574-3583, Jun 2007.

[69] B. Yoon, H. Acharya, G. Lee, H. C. Kim, J. Huh, and C. Park, "Nanopatterning of thin polymer films by controlled dewetting on a topographic pre-pattern," *Soft Matter,* vol. 4, no. 7, pp. 1467-1472, 2008.

[70] A. Verma and A. Sharma, "Enhanced self-organized dewetting of ultrathin polymer films under water-organic solutions: Fabrication of sub-micrometer spherical lens arrays," *Advanced Materials,* vol. 22, no. 46, pp. 5306-5309, Dec 2010.

[71] A. Sehgal, V. Ferreiro, J. F. Douglas, E. J. Amis, and A. Karim, "Pattern-directed dewetting of ultrathin polymer films," *Langmuir,* vol. 18, no. 18, pp. 7041-7048, Sep 2002.

[72] D. Julthongpiput, W. H. Zhang, J. F. Douglas, A. Karim, and M. J. Fasolka, "Pattern-directed to isotropic dewetting transition in polymer films on micropatterned surfaces with differential surface energy contrast," *Soft Matter,* vol. 3, no. 5, pp. 613-618, 2007.

[73] B. J. Brasjen, H. Gu, and A. A. Darhuber, "Dewetting of thin liquid films on chemically patterned substrates: front propagation along narrow lyophobic stripes and stripe arrays," *Microfluidics and Nanofluidics,* vol. 14, no. 3-4, pp. 669-682, Mar 2013.

[74] Z. X. Zhang, Z. Wang, R. B. Xing, and Y. C. Han, "Patterning thin polymer films by surface-directed dewetting and pattern transfer," *Polymer,* vol. 44, no. 13, pp. 3737-3743, Jun 2003.

[75] L. W. Schwartz and R. R. Eley, "Simulation of droplet motion on low-energy and heterogeneous surfaces," *Journal of Colloid and Interface Science,* vol. 202, no. 1, pp. 173-188, Jun 1998.

[76] A. Oron, S. H. Davis, and S. G. Bankoff, "Long-scale evolution of thin liquid films,"

Reviews of Modern Physics, vol. 69, no. 3, pp. 931-980, Jul 1997.

[77] T. P. Witelski and M. Bowen, "ADI schemes for higher-order nonlinear diffusion equations," *Applied Numerical Mathematics,* vol. 45, no. 2-3, pp. 331-351, May 2003.

[78] B. J. Brasjen and A. A. Darhuber, "Dry-spot nucleation in thin liquid films on chemically patterned surfaces," *Microfluidics and Nanofluidics,* vol. 11, no. 6, pp. 703-716, Dec 2011.

[79] R. Konnur, K. Kargupta, and A. Sharma, "Instability and morphology of thin liquid films on chemically heterogeneous substrates," *Physical Review Letters,* vol. 84, no. 5, pp. 931-934, Jan 2000.

[80] C. V. Thompson, "Solid-State Dewetting of Thin Films," *Annual Review of Materials Research,* vol. 42, pp. 399-434, 2012.

[81] L. W. Schwartz, R. V. Roy, R. R. Eley, and S. Petrash, "Dewetting patterns in a drying liquid film," *Journal of Colloid and Interface Science,* vol. 234, no. 2, pp. 363-374, Feb 2001.

[82] L. Leibler and K. Sekimoto, "On the sorption of gases and liquids in glassy-polymers," *Macromolecules,* vol. 26, no. 25, pp. 6937-6939, Dec 1993.

[83] L. Xu, A. Sharma, and S. W. Joo, "Dewetting of stable thin polymer films induced by a poor solvent: Role of polar interactions," *Macromolecules,* vol. 45, no. 16, pp. 6628-6633, Aug 2012.

[84] G. Ghigliotti, C. F. Zhou, and J. J. Feng, "Simulations of the breakup of liquid filaments on a partially wetting solid substrate," *Physics of Fluids,* vol. 25, no. 7, pp. 072102-1–072102-14, Jul 2013.

[85] X. Han, X. F. Qian, J. G. Bernstein, H. H. Zhou, G. T. Franzesi, P. Stern*, et al.*, "Millisecond-Timescale Optical Control of Neural Dynamics in the Nonhuman Primate Brain," *Neuron,* vol. 62, no. 2, pp. 191-198, Apr 2009.

[86] K. Y. Kwon, H. M. Lee, M. Ghovanloo, A. Weber, W. Li, and Ieee, "A WIRELESS SLANTED OPTRODE ARRAY WITH INTEGRATED MICRO LEDS FOR OPTOGENETICS," *2014 Ieee 27th International Conference on Micro Electro Mechanical Systems (Mems),* pp. 813-816, 2014.

[87] E. Stark, T. Koos, and G. Buzsaki, "Diode probes for spatiotemporal optical control of multiple neurons in freely moving animals," *Journal Of Neurophysiology,* vol. 108, no. 1, pp. 349-363, Jul 2012.

[88] X. P. Bi and W. Li, "Fabrication of flexible microlens arrays through vapor-induced dewetting on selectively plasma-treated surfaces," *Journal Of Materials Chemistry C,* vol. 3, no. 22, pp. 5825-5834, 2015.

[89] K. Y. Kwon, B. Sirowatka, A. Weber, and W. Li, "Opto-μECoG Array: A Hybrid Neural Interface With Transparent μECoG Electrode Array and Integrated LEDs for

Optogenetics," *IEEE Transactions on Biomedical Circuits and Systems,* vol. 7, no. 5, pp. 593-600, 2013.

[90] B. Gysbrechts, L. Wang, N. N. D. Trong, H. Cabral, Z. Navratilova, F. Battaglia*, et al.*, "Light distribution and thermal effects in the rat brain under optogenetic stimulation," *Journal of Biophotonics,* vol. 9, no. 6, pp. 576-585, 2016.